Design and Implementation of Articulated Robotic Tails to Augment the Performance of Reduced Degree-of-Freedom Legged Robots

Wael Saab

Dissertation submitted to the faculty of the Virginia Polytechnic Institute and State University in partial fulfillment of the requirements for the degree of

Doctor of Philosophy
In
Mechanical Engineering

Pinhas Ben-Tzvi, Chair
Nabil Simaan
Steve C. Southward
Andrew J. Kurdila

March 19, 2018
Blacksburg, Virginia

Keywords: Robotics, Legged Robots, Robotic Tails, Mechanical Design, Dynamic Modeling, Control

ABSTRACT

Design and Implementation of Articulated Robotic Tails to Augment the Performance of Reduced Degree-of-Freedom Legged Robots

Wael Saab

This dissertation explores the design, and implementation of articulated robotic tail mechanisms onboard reduced degree-of-freedom (DOF) legged robots to augment performance in terms of stability and maneuverability. Fundamentally, this research is motivated by the question of how to improve the stability and maneuverability of legged robots. The conventional approach to address these challenges is to utilize leg mechanisms that are composed of three or more active DOFs that are controlled simultaneously to provide propulsion, maneuvering, and stabilization. However, animals such as lizards and cheetahs have been observed to utilize their tails to aid in these functionalities. It is hypothesized that by using an articulated tail mechanism to aid in these functionalities onboard a legged robot, the burden on the robot's legs to simultaneously maneuver and stabilize the robot may be reduced. This could allow for simplification of the leg's design and control algorithms.

In recent years, significant progress has been accomplished in the field of robotic tail implementation onboard mobile robots. However, the main limitation of this work stems from the proposed tail designs, the majority of which are composed of rigid single-body pendulums that provide a constrained workspace for center-of-mass positioning, an important characteristics for inertial adjustment applications.

Inspired by lizards and cheetahs that adjust their body orientation using flexible tail motions, two novel articulated, cable driven, serpentine-like tail mechanisms are proposed. The first is the Roll-Revolute-Revolute Tail which is a 3-DOF mechanism, designed for implementation onboard a quadruped robot, that is capable of forming two mechanically decoupled tail curvatures via an s-shaped cable routing scheme and gear train system. The second is a the Discrete Modular Serpentine Tail, designed for implementation onboard a biped robot, which is a modular two-DOF mechanism that distributes motion amongst links via a multi-diameter pulley. Both tail designs utilize a cable transmission system where cables are routed about

circular contoured links that maintain equal antagonistic cable displacements that can produce controlled articulated tail curvatures using a single active-DOF. Furthermore, analysis and experimental results have been presented to demonstrate the effectiveness of an articulated tail's ability to: 1) increase the manifold for center-of-mass positioning, and 2) generate enhanced inertial loading relative to conventionally implemented pendulum-like tails.

In order to test the tails ability to augment the performance of legged robots, a novel Robotic Modular Leg (RML) is proposed to construct both a reduced-DOF quadrupedal and bipedal experimental platform. The RML is a modular two-DOF leg mechanism composed of two serially connected four-bar mechanisms that utilizes kinematic constraints to maintain a parallel orientation between it's flat foot and body without the use of an actuated ankle. A passive suspension system integrated into the foot enables the dissipation of impact energy and maintains a stable four point-of-contact support polygon on both flat and uneven terrain.

Modeling of the combined legged robotic systems and attached articulated tails has led to the derivation of dynamic formulations that were analyzed to scale articulated tails onboard legged robots to maximize inertial adjustment capabilities resulting from tail motions and design a control scheme for tail-aided maneuvering.

The tail prototypes, in conjunction with virtual simulations of the quadruped and biped robot, were used in experiments and simulations to implement and analyze the methods for maneuvering and stabilizing the proposed legged robots. Results successfully demonstrate the tails' ability to augment the performance of reduced-DOF legged robots by enabling comparable walking criteria with respect to conventional legged robots. This research provides a firm foundation for future work involving design and implementation of articulated tails onboard legged robots for enhanced inertial adjustment applications.

GENERAL AUDIENCE ABSTRACT

Design and Implementation of Articulated Robotic Tails to Augment the Performance of Reduced Degree-of-Freedom Legged Robots

Wael Saab

In nature, animals commonly use their tails to assist propulsion, stabilization, and maneuvering. However, in legged robotic systems, the dominant research paradigm has been to focus on the design and control of the legs as a means to simultaneously provide propulsion, maneuvering, and stabilization. Fundamentally, this research is motivated by the question of how to improve the stability and maneuverability of legged robots utilizing an articulated tail mechanism. It is hypothesized that by using an articulated tail mechanism to aid in these functionalities onboard a legged robots, the burden on the robot's legs to simultaneously maneuver and stabilize the robot may be reduced. This could allow for simplification of the leg's design and control algorithms.

This doctoral dissertation addresses this problem statement and hypothesis by proposing two articulated tail mechanisms, R3-RT and DMST, that are uniquely designed to be practically implemented on a reduced DOF quadruped and biped robot, respectively, for tail-aided stabilization and maneuverability. Through analysis and experimentation, it is demonstrated that articulated tails enable enhanced workspace and inertial loading capabilities relative to previously implemented pendulum-like tails while the proposed leg mechanism enables the construction of legged robots with simplified design and control. However, these legged robots cannot effectively walk as standalone machines which justifies the implementation of articulated tails for augmented performance. The dynamics of the combined robotic system consisting of reduced DOF legged robots with implemented tails are derived to scale and optimize articulated tails to maximize inertial adjustment capabilities and derive control schemes for enhanced maneuvering and stabilization using tail-aided motion. Using experiments and simulations, the combined robotic systems consisting of a reduced DOF quadruped and biped robots augmented via articulated tails demonstrate walking criteria that is comparable to conventional legged robots.

ACKNOWLEDGMENTS

TABLE OF CONTENTS

LIST OF FIGURES

LIST OF TABLES

CHAPTER 1: INTRODUCTION

This dissertation explores the design, and implementation of articulated robotic tail mechanisms onboard legged robots to augment performance in terms of stabilization and maneuverability. This work addresses two challenges that arise from the limitations of current implementation of robotic tails intended for inertial adjustment applications onboard legged robots. The first is designing articulated tail mechanisms for practical implementation onboard legged robots and analyzing their inertial adjustment capabilities through a series of simulation and experimental case studies to demonstrate enhanced capabilities relative to conventional pendulum-like tails. To justify the addition of a tail onboard legged robot, the tail must provide multiple functionalities for the legged robot to reduce the burden on the legs in producing simultaneous propulsion, maneuvering, and stabilization. The second challenge is to investigate: 1) the performance enhancement capabilities an articulated tail can provide a legged robot in terms of stabilization and maneuvering and, 2) the potential reduction in design and control complexity of the legged robot that tail implementation can enable when aiding maneuvering and stabilization applications. The objective of this dissertation is to jointly synthesize a robotic system composed of a reduced-DOF legged robot with an attached articulated tail mechanism. Then, analyze and demonstrate the tails performance enhancement capabilities in terms of stabilization and maneuverability onboard the proposed reduced-DOF legged robots.

1.1 Motivation and Scope of Work

By observing nature, engineers can gain a source of inspiration to address major challenges within the field of robotics. For example, animals use their tails for a wide variety of tasks ranging from stabilization, maneuvering, propulsion, and manipulation [1]. By studying fossil remains, scientists believe that the Tyrannosaurus Rex swung its tail laterally to counter-act the weight of its massive body while it walked forward [2, 3]. Similarly, kangaroos have been observed to use their tails in a compliant mode as a counter balance while hopping [4], and can stiffen their tails to provide an additional limb while standing on their hind legs or engaging in defensive boxing routines [5]. Kangaroo rats and lizards have been observed to swing their tails while in mid-air to

reorient their bodies [6, 7]. Green Iguanas are known to lash their tails against predators to escape dangerous situations [8]. Other examples of tail usage include monkeys climbing and grasping objects, an alligator rolling underwater, or the propulsion of fish through water. These stabilization, maneuvering, and propulsive behaviors are examples of inertial adjustment, where a structure onboard a system is used to generate inertial forces and moments to modify the dynamics of the animal. While tails are the most obvious inertial adjustment mechanism used by animals, any motion of an appendage or body mass can be used for angular reorientation such as wings [9], spines [10], or legs [11, 12]. By observing these functionalities scaled over a wide range of sizes and uses, engineers have been inspired to apply inertial adjustment mechanisms to mobile robotics to further enhance stabilization and maneuverability.

Researchers have proposed robotic tail utilization for inertial adjustment applications onboard mobile robots. However, the existing literature has been dominated by rigid, single-DOF pendulums that provide improved performance limited to specific planes. Recently, spatial pendulum-like tails have been proposed that provide multi-axis performance enhancement capabilities and an increased workspace. Research thrusts, as part of this work, have shifted away from the conventional design structures of single-body pendulum like tails to investigate the performance advantages articulated, spatial tails can provide; such as, forming multiple configuration shapes that enable enhanced inertial loading capabilities and a greater workspace for end effector and center-of-mass (COM) positioning.

In the field of legged robotics, the dominant research paradigm has focused on leg mechanism designs that are composed of three or more active DOFs, and developing leg control algorithms to simultaneously propel, maneuver, and stabilize the robot. Although conventional legged robots are composed of a large number active DOFs, that do enhance locomotion and tasking abilities, each additional DOF increases the robot's weight, energy consumption and complexity of foot trajectory planning and control. It is hypothesized that by using an articulated tail mechanism to aid in tasks involving stabilization and maneuvering onboard a legged robots, the burden on the robot's legs to simultaneously maneuver, and stabilize the robot may be reduced. This could allow for simplification of the leg's design and control algorithms. As part of this work, a reduced-DOF modular robotic leg mechanism is presented to construct both a quadrupedal and bipedal experimental platform that are utilized to investigate the articulated tails capabilities in augmenting performance to exhibit similar walking criteria relative to conventional legged robots.

2

1.2 Objectives

The aforementioned challenges motivated this research with the aim to enhance the performance of legged robots via an attached articulated inertial tail. In particular, this dissertation seeks to design, analyze, and synthesize articulated tail mechanisms that exhibit inertial adjustment capabilities (relative to previous pendulum-like tail designs), intended to be attached onboard quadruped and biped robots composed of reduced DOF leg mechanisms to provide a means, separate from the legs, to aid functionalities such as of stabilization, and maneuverability. This aim entails the accomplishment of the following objectives:

- Robotic Tail Design: Investigate the mechanical design of various robotic manipulators to identify idealized design criteria to be incorporated into the proposed articulated tail mechanisms.

- Reduced DOF Robotic Leg Design: Investigate existing leg mechanism designs, and develop a reduced DOF modular leg with less than three active DOFs to construct both a quadrupedal, and bipedal experimental platform to test the performance enhancement criteria that the proposed articulated tail mechanisms can provide in terms of stabilization, and maneuverability.

- Dynamic Modeling and Control: Develop dynamic models of articulated tails onboard legged robots to: 1) optimize design parameters of articulated tail mechanisms onboard legged robots to maximize inertial adjustment capabilities, and 2) develop control schemes that exhibit goal oriented behavior to effectively augment the performance of reduced-DOF legged robots in terms of maneuvering, and stabilization applications.

The objective of this work is to design and implement an articulated robotic tail onboard a reduced-DOF legged robot to augment the legged robot's performance in terms of stabilization and maneuvering using tail-aided motion. Performance of the proposed robotic systems consisting of an articulated tail onboard a reduced-DOF legged robot will be evaluated through experimental and simulation based case studies to demonstrate comparable walking criteria relative to conventional legged robots, listed as: (1) maintain quasi-static stability during locomotion, (2)

maintain a constant robot body height during a waiting gait, (3) maintain horizontal body orientation during a walking gait, (4) have the ability to move backward, forward and (5) steer.

1.3 Contributions

The contributions of this dissertation span a range of research topics that include: mechanical design, analysis, and experimental validation of hyper-redundant, cable driven manipulators, and reduced DOF legged robots. In addition to dynamic modeling, optimization, and control of articulated tails onboard legged robots for enhanced stabilization, and maneuvering applications. These contributions are summarized as follows:

- Robotic Tail Design and Implementation Review: A state-of-the-art review is presented in the field of mobile robotics that utilize pendulum-like, and continuum robotic tails for inertial adjustment applications along with a tabular comparison highlighting the attributes of existing robotic systems to identify quantitative performance criteria to aid the design, and implementation of novel articulated tail designs [13].

- Articulated Robotic Tail Design: Two novel articulated robotic tails differing in topology, degrees of actuation are conceptualized, designed, analyzed, and integrated into prototypes.

    1) A novel 3 DOF serpentine tail structure (2 articulated tail curvatures, and 1 roll motion) mechanism, called the Roll-Revolute-Revolute Tail (R3-RT) [14] intended for use onboard a quadruped robot, is composed of rigid links interconnected via revolute joints. Cable routing about circular contoured links, and an S-shape cable routing scheme maintains equal antagonistic cable displacements. Therefore, the antagonistic cables can be connected single active DOF to control an articulated tail segment. Furthermore, this enables mechanical decoupling of articulated segments connected in series using a gear train system to regulate equal relative link rotation and kinematically resolve the redundancy within articulated tail segments. A slip ring incorporated into the roll DOF enables infinite rotation without the risk of breaking wires and enables the tail to act like a reaction wheel by imparting long duration, unconstrained reactive moments about the roll-axis. Significant experimental results in this dissertation have

4

corroborated previous analytical simulations results presented by Rone and Ben-Tzvi [15] by demonstrating that articulated tails can provide enhanced inertial loading capabilities (53 % net increase in generated moments, and 46 % net decrease in generated forces) in comparison to pendulum-like tails. These experimental results demonstrate that articulated tails exhibit enhanced loading capabilities relative to previously implemented pendulum-like tails.

2) A novel 2-DOF serpentine tail structure (1 articulated tail curvature, and 1 roll motion), called the Discrete Modular Serpentine Tail (DMST) [16, 17] intended for use onboard a biped robot, utilizes a cable transmission system routed about circular contoured rigid links to enable equal antagonistic cable displacements. Therefore, the antagonistic cables can be connected to a multi-diameter pulley that, upon rotation, creates a controlled articulated tail curvature using a single active DOF. Each module is self-contained, a feature that enables infinite rotation about the roll-axis for reaction wheel-like operation and the modular connection of multiple tail modules in series to achieve independently actuated multi-tail curvatures.

- Reduced DOF Robotic Leg Design: A novel modular two-DOF leg mechanism, called the Robotic Modular Leg [18, 19], is used to construct reduced-DOF legged robotic platforms to evaluate performance enhancement criteria that articulated tails can provide. The leg mechanism is composed of two serially connected four-bar mechanisms that utilize kinematic constraints to maintain a parallel orientation between the flat foot and body without the use of an actuated ankle. A passive suspension system integrated into the foot enables the dissipation of impact energy and maintains a stable four point of contact support polygon on both flat and uneven terrain. The modular design enables the construction of reduced-DOF quadruped and biped robots that are used as experimental platforms to test the articulated tails abilities in enhancing maneuverability and stabilization.

- Dynamic Modeling and Control: The dynamic formulations of articulated tails onboard legged robots derived in this dissertation are used to select optimal ranges of tail mass and length ratios to produce effective inertial adjustment of legged robots. Data on biological specimens validated optimization results by demonstrating that animals, that utilize their

tails for inertial adjustment applications, satisfy the optimal ranges defined based the proposed analysis. The dynamic formulations were then used to derive a maneuvering controller consisting of a Path Planner to plan tail trajectories for goal oriented maneuvering behavior, and a Tail Motion controller was designed and implemented to decouple manipulator dynamics and control an articulated tail to track the planned tail trajectory. The control approach was evaluated using experiments and simulations of the robotic systems composed of reduced-DOF quadruped and biped robots to demonstrate the articulated tail mechanisms abilities to enhance stabilization and maneuvering [20, 21].

1.4 Selected Publications

Disclosure: This dissertation uses content directly adapted from the following publications:

Journals

1. **W. Saab**, W. Rone, and P. Ben-Tzvi, "Robotic Tails: A State of The Art Review," *Robotica (submitted Nov. 2017),* 2018.

2. **W. Saab**, W. Rone, A. Kumar, and P. Ben-Tzvi, "Design and Integration of a Novel Spatial Articulated Robotic Tail," *Transactions on Mechatronics (submitted Oct. 2017),* 2018.

3. **W. Saab**, W. Rone, and P. Ben-Tzvi, "Discrete Modular Serpentine Robotic Tail: Design, Analysis and Experimentation," *Robotica,* 2018, Published online, March 2018. doi:10.1017/S0263574718000176.

4. **W. Saab,** W. S. Rone, P. Ben-Tzvi, "Robotic Modular Leg: Design, Analysis and Experimentation", ASME Journal of Mechanisms and Robotics, vol. 9, no. 2, pp. 024501: 1-6, April 2017. doi: 10.1115/1.4035685.

5. W. Rone, **W. Saab**, A. Kumar, and P. Ben-Tzvi, "Controller Design, Analysis and Experimental Validation of a Robotic Serpentine Tail to Stabilize and Maneuver a Quadrupedal Robot," *Journal of Dynamic Systems Measurement and Control (submitted Nov. 2017),* 2018.

Conferences

1. **W. Saab**, Y. Jiteng, and P. Ben-Tzvi, "Modeling and Control of an Articulated Tail for Maneuvering a Reduced Degree of Freedom Legged Robot," in *International Conference on Intelligent Robots and Systems (Submitted March 2018)*, 2018.

2. **W. Saab** and P. Ben-Tzvi, "Maneuverability and Heading Control of a Quadruped Robot Utilizing Tail Dynamics," in *Dynamic Systems and Control Conference*, Va, USA 2017, pp. V002T21A010: 1-7.

3. **W. Saab** and P. Ben-Tzvi, "Design and Analysis of a Discrete Modular Serpentine Robotic Tail for Improved Performance of Mobile Robots," in *International Design Engineering Technical Conferences and Computers and Information in Engineering Conference* Charlotte, NC, 2016, pp. V05AT07A061: 1-8.

4. **W. Saab** and P. Ben-Tzvi, "Design and Analysis of a Robotic Modular Leg," in *International Design Engineering Technical Conferences and Computers and Information in Engineering Conference* Charlotte, NC, USA, 2016, pp. V05AT07A062: 1-8.

1.5 Dissertation Structure

The dissertation is structured as follows:

Chapter 1 provides a summary and outlines the main objectives and contributions of the proposed work.

Chapter 2 presents a comprehensive state-of-the-art review of the mobile robots that utilize robotic tails for inertial adjustment applications with tabular analysis that compares design attributes of previous work and highlights the significant results and challenges that have motivated this research.

Chapter 3 explores the design space of under-actuated, articulated robotic manipulators to identify design challenges and useful design criteria that have inspired the proposed tail mechanisms. Based on this investigation, the mechanical designs of two articulated tail mechanisms are presented. These tail designs represent the first major contributions to this dissertation where the novelties and design oriented advantages relative to existing work are highlighted within the discussions.

Chapter 4 presents the kinematic and dynamic modeling of the R3-RT mechanism that is used to compute generated inertial loading, reactive forces and moments about the base of the tail. Simulated case studies are then presented to analyze the impact of tail motion and tail configuration parameters on inertial loading profiles. Experimental results using an integrated prototype demonstrate accuracy and repeatability and the enhanced inertial loading capabilities of articulated tails over previously implemented pendulum-like tails.

Chapter 5 presents the kinematic and dynamic modeling of the DMST mechanism that is used to compute generated inertial loading, reactive forces and moments about the base of the tail. Simulated case studies are then presented to analyze the effect of varying design and tail trajectory parameters on inertial loading profiles resultant from tail motions. Experimental results using an integrated prototype demonstrate accuracy and repeatability and the capacity of inertial loading capabilities and are used to validate both the kinematic and dynamic models.

Chapter 6 discusses the challenges in design and control of conventional legged robots. Existing reduced-DOF leg mechanisms are reviewed that reduce the overall design and control complexity of legged robots. However, the majority of existing solutions utilize point of contact feet that introduce challenges in developing robots that can satisfy walking criteria described as producing stable forward and turning gaits that maintain constant body height, and orientation during locomotion. Therefore, a novel reduced-DOF leg mechanism is proposed to construct both a quadrupedal and bipedal experimental platform to evaluate the performance enhancement capabilities that attached articulated tails can enable. Foot trajectory and sequencing are presented to enable a stable trot walking gait. Kinematic and dynamic models are then derived to aid the design procedure by selecting appropriate motors that satisfy operational requirements to produce the desired walking gaits. However, to satisfy all the aforementioned walking criteria, the articulated tails must be implemented onboard the quadruped and biped robot to augment performance of maneuvering and stabilization.

Chapter 7 derives the dynamics of a legged robot with an attached articulated tail. These dynamic formulations are used to select optimal ranges of tail mass and length ratio to produce effective inertial adjustment of the legged robot due to tail motions. Data on biological specimens was found to satisfy the optimal ranges defined based on analysis. The dynamic formulations were then used to derive a maneuvering controller consisting of a Path Planner to plan tail trajectories for goal oriented maneuvering, and a Tail Motion controller to track the desired tail trajectory.

Chapter 8 presents the experiments and simulations that consist of an articulated tail prototype attached to a virtually simulated quadruped and biped model to evaluate the performance of the tails in enabling enhanced stabilization and maneuvering behaviors. This chapter demonstrates that the proposed tails, R3-RT and DMST, attached to the reduced-DOF quadruped and biped robot, respectively, can produce the desirable set of walking criteria (described in Chapter 6) that is comparable to the performance of conventional legged robots.

Chapter 9 discusses future work research directions and applications enabled by the proposed work in this doctoral dissertation.

CHAPTER 2: LITERATURE REVIEW

This chapter reviews the state-of-the-art in robotic tail design and implementation intended for inertial adjustment applications onboard mobile robots. Inspired by biological tail usage found in nature, engineers have proposed the usage of robotic tails that provide a separate means to enhance stabilization, and maneuverability from the mobile robot's main form of locomotion, such as legs or wheels. Research over the past decade has primarily focused on implementing single-body rigid pendulum-like tail mechanisms to demonstrate inertial adjustment capabilities onboard walking, jumping, and wheeled mobile robots. Recently, there has been increased efforts aimed at leveraging the benefits of continuum tail mechanism designs to enhance inertial adjustment capabilities and further emulate the structure and functionalities of tail usage found in nature. This chapter discusses relevant research in design, modeling, analysis, and implementation of robotic tails onboard mobile robots, and highlights how this work is being used to build robotic systems with enhanced performance capabilities.

The objective of this chapter is to present and compare research contributions made to robotic tail design, analysis, and implementation onboard mobile robots for inertial adjustment applications. While there are examples of inertial adjustment of legged robots and mobile platforms using torsos [22], limbs [23] and robotic manipulators [24], this review will focus on active mechanisms that mimic functionalities of biological tails observed in nature. The objective is to summarize the most recent and relevant advances in this field and outline the limitations and challenges pertaining to inertial adjustment applications of mobile robots via robotic tails. This chapter will outline progress and identify key challenges that lay ahead to justify the design and analysis of the work proposed in subsequent chapters of this dissertation.

2.1 Inertial Adjustment Mechanism Technology

Robotic engineers and scientists inspired by nature often face a scenario where meeting design requirements using traditional engineering approaches becomes challenging. In the case of a biological tail used for inertial adjustment applications, faithfully mimicking a biological structure in terms of design alone has not been demonstrated as a realistic option since animals have evolved

over millions of years to exploit structural and organizational principles spanning multiple physical scales and operational modes to realize functional performance gains in an efficient manner [25].

From an engineering perspective, the fundamental principles of an inertial adjustment mechanism is to offer the capability to adjust the center-of-mass (COM) location and generate control forces and moments about its attachment point to adjust the system orientation. These basic requirements have led to vast amounts of research to develop inertial adjustment mechanism technologies to meet these needs. However, for applications onboard mobile robots, the feasibility of such technologies must be carefully considered.

Engineered solutions for inertial adjustment mechanisms can be categorized based on their principles of operation: (1) substrate interaction mechanisms propel the surrounding environment to produce propulsive forces such as thrusters, gas jets, fins, turbojets and turbofans [26] [27], (2) translational mechanisms displace a reaction mass to adjust COM location [28], (3) symmetric rotational mechanisms provide a reactive moment (no forces), such as reaction wheels [29], to adjust orientation, and (4) asymmetrical rotational mechanisms, such as pendulums (i.e. robotic tails), provide COM adjustments and generate control forces and moments.

Although category 1 mechanisms have demonstrated highly capable inertial adjustment capabilities onboard satellites, airplanes and spacecraft, the requirement of compressors and fuel make practical implementation on board mobile robots challenging. Similarly, category 2 mechanisms rely on the translational stroke length of the reaction mass and requires a large foot print onboard a relatively compact mobile robot for significant inertial adjustment contributions. Therefore, the feasibility of category 3 and 4 mechanisms has been studied for inertial adjustment applications of mobile robots.

A category 3 reaction wheel consists of an axisymmetric mass that is capable of continuous rotation about a single axis of rotation and is used to impart a reactive moment about its attachment point. Although they can be designed to fit in small volumes, they are limited by the angular velocity of the actuator and mass constraints [30]. Category 4 pendulums are capable of generating both control forces and moments in addition to adjusting COM location. They can be designed with high inertia while maintaining a constant mass due to the quadratic relationship between pendulum length and effective inertia. However, pendula are often limited to a maximum range of motion due to potential contact with the environment or robot during operation.

In the work presented by Briggs et. al. [31], the results of comparative analysis between mobile robot implementations of a reaction wheel and a robotic tail, in the form of a single-body rigid pendulum, are summarized as follows: (1) the longer spatial dimension of a robotic tail provides the advantage of a greater moment of inertia at the cost of a constraint on maximum allowable relative rotation, (2) a reaction wheel is appropriate when there are tightly confining geometry constraints and the time of interest is long due to its ability to continuously rotate, and (3) for an equivalent power input, effective moment of inertia and short time span, a robotic tail can produce a significantly higher angular impulse to affect the attached mobile robot. In a separate study presented by Machairas et. al. [30] that analyzed a pendulum-like tail and reaction wheel onboard a quadruped robot, for equivalent inertial properties and time span of motion that result in an equivalent heading angle adjustment in the yaw direction, results indicated that: (1) less torque is required for the robotic tail motion because the inertial force at the tail base also contributes to the net torque relative to the system COM, and (2) the motor needs to run at a much higher speed in the reaction wheel case; as a result, for the same net rotation, more power is required by the motor. The results from both [30, 31] have concluded that robotic tails are the optimal means of inertial adjustment for mobile robotic applications.

2.2 Robotic Tails

This section reviews the design and implementation of robotic tails onboard mobile robots for inertial adjustment applications categorized by structural design and means of operation. Section 2.2.1 reviews work pertaining to single-body rigid pendulum-like tails that operate in planar (2.2.1.1) and spatial (2.2.1.2) workspaces. Section 2.2.2 presents recent trends into soft robotics that have led to mechanism designs that form continuum structures and closely mimic the motions and functionalities of biological tails found in nature. The aim of this section is to provide a comparative analysis and highlight the benefits and results of the proposed tail mechanism designs found in literature.

Many of the robotic tails proposed in the literature draw inspiration from a diverse variety of animals such as cheetahs [31-34], kangaroos [5, 35-37], fish [38, 39], lizards [6, 40, 41], and dinosaurs [7, 42]. To facilitate a comparative analysis of prior research into robotic tails, a sample of previous tail designs and their physical properties are collected in Table 2.1. In terms of mechanical design, the majority of research has focused primarily on single-body planar

pendulums and covers a wide range of masses (4 to 700 g) and lengths (73 to 500 mm). Planar tails operate in a single-DOF either in the pitch [6, 35, 37, 40, 43-47], yaw [42, 48-50], or roll-direction [33]. Spatial pendulum-like tails are two-DOF mechanisms that operate in a combination of planes by utilizing active pitch and yaw DOFs [31, 36, 41]. Planar tails provide enhanced performance about a single body-axis with the advantage of simpler design and implementation. Spatial tails greatly increase workspace and provide multi-axis enhanced performance capabilities, but require increased actuator unit design complexity and control. The continuum tails' [38, 39, 51] earliest implementations dating back to the year 2014, not shown in Table 2.1, are designed to closely emulate the natural motions and functionalities of biological tails and utilize various forms of actuation such as cable systems, pneumatic pressure, and mechanical layer jamming.

Functionally, these tails may be classified as aiding stabilization, maneuvering, propulsion or manipulation. Tails for stabilization include static applications of COM adjustment that aid passive quasi-static walking [50], and dynamic applications for disturbance rejection [31], dynamic running [42], pitch adjustment [6, 7, 37, 40, 44, 45, 47, 52], stabilization for high-speed maneuvers [32, 33], and attitude control [31, 36, 41]. Tails for maneuvering enable yaw-angle turning [48, 49]. Tails for prolusion have demonstrated for underwater swimming applications [38, 39]. Tails for manipulation enable environmental contact to provide an additional supporting limb [5, 42].

Table 2.1: Comparison of robotic tail designs, and actuation properties.

System	[37]	[50]	[6, 40]	[48]	[33, 46]	[35]	[41]	[32]	[36]
Year	1991	2008	2012	2012	2013	2014	2013	2015	2015
Tail Mass (g)	-	700	17	4	400	371	70	400	150
Tail Length (mm)	-	150	103	115	500	177	73	500	300
Rated Motor Power (W)	-	5.5	4	2.5	120	19	1.75	70 ea.	-
Max Speed (rpm)	-	6	3000	400	275	240	320	137	353
End Effector Workspace (Deg)	-	180	255	265	224	220	135/135	70/180	180/180
Mechanical Design	Planar						Spatial		
	Single-Body Rigid Pendulum								

- Not Reported.

2.2.1 Single-Body Rigid Pendulum Tail Mechanisms

As pointed out in Table 2.1, pendulum tails can either be classified as planar tail mechanisms reviewed in section 2.2.1.1 or spatial tail mechanisms reviewed in section 2.2.1.2.

2.2.1.1 Planar Tail Mechanisms

Planar tails, examples of which are shown in Fig. 2.1, provide enhanced performance about a single axis with the advantage of simple design and implementation. Based on an extensive literature review, the first system that appears to have utilized an inertial tail was the Uniroo robot [37] composed of a single leg constrained to hop along a circular path and a pitch DOF tail used to counterbalance leg motion, shown Fig. 2.1(A). The authors used experimental observations and data to modify the control architecture and the tail's moment of inertia to achieve desirable behavior. The robot demonstrated a forward hoping velocity of 1.8 m/s. Based off this work, a number of pitch DOF tails have been further analyzed and implemented on numerous robots for dynamic mid-air pitch adjustment. Liu et. al. investigated a kangaroo robot [35], shown in Fig. 2.1(B), with two synchronized circular arc-shaped legs used to produce forward hopping motion while an active tail compensated for undesired angular momentum. The authors investigated performance of a stationary tail, and an active pitch DOF tail using both open-loop control (i.e.,

pre-calculated trajectories) and closed loop control (updating tail trajectories using sensor data). Results indicated that an active tail can reduce pitch variation by up to 50 %. With the open-loop active tail, the body pitch RMS error of the robot reduced by 52% in comparison to the robot with stationary tail. With the closed-loop active tail, the value is further reduced by 43%.

By studying a lizard's jump, transitioning between horizontal and vertical surfaces [7], Chang-Siu, Johnson, Libby et. al. explored the design space and performance enhancements a pitch DOF tail can provide Tailbot [6, 40], shown in Fig. 2.1(C), for mid-air pitch self-righting. Conservation of angular momentum of the robotic system, modeled as two rigid bodies (mobile robot and tail) connected by a revolute joint imposed a dimensionless index of rotational efficacy upon which the tail can be designed and optimized in terms of tip mass and length specifications for mobile robots of various sizes and weights [53]. Further analysis demonstrated that: 1) the duration of body reorientation depends upon the acceleration of the tail relative to the body, and 2) the power density of the tail's actuator must increase quadratically with the robot's body length in order to achieve the same maneuver in the same relative time span of the tail motion. These results indicate that inertial adjustment gets more expensive for larger size scaled robots; therefore, larger robots may suffer from reduced tail-aided performance or must dedicate a larger proportion of total body mass and power to tail actuation. Experimental results in this work demonstrated how the tail enables rapid pitch reorientation of the body up to 90° with relatively low tail tip mass ($10\% - 20\%$ of the robot body mass). The authors later implemented a similar tail on X-Rhex robot [44, 47], shown in Fig. 2.1(D), to demonstrate the robot's enhanced survivability in running off an elevated ledge and dynamically adjusting its pitch to land on its feet enabled via closed-loop, tail-aided body pitch control. A similar functionality was demonstrated by Zhao et. al. on a miniature 28 gram robot called the MSU Jumper [45, 52], shown in Fig. 2.1(E), that can translate using wheels, jump over obstacles using spring loaded legs, and perform aerial pitch adjustments using an active tail. Therefore, the robot can control its landing posture to protect it from damage.

Tails that operate in the yaw DOF have been proposed to enhance maneuverability and stabilization of mobile robots. Kohut et. al. proposed a palm-sized, 45 gram legged robot called TAYLRoACH [48, 49], shown in Fig. 2.1(F), to investigate the maneuverability improvement a tail can provide in terms of turning without reducing the its forward running speed. Modeling of the robotic system assumed that the tail torque occurs as soon as the tail is actuated and overwhelms static friction, causing a full-body rotation opposed by dynamic sliding friction at the

feed. However, this model did not consider the effects of translation resulting from inertial forces generated by the tail. Using gyroscope sensory feedback, a bang-bang controller was developed to apply maximum motor torque within 5° of the desired body yaw angle. The robot demonstrated 90° turns up to 360°/sec with an RMS error up to 13.2°. Inspired by recent biomechanics research of the cheetah [54], Patel and Braae analyzed the enhanced stabilization a tail can provide the wheeled robot Dima, shown in Fig. 2.1(G), in terms of rapid forward motion acceleration/braking [46], and turning [33]. For rapid acceleration/braking, the authors proposed a longitudinal maneuver template to model the complex control strategies of animal's hyper-redundant task-level behaviors using reduced-order models [55] that consisted of two rigid bodies, tail and robot, capable of rotating about a grounded joint where acceleration/braking forces were considered to be external forces acting on the system. In this case, the tail was used to maintain zero pitch angle during instances of rapid acceleration and deceleration. For rapid turning, a Lagrangian method was used to model the system in the lateral plane where the robot was assumed to be rotating in the roll direction about a grounded joint. The centrifugal force resulting from high-speed turning was modeled as a disturbance to the system and a controller was developed to maintain a zero roll angle using counteractive tail motions. The authors utilized the analytical models of the system to select an optimal tail mass and actuator gearbox reduction ratio to maximize the resultant body angular adjustment resulting from a tail motion, and then studied the effects of a tailed and tailless robot. Both simulation and experimental results of this work indicated that the addition of the tail enabled the robot to perform up to a 40% increase in lateral acceleration and a 50 % increase in forward acceleration, without toppling over in comparison, to the tail-less version; therefore, enabling high-speed maneuverability. The authors then designed a new actuation unit to combine both pitch and yaw tail motions to construct a 2-DOF spatial tail [32] to better approximate the conical motion of tail usage of the cheetah and impart a roll torque, about a single axis, on the Dima robot; however, in terms of functionality the goal was to enhance turning of the robot about a single axis in the lateral direction. A tail controller was then developed to generate tail motions that constrained the tail workspace to a cone of specified width. Experimental results indicated that, on average, a tail-less system could only perform a turn at 6 m/s whereas the tailed system could initiate turns at 7 m/s since the tail can provide up to 70 % more lateral acceleration.

Berenguer et. al. proposed a passive, compliant bipedal robot called Zappa that is capable of walking using only one actuator that controls yaw rotation of a tail [50], shown in Fig. 2.1(H).

The authors demonstrated that the gait length and forward walking speed of the robot can be controlled by varying the frequency of tail oscillation that adjusts the robot's COM position to fall within the left/right support polygon. Results highlight the potential simplifications a tail can provide legged robots in terms of reduced mechanical design and control complexity. Takita et. al. proposed a bipedal robot called TITRUS [42], designed to realize a practical mobile working platform. Both a pendulum-like neck and tail mechanism, attached to universal joints each controlled by two coupled differential drive motors, were used to swing the inertial appendages left and right in a horizontal plane (about a single axis) to walk statically and run dynamically by adjusting its projected COM and zero-moment point within the robots support polygon. This work demonstrates the first functionality how an inertial appendage with a spatial workspace can be used to provide a stable tripod like structure while the neck can potentially perform tasks of manipulation or surveillance.
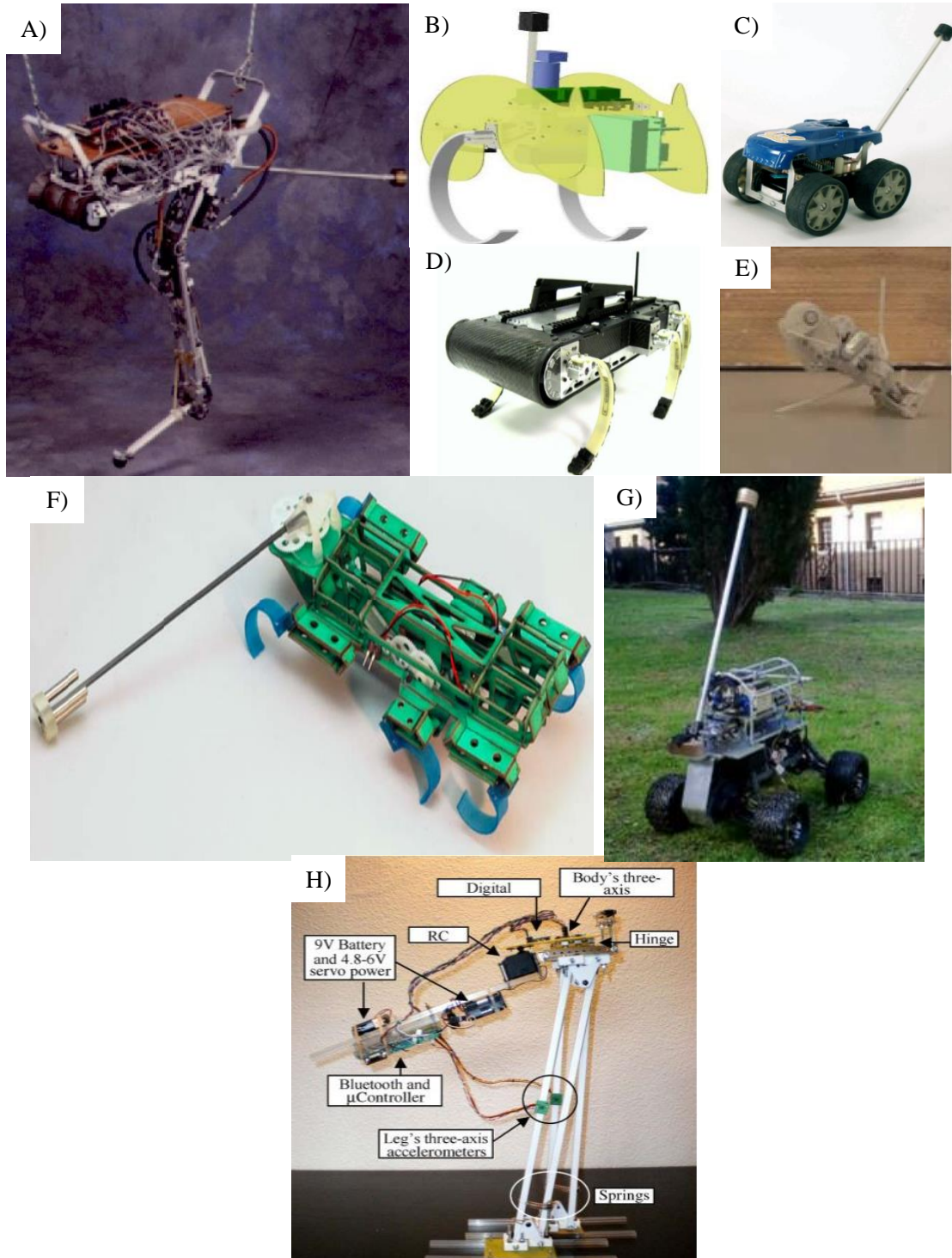
Figure 2.1: Planar, pendulum-like tail mechanisms: A) Uniroo robot , B) Kangaroo robot [35], C) Tailbot [6, 40], D) X-Rhex [44, 47], E) MSU Jumper [45, 52], F) TAYLRoACH [48, 49], G) Dima [33, 46], and H) Zappa [50]

2.2.1.2 Spatial Tail Mechanisms

Spatial, single body rigid pendulum tails, shown in Fig. 2.2, have been proposed that greatly increase workspace and provide enhanced multi-axis capabilities at the cost of increased actuator unit design and control complexity. Although structurally similar to planar pendulum-like tails reviewed in section 2.2.1.1, the main contributions of spatial pendulum-like tails falls within algorithm design to control the tail's pitch and yaw DOFs simultaneously to achieve a desired functionality. These tails have been used to experimentally demonstrate dynamic applications including disturbance rejection [31], mid-air attitude control, [41] and energy regulation [36].

Inspired by video footage of a cheetah observed whipping its tail from side to side during a high-speed chase of its prey, Briggs et. al. hypothesized that the tail provides a reactive moment to help roll the animal's body in mid-air to assist in turning motion. In this work, a 2-DOF pendulum-like tail attached to the MIT Cheetah [31], shown in Fig. 2.2(A), was modeled during midair-flight as two rigid bodies, tail and robot. The authors then developed a controller to reorient the body using tail motion by: 1) defining an Euler axis along which the robot should rotate to the desired orientation, 2) computing the angular rotation needed to achieve the desired orientation, 3) calculating the current angular velocity of the body, 4) defining the desired angular velocity at the end configuration, 5) determining the desired angular momentum with the desired angular velocity, 6) computing the desired change in angular momentum to compute the desired torque tail input, and 7) projecting the desired torque on the achievable space of torques along the axis of the tail actuators. In this analysis, only inertial moments were considered for inertial adjustment applications; inertial forces generated by the tail were neglected due to the complexity of its consideration since these forces either aid or hinder rotation of the robot based on its instantaneous state as discussed by the authors. The simulated controller failed to achieve a desired orientation when the initial tail orientation was arbitrarily selected, but was successful when the initial tail orientation was optimized. The authors then experimentally demonstrated how the tail can be used to reject external disturbances, by swinging it in an opposite orientation of its body rotation, to prevent the robot from tipping over while in contact with the ground.

Chang-Siu et.al. proposed a control scheme for attitude control of a falling, 2-DOF Tailbot, shown in Fig. 2.2(B), with the tail capable of rotating in the pitch and yaw directions [41]. By choosing a body angular velocity vector parallel to the axis of error rotation, the controller steers the robot towards its desired orientation. However, the attachment point of the tail to the robot was

assumed to be at the COM, therefore neglecting the effects of generated inertial forces on the orientation of the robot. The proposed scheme was accomplished through feedback laws as opposed to feed forward trajectory generation, and demonstrated a fair robustness to model uncertainties. The authors implemented the control approach on a simple controller on a small (175 g) robot platform. Experimental trials, after inertial adjustment using the tail, demonstrated an angular orientation error up to 18° attributed to friction in the inexpensive motors and lack of an integrator in the controller.

De and Koditschk proposed the Penn Jerboa [36], shown in Fig. 2.2(C), a passive-compliant 4-DOF tailed monoped fastened to a boom to restrict motion in the sagittal plane. The platform's locomotion is powered by the hip motor that adjusts the leg touchdown angle in flight and balance in stance, along with a tail motor that adjusts body shape in flight and drives energy into the passive leg shank spring during stance. Although the 2-DOF tail is spatial, spatial inertial reorientation analysis was presented but was only demonstrated for the robotic system constrained in the sagittal plane with the tail operating in the pitch DOF. The authors adopt a template-anchor framework [55] to represent this machine's 4-DOF steady sagittal plane running as the hierarchical composition of the low DOF constituents described as: 1) tail energy pump, 2) Raibert Stepping, 3) Raibert pitch correction, and 4) shape reorientation. The authors apply the four decoupled 1-DOF control laws associated with these isolated templates directly to the (highly dynamically coupled) physical platform and demonstrate empirically steady sagittal plane running whose body motions reveal, when viewed in the appropriate coordinates, striking similarity to the corresponding isolated 1-DOF constituents.
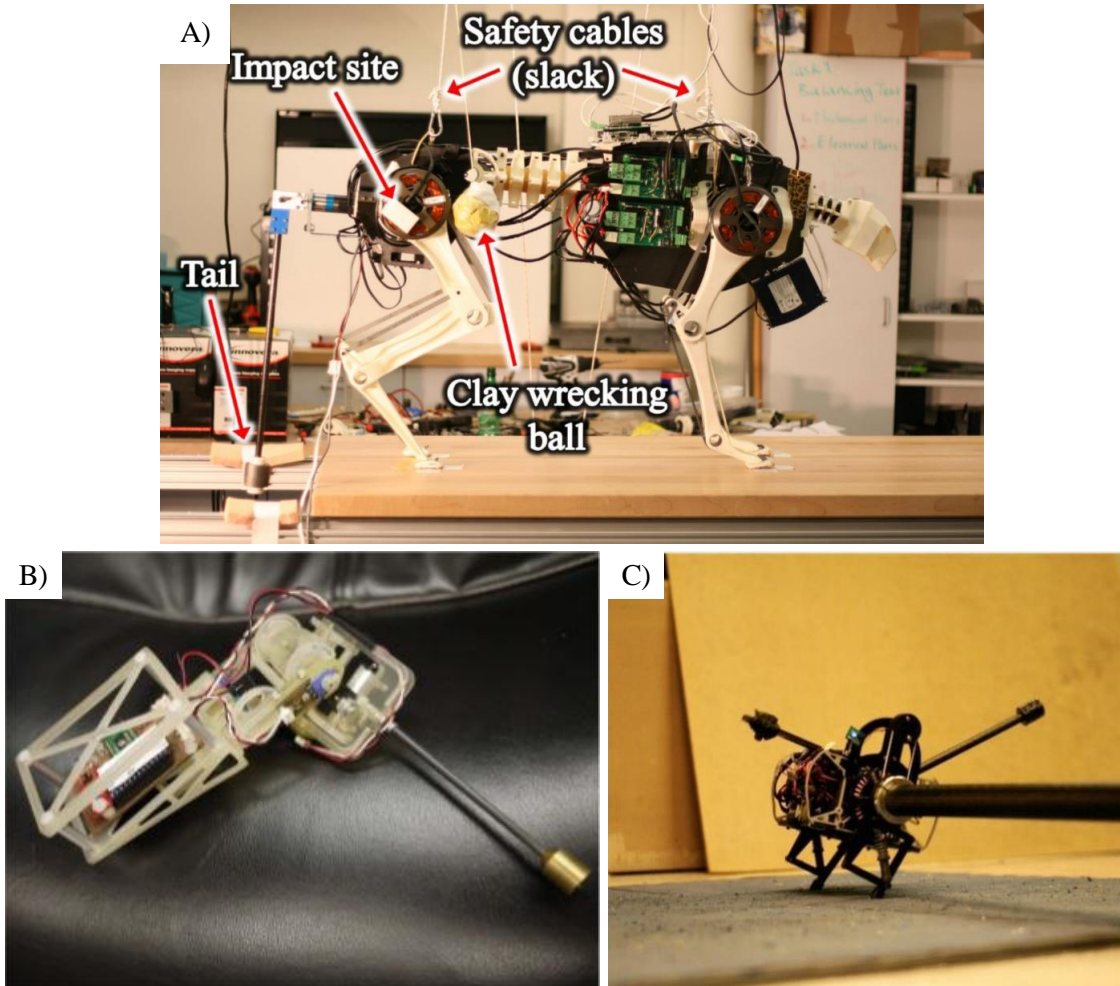
Figure 2.2: Spatial, pendulum-like tail mechanisms: A) MIT Cheetah [31], B) 2-DOF Tailbot [41], and C) Penn Jerboa [36].

2.2.2 Continuum Tail Mechanisms

A recent surge of interest into soft robots, capable of forming continuous curvatures, has been motivated by the perceived observations and performance of traditional rigid body robotic manipulators that exhibit a mechanically a stiff interface with the surrounding environment [56]. The body compliance of soft robots is a salient feature found in many natural systems that offers inherent robustness to uncertainty, adaptability to environmental uncertainties and the capacity to distribute forces at the cost of reduced repeatability and accuracy [57].

Rone et. al. proposed the use continuum robotic tails for inertial adjustment applications [51], shown in Fig. 2.3(A). The tail was composed of eight disks rigidly mounted along an elastic core. The two-segment structure, capable of forming two curvatures, also called mode-shapes, was

composed of six rods that provide structural support. Three rods were terminated at the fourth and eighth disks in each segment. Two active rods are displaced via linear motors to create planar tail curvatures. The authors also proposed a two segment cable-driven variation, driven by three linear motors, capable of forming spatial curvatures. These preliminary prototypes were used to validate a novel method of dynamic modeling that captures curvature variations along segments using the principle of virtual power [58, 59]. For stabilization and maneuvering applications, the authors analyzed the impact of both trajectory and design factors on the loading profiles about the tail base resulting from tail motions of the continuum structure. Trajectory factors considered include the configuration shape, speed, bending magnitude and bending plane angle. Design factors considered for a fixed mass tail include segment length(s) and mass distribution. Results indicated that a shorter segment 1 length, in a two segment continuum tail, provides a greater range of motion of the tail tip and will enable more rapid tail motions due to less required actuation displacement, and allocating a larger mass concentration in segment 2 towards the tip provides larger bending moments and greater fidelity of control over the applied moment. Furthermore, the two configuration shapes in the tail structure was shown to increase the manifold of inertial loading about the base of the tail by actuating various configuration shapes during tail motions.

However, challenges associated with scaling the continuum designs up to the macro-scale led the authors to consider other tail structures composed of rigid bodies – presented in this dissertation. First, the uniform elasticity of the single continuum core did not allow for the tail's stiffness to vary in different directions (i.e., vertical and horizontal) or along the structure. Higher stiffness to counteract gravity in the vertical direction would be more desirable, along with higher stiffness at joints closer to the tail base, as they have to support larger gravitational moments. Second, for uniform horizontal bending with minimal actuation, it is desirable to have a low, consistent horizontal stiffness. In addition, on the macro-scale, when the continuum structure bends out of the plane, the core's torsional deflection causes undesired sag in the tail that must be accounted for in the modeling and further impedes uniform bending. Third, the continuum robot's theoretically infinite-DOF joint space provided significant challenges in planning strategies for real-time interoceptive sensing.

Marchese et. al. proposed an autonomous soft-bodied fish robot that is both self-contained and capable of rapid, continuum-body motion[38]. The robot, shown in Fig. 2.3(B), is composed of a rigid body structure that houses the electronics, sensors, and a fluidic actuation unit. The fish

tail is composed of fluidic elastomer actuators that expand and contract with fluidic pressure; thus, creating left or right bending curvatures. The major implications of this work demonstrate how the continuum tail can emulate natural motions in forward swimming and rapid escape response maneuvers in the form of C-shape heading angle turning with a maximum measured rate of 320 °/s. The kinematics and controllability of the soft-bodied robot during escape response maneuvers were shown to have similar input–output relationships to those observed in biological fish. In a later piece of work by Liu et. al., a soft, continuum-bodied robotic fish [39] with a tail actuated via three servo motors controlling discrete joints demonstrated a C-shape escape maneuver with a maximum measured heading angle turning rate of 120 °/s. The comparison of measured yaw rate maneuvering between [38] and [39], indicate one of the very first quantitative experimentally validated performance advantages that a continuum tail actuated via pneumatic pressure can provide versus a conventionally actuated fish tail mechanism.

To mimic the functionalities of kangaroo tail usage in nature, Santiago et. al. proposed a continuum robotic structure that can modulate compliance via mechanical layer jamming[5]. The mechanism utilized a novel mechanical approach to layer jamming, shifting away from fluidic actuation and vacuum pressure as originally proposed in [60]. The tail, shown in Fig. 2.3(C), is composed of a proximal and distal section, each driven by three active cables routed through coupling disks and terminated at the section ends. Displacement of these cables enables spatial tail curvatures. The structure is composed of an underlying spring back bone that runs along the manipulator's length. The layer jamming mechanism is composed of laser cut flaps enclosed within a nylon braided sheath, similar to that used for artificial muscles. Extension/pulling of the sheath via tendons causes it to shrink in diameter resulting in additional friction due to the internal flaps rubbing against the spring steal core; therefore, stiffening the structure. The authors presented a novel application of the tail attached to a stuffed kangaroo toy. In a stiff state, the tail was used to provide an additional anchoring limb to enable additional stability while standing on its hind limbs. In the unstiffened state, the kangaroo was unable to support its weight and slowly collapsed to the ground. As part of future work, the authors plan to taper the diameter of the tail to better emulate a kangaroo tail structure and functionality. Contrary to previous implementation of robotic tails that exploit tail motions to aid inertial adjustment applications, this work represents the first application into studying environmental contact, and variable softness/compliance of a tail. The utilization of a compliant tail onboard a hopping kangaroo robot may led to future investigations

23

of energy conservation to produce efficient locomotion [61] as proposed in a biological study of these animals by Kram and Dawson. In their work [62], it was stated that the extremely long Achilles tendon in a kangaroo's tail acts as a "pogo stick" that stores and releases energy while hopping; in effect, it is nearly impossible to tire out a kangaroo while it hops over level ground.
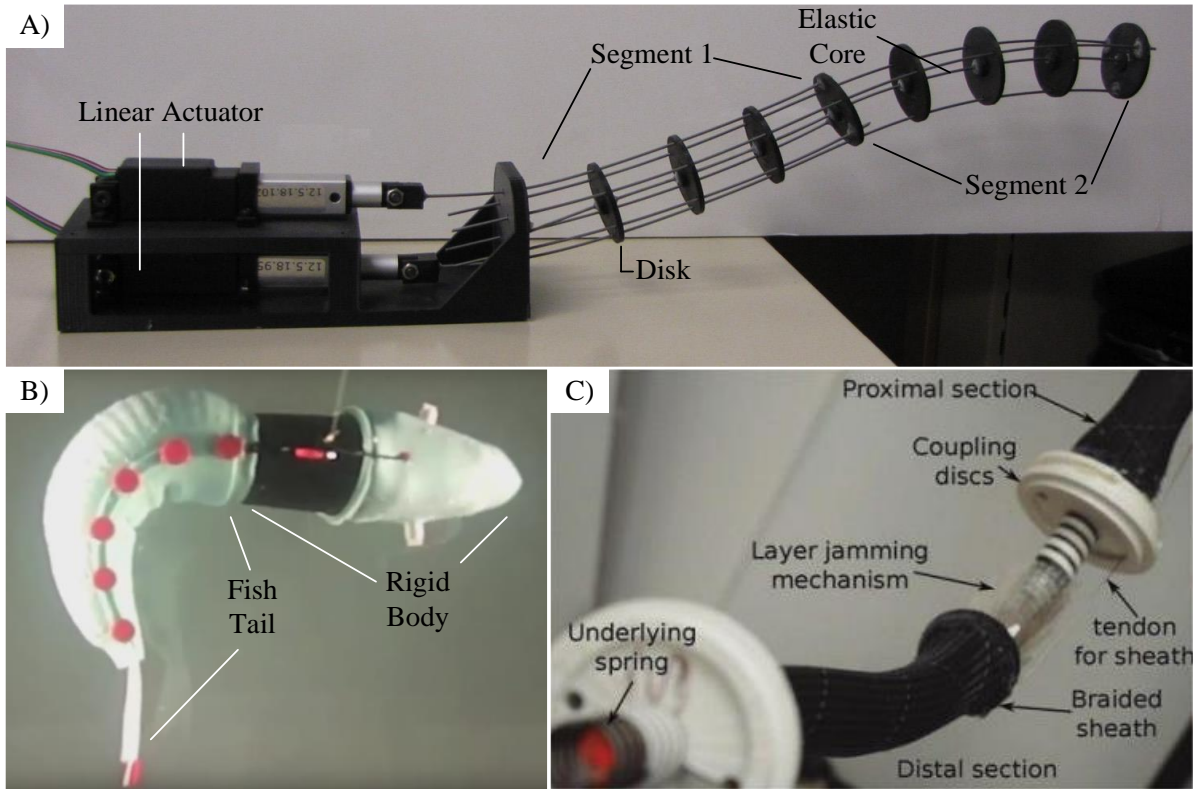
Figure 2.3: Soft robotic tail mechanisms: A) Continuum robotic tail [51, 58, 59], B) Autonomous soft robotic fish [38] (image courtesy of MIT News[63]), and C) Continuum kangaroo tail actuated via mechanical layer jamming [5].

2.3 Challenges

Since the early implementations of robotic tails, mechanical design, modeling, and control aspects have been continuously improving. The extent to which the promise of robotic tails can be realized depends on the robustness of its design, the accuracy of modeling and the effectiveness of the control system to demonstrate the full range of functionalities of tail usage observed in nature that involves both inertial adjustment capabilities (stabilization, maneuvering) and manipulation. However, several key steps are necessary for robotic tails to realize their full potential that can be broken down into challenges in mechanical design, modeling and control.

2.3.1 Mechanical Design Challenges

Performance of robotic tails is highly dependent on its mechanical design. To date, with reference to Table 2.1, tail designs have evolved from planar to spatial pendulums and most recent progress has shifted to continuum mechanisms. These advancements have been coupled to enhanced workspace for more desirable effects of inertial adjustment applications. However, an optimal and general purpose tail design has yet to be proposed. The fundamental challenges that govern this problem include:

- Design optimization and considerations on the minimal number of active DOF's required to produce a spatial workspace with distributed motion about its tail length for enhanced inertial loading capabilities. The added mass of the actuators contributes a change to system dynamics and is directly related to the cost inertial adjustment capabilities.
- Limits on strength, and precision of the tail mechanism that can perform both dynamic motions for inertial adjustment applications and provide the accuracy required for quasi-static applications that involve precise COM positioning for static stabilization and manipulation.
- Limits on motor power, and energy efficiency to maintain a cantilevered configuration with minimal energy consumption

Given the broad base of tail designs presented in the literature, rigorous comparative analysis is needed of the merits and shortcomings of these designs in relation to one another and in relation to the various types of mobile robotic platforms (e.g., biped, quadruped, wheeled) on which they may be deployed.

2.3.2 Modeling and Control Challenges

Although modeling and control approaches have been developed and implemented over a wide range of applications, inertially adjusting a mobile robot using a robotic tail is a challenging task due to modeling of a highly coupled, nonlinear dynamic, under actuated system. Since the tail attachment point to a mobile robot is usually located at its rear end, offset from the robot COM, during inertial adjustment applications, tail motions generate both a reactive moment and lateral forces, caused by eccentric mass distribution of the tail that are transferred to the mobile robot.

These forces also induce a moment due to this positional offset that introduces challenges in modeling and control. Depending on the state at each instant, this may either augment or diminish the resultant moment produced by the tail, complicating analysis considerably. This problem requires optimization to find good control policies. To address these challenges, common methods employed by researchers include simplifying assumptions that have neglected the effects of inertial forces [6, 31, 33, 40, 44, 46-49] on the mobile robot and have constrained the robotic system dynamics to a single plane [35-37]. The challenges that remain to be addressed both in low-level control and high-level planning to overcome realistic constraints include:

- Algorithms for maneuvering that also account for the stability of the system that may be compromised during tail motions.
- Algorithms for computing an optimal tail trajectory with a constrained workspace that considers the effects of both inertial forces and moments to maximize desirable effects of inertial adjustment.

Broadly speaking, efforts are needed to reconcile the effects of a tail within existing frameworks for analyzing the stability of a mobile robot. In doing so, the stability analysis can be used to generate tail control inputs to generate inertial loading and adjust gravitational loading in a similar manner as leg control inputs are formulated to generate desired ground contact loading.

2.4 Conclusion

Robotic tails have shown potential to enhance the stability, maneuverability, and propulsion of mobile robots by providing a means, separate from its main form of locomotion, to enable inertial adjustment capabilities and have demonstrated significant technological advances to the field robotics in general with recent applications demonstrating manipulation. Despite the achievements accomplished with robotic tails, based on the current state-of-the-art, significant challenges still persist in regards to mechanical design, modeling and control to provide a full range of capabilities based on tail usage observed in nature, and fully understand the effects of both inertial forces and moments and its impact on the mobile robot.

26

CHAPTER 3: ARTICULATED ROBOTIC TAIL DESIGNS

The literature review presented in the previous chapter delineated the state-of-the-art contributions to the field robotic tail design and implementation for inertial adjustment applications, and helped synthesize a comparison to highlight the differences between existing literatures. Previous methods have utilized planar or spatial rigid body pendulum-like tails, and continuum tails. This chapter aims to bridge the gap between existing methods of robotic tail implementation that utilize pendulum-like and continuum manipulators for inertial adjustment applications by proposing the use of articulated spatial robotic tails constructed of rigid-links that are interconnected via revolute joints.

Recent research by Rone and Ben-Tzvi studied the effect of tail structures, ranging from a single body rigid pendulum to a 6-DOF articulated tail, on the maneuverability of legged robots along the yaw direction [15]. A dynamic model was developed that calculated the tail base loading (inertial moments and forces) based on prescribed joint angle trajectories. Simulation based case studies were presented that analyze the effect of tail motion on yaw angle maneuverability, and the impact of increased tail articulation for equivalent angle trajectories. Results indicate that higher articulation in the tail structure results in larger angular displacements that correspond to larger velocities and accelerations of the tail segments that increase inertial loading in comparison to single body rigid pendulums undergoing equivalent tail motions. For similar tail trajectories, a 6-DOF tail provided a greater net yaw angle rotation of a quadruped robot equivalent to 33.8° in comparison to a single DOF tail that provided a yaw angle rotation of 25.5°. However, increased articulation requires more complex mechanical designs and control of the additional DOFs. Therefore, mechanical designs of existing under-actuated articulated robotic structures should be investigated to feasibly construct articulated tail mechanisms that can be implemented on robotic tail for the simplest design and control complexity.

In this chapter, Section 3.1 reviews previous articulated robot manipulator structures to: 1) identify design challenges, and 2) highlight useful design criteria for articulated tail implementation. From this review, a set of required design criteria are discussed in Section 3.2 to

address the challenges of design, actuation, and control of articulated robotic structures. From these design requirements, two novel articulated spatial robotic tail designs are proposed in sections 3.3 and 3.4 that will be used for inertial adjustment applications onboard a quadruped and biped legged robot as will be further discussed and analyzed in subsequent chapters.

3.1 Existing Under-actuated Articulated Robotic Structures

The term under-actuation is used to describe a robotic system having fewer actuators than DOFs [64]. Examples from nature indicate that not all DOFs need to be independently actuated; for instance the human hand is estimated to have 21-DOF and is actuated with 16 muscle pairs via a complex tendon system located in the forearm [65]. This section discusses the two main design approaches that dominate the field of under-actuated articulated robotics: Continuum and Serpentine.

Continuum robots are defined by their ability to continuously bend along their length [66]. Extrinsically actuated continuum robots are composed of an actuation unit at the base, an actuation transmission system (typically cables or rods [59, 67]), and a manipulator composed of an elastic backbone that provides structural support and elastically distributes angular deflection along its length. Intrinsically actuated designs integrate actuation along the robot and generate motion from the expansion and contraction of parallel structures. The utilization of a compliant core and extrinsic actuation provides the benefits of using common forms of actuation (often rotary motors), that are placed away from the point of application that enables robotic manipulator miniaturization and relatively higher flexibility at the cost of lower response time and degraded accuracy [56].

Although continuum structures are capable of forming spatial curvatures, there remain significant challenges in terms of modeling these structures, sensing their configuration and performing real-time motion planning and control due to the absence of conventional joints, which are all active research topics [57, 68]. Previous implementation of continuum robots for a robotic and challenges associated with this task have been described in Chapter 2 [13].

Serpentine robots are characterized by their ability to form discrete curvatures and are composed of a serial chain of numerous rigid links connected by joints [66]. Traditional serpentine robots are fully actuated with motors and encoders at each joint. However, individual joint actuation increases the robot's mass, cross-section, and actuator torque requirements. Another approach separates the manipulator structure from the actuators and produces motion with a cable

transmission system, similar to extrinsically actuated continuum robots. In these designs, elastic components were utilized to regulate joint rotation [69-71]. However, this approach requires individual cable actuation since cable displacements are not typically constrained to be equal during motions. Alternatively, rolling contact joints with specially designed contours have been proposed to maintain equal antagonistic cable displacements and address the issue of limited joint rotation due to elastic joint angle regulation and enable the connection of two active cables to a single driving pulley which reduces the number of required actuators [72]. A method of decoupling multi-segment curvature actuation utilizing a hollow elastic backbone to route cables along the neutral axis has been proposed by [71]. Highly flexible, variable stiffness, cable driven manipulators composed of a serial connection of jammable segments contained within vacuumed membranes of granular material have also demonstrated spatial multi-segment motions [60, 73].

The merits of extrinsic actuation in serpentine-like robotics have been widely demonstrated in robotic hand/finger and gripper designs that commonly have more joints than actuators to reduce manipulator size and inertia [74]. Fixed motion coupling is one method of distributing angle via gear trains [75], closed belts/pulleys [76], and linkages [77] that provide structural rigidity and accurate trajectory tracking. Cable transmission systems have also been used to produce motion in combination with angle distribution methods such as friction pulleys [78], higher order rolling pairs [79], and spring-loaded joints [80].

3.2 Design Motivation and Requirements

As a precursor to presenting the detailed design concept, three primary requirements driving the tail's design are presented. First, the tail should be spatial and significantly multi-functional, capable of affecting the mobile robot both dynamically and quasi-statically. Quasi-static loading reconfigures the tail to accurately adjust the net system COM positioning. Dynamic loading utilizes rapid tail motions to generate high-magnitude inertial loading to impact the system dynamics. A spatial tail will enable loading in the yaw, pitch and roll directions. While the tail structure will not be able to apply an arbitrary loading profile with forces decoupled from moments, it should be capable of generating significant moments about all directions.

Second, similar to tails in nature, the mechanism should be articulated and capable of forming multiple curvatures. As discussed in [15, 51], the use of an articulated structure allows for magnified acceleration of a tip mass due to the addition of the angular accelerations along the tail.

Based on section 3.1, a serpentine-like structure is chosen to provide additional articulation due the conventional means of design, modeling, and sensing. Extrinsic actuation transmitted by cabling is chosen to reduce manipulator size, inertia and actuator loads. However, the mechanical structure and cable routing scheme determines the system's required number of active DOFs for controlled motions. For example, Fig. 3.1(A) shows a single link with a revolute joint located at its base that is actuated using a straight cable routing scheme – as utilized in [81]. Left and right cable displacements (Δ_L and Δ_R, respectively) are calculated using Eq. 3.1, where r_{cbl} is the effective radius/length of the link, and $\{h, w, \alpha\}$ are the geometric link parameters shown in Fig. 3.1(A). Since antagonistic cable displacements are not equal in magnitude for a given link rotation β_i, each cable requires an independent actuator and control scheme to produce rotation.

$$\Delta_L = \sqrt{h^2 + w^2 - 2hw\cos(\alpha - \beta)} - r_{cbl},$$
$$\Delta_R = \sqrt{h^2 + w^2 - 2hw\cos(\alpha + \beta)} - r_{cbl} \tag{3.1}$$

Figure 3.1(B) shows a straight cable routing method employed by manipulators that utilize an elastic core for angle regulation. Due to material isotropy, it can be assumed that bending is uniform [69-71]. Therefore, the mechanism can be modeled as two links rotating about a centered revolute joint. The associated Δ_L and Δ_R are defined in Eq. 3.2 with the geometric parameters, defined in Fig. 3.1(B). For small rotations antagonistic cable displacement can be assumed to be equal and opposite and can be attached to a single driving pulley; thus, reducing the overall size, weight and control complexity of the cable driven mechanism [70]. However, for large deflections each cable requires an actuator and synchronous control that may increase the size and complexity of the system [69, 71].

$$\Delta_L = -2w\sin(\beta/2) - 2r_{cbl}\sin^2(\beta/4),$$
$$\Delta_R = 2w\sin(\beta/2) - 2r_{cbl}\sin^2(\beta/4) \tag{3.2}$$

To address these challenges, the proposed designs will investigate the effectiveness of grooved, cylindrical contoured links that act as pulleys to route cables and maintain equal cable displacements with minimal slack during operation. The cylindrical routing scheme, shown in Fig.

30

3.1(C), results in the equal but opposite left and right cable displacements defined in Eq. 3.3 using the r_{cbl} geometric parameter defined in Fig. 3.1(C). Therefore, if the antagonistic cables are initially tensioned and connected to a pulley, the cylindrical routing method can ensure no cable slack during rotation of the pulley. This design feature enables antagonistic cables from multiple links to be attached to a single multi-diameter pulley that can be actuated using a single motor, thus reducing the number of actuators required to achieve tail curvatures.

$$\Delta_L = r_{cbl}\beta$$
$$\Delta_R = -r_{cbl}\beta \qquad\qquad (3.3)$$
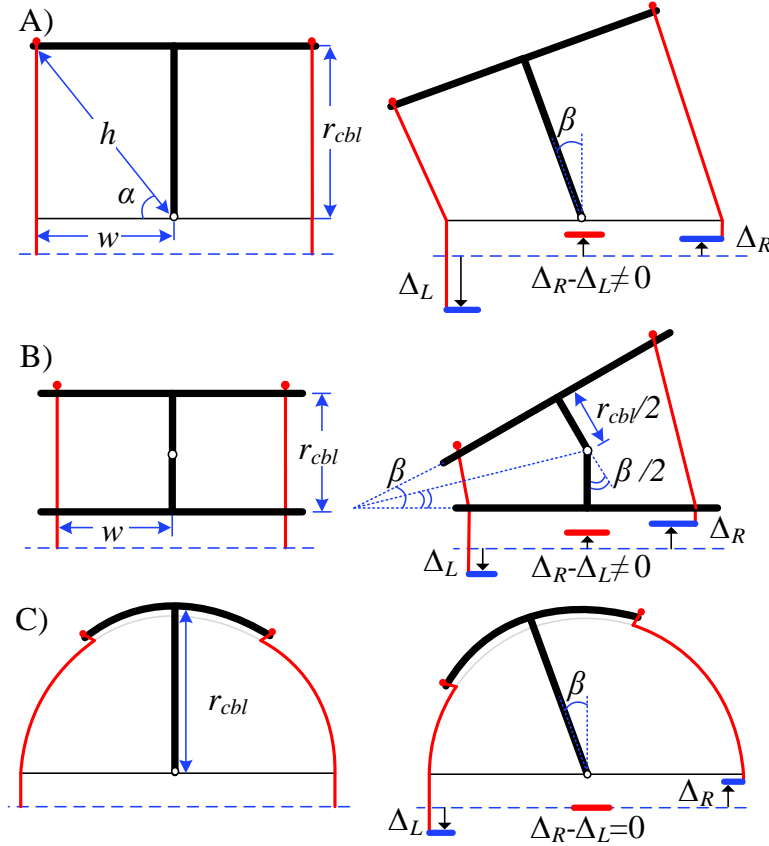
Figure 3.1: Various mechanical structure and cable routing approaches: A) Base located revolute joint with straight cable routing, B) Uniform bending of a centered revolute joint with straight cable routing, C) cylindrical cable routing.

3.3 Roll-Revolute-Revolute Tail Design

This section details the mechanical design of the R3-RT [14], where the design specifications from section 3.2 are implemented in the proposed mechanism intended for use onboard a quadruped robot, attached in cantilevered mode. This tail incorporates a long articulated structure and high-power motors to generate inertial loading sufficient enough to stabilize and maneuver a quadruped as will be demonstrated in Chapters 5 and 8.

The R3-RT (Fig. 3.2) is composed of three main subsystems: the rigid housing, actuation unit, and tail segments. The rigid housing, shown in Fig. 3.3, consists of front and rear frames connected using steel rods and provides a relatively lightweight, rigid support for the tail that can be attached to a mobile robot via its connector ports. Bearings in each frame support the actuation unit's roll DOF, and an internal gear is integrated in the rear frame. A spur gear, attached to a motor in the actuation unit (Fig. 3.4), meshes with this internal gear to actuate the roll-DOF rotation; this roll is measured with an absolute encoder mounted to the rear frame and coupled to the actuation unit at a groove in the hollow shaft via a timing belt (Fig. 3.4). A high-current-capacity, miniature slip ring (Orbex 300 Series) is also integrated in the rear frame to provide command signals and motor current to the actuation unit. This slip ring enables continuous roll rotation of the tail along the z_T axis (Fig. 3.2), allowing it to operate without the risk of breaking wires. This feature enables the R3-RT to act like a reaction wheel that can rotate unconstrained about the roll axis and provide pure reactive moments to a mobile robot to aid stabilization or maneuverability in addition to acting as a conventional asymmetrical robotic tail inertial adjustment mechanism. This provides significant advantages over prior tail designs (Table 2.1) that have constrained workspaces.
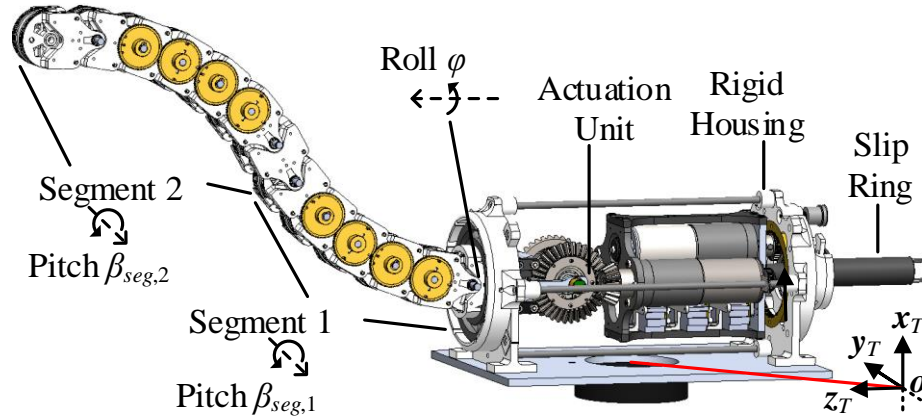
Figure 3.2: R3-RT overall system design.
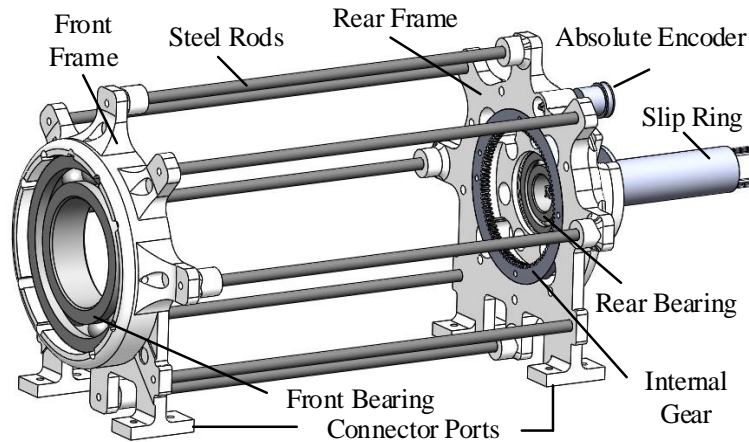
Figure 3.3: R3-RT rigid housing.

The actuation unit, shown in Fig. 3.4, houses the tail actuation, motor speed and cable pulley position sensors, and the motor controllers. The actuation unit structure is provided by an aluminum frame that sits in the pair of roll-DOF bearings mounted within the rigid housing.

The tail actuation consists of three gear motors: one to actuate the roll-DOF, and two to actuate the tail segment DOFs. The roll-DOF motor is attached to a spur gear that meshes with an internal gear located in the rigid housing. The segment gear motors are coupled to the two-channel pulley through a pinion/bevel gear reduction (Fig. 3.4). The pulleys are rigidly connected to both the bevel gear and the antagonistic cable pair used to actuate the motor's tail segment.

Four adjustable tensioning mechanisms (Fig. 3.4) provide a means of individually tensioning each of the four cables (two antagonistic cables per actuated segment) to ensure a straight home configuration and minimize backlash. These tensioners are composed of a lever arm

33

(to adjust the cable path) and passive roller (to minimize cable friction during motion). The tensioners are connected to the segment plate, to which the base link of the tail is also connected.

A microcontroller and three motor drivers are nested below the motors, with electrical cabling routed through the hollow shaft to the power control module via the slip ring.
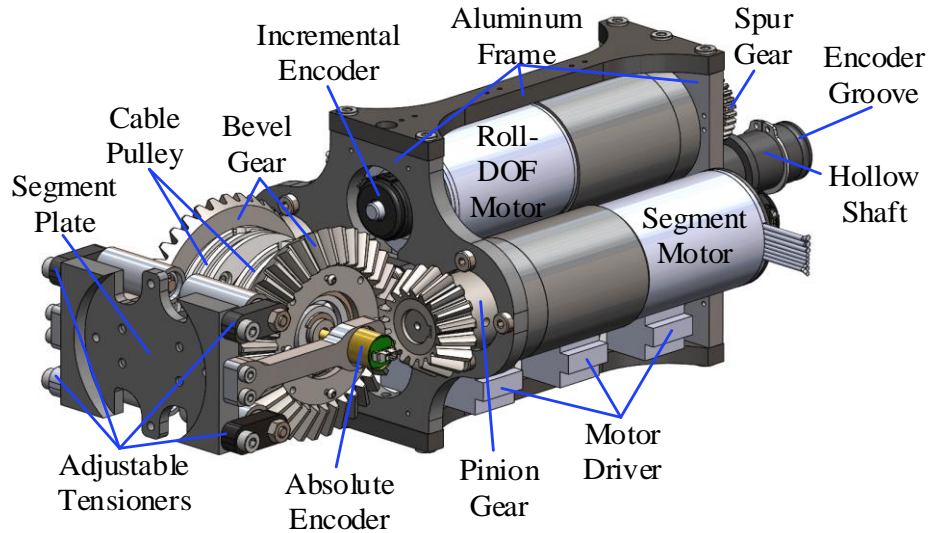
Figure 3.4: R3-RT actuation module.

Figure 3.2 shows the overall tail design concept. Twelve bodies (links 1-12) are connected serially to create a two-segment robotic tail capable of "bending" in a rotating plane. Link 1 is connected to the actuation unit at the segment plate (Fig. 3.4) through link 0 by a revolute joint in the pitch direction when roll angle of the actuation unit is zero.

The remaining 11 links are connected by revolute joints parallel to the joint between links 0 and 1. As a consequence of this design, when the roll angle is ±90°, the tail remains extended without requiring cable actuation. Distinct segments are created by terminating pairs of antagonistic cables along the robot—in Fig. 3.5, two segments are created by terminating cables at link 6 and at link 12.

The R3-RT addresses the challenges of decoupled multi-curvature actuation and equal antagonistic cable displacements through its link design and cable routing scheme. Cables are routed along nested cylindrical surfaces built into the links to ensure equal cable extension/retraction of the antagonistic cable pair during tail motion. Figure 3.5(A) shows the cable paths for segment 1, in which the cable pairs route along six cylindrical surfaces before terminating

(tying off) at link 6. The segment 1 antagonistic cable displacements are defined by the linear relationship $\pm 6 r_{cbl}\beta_i$, where r_{cbl} is the radius of the cylindrical contour and β_i is the relative link rotation. The nested cylinder cable routing approach enables the use of a single pulley to simultaneously control the extension and retraction of an antagonistic cable pair without the need for an additional mechanism to account for variance in extension and retraction. This is because the angular displacement of the joints increases and decreases the cable path by equal angles on each side over the same radial dimension.

As an additional requirement to simplify control, considerations were also made to mechanically decouple the actuation of segments 1 and 2. Figure 3.5(B) shows the cable paths for segment 2. Within segment 2 (links 7-12), the cable routing is similar to the segment 1 cables in links 1-6 in Fig. 3.5(A). However, through links 1-6, the segment 2 cabling routes along an S-path and crosses the R3-RT between links 2 and 3. With this S-path routing, the cable path on the link 0-2 cylindrical surfaces and the link 3-5 cylindrical surfaces will extend and shorten the cable path by equal amounts, or vice versa. This routing creates a null space for the segment 2 cable displacements with respect to the segment 1 motion. However, this assumes that the joint angles along the segment are equal.
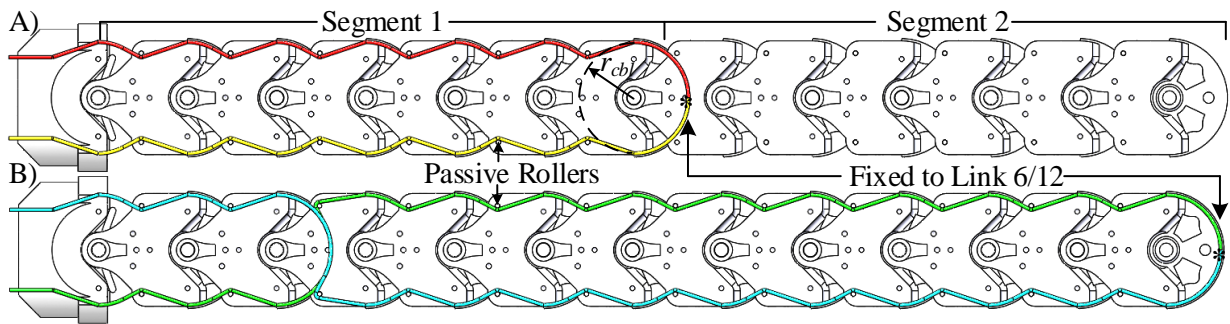
Figure 3.5: R3-RT cabling concepts: A) segment bending arrangement, and B) S-path arrangement.

To ensure a segment's 6 joint angles are equal, the R3-RT utilizes 5 gear pairs mounted along the segment. The gears in each pair are mounted on two links with a single link separating them, as shown in Fig. 3.6(A). For example, in gear pair 1, the first gear (red) meshes with the second gear (purple) with an intermediate link (yellow) separating the gears' associated rigid bodies.

To ensure equal angles along the segment, the gears in each pair have equal pitch diameters. For the gear pair associated with three sequential links i-1, i and i+1, shown in Fig. 3.6(B), gears are rigidly attached to links i-1 and i+1, with link i separating the links. If link i-1 is held fixed, link i will rotate by angle β_i relative to link i-1, and link i+1 will rotate by β_i relative to link i. This is done for the five sequential triplets of links 0-6 (segment 1) and 6-12 (segment 2).

Although gears were used here in the R3-RT as a straightforward means to implement the coupling between links, other means of rigidly coupling the links' rotations using linkages may also be considered in future work, such as a scissor mechanism or a crossed four-bar.

These features integrated into the R3-RT mechanism present a novel approach to achieve decoupled actuation of multi-curvature cable driven serpentine-like manipulators as reviewed in section 3.1. The effectiveness of this approach is experimentally evaluated in Chapter 4.
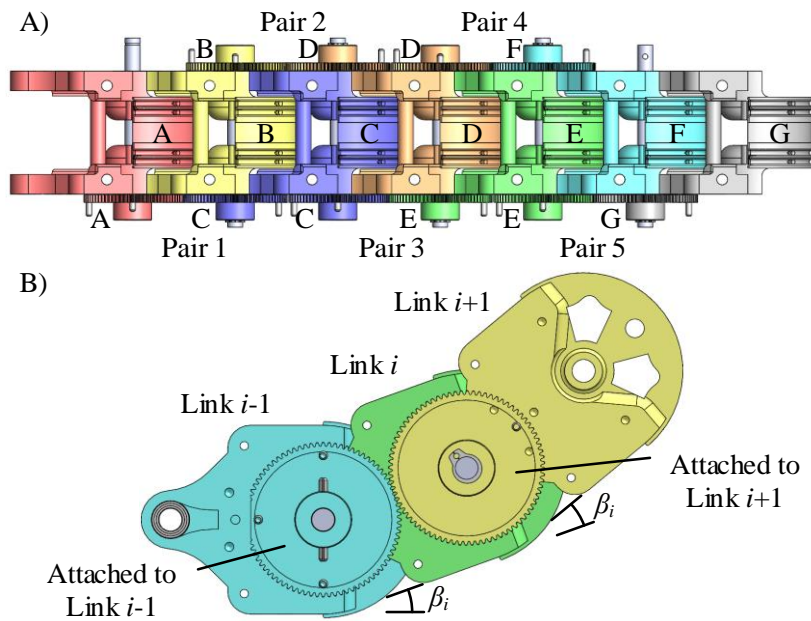
Figure 3.6: R3-RT gearing: A) single-segment gear arrangement, and B) angle constraint from gear pair. Parts sharing a color are rigidly attached.

3.3.1 Sensing, Actuation and Electrical Design

This section details the electromechanical considerations for the R3-RT, including the types of sensors, considerations for actuation, and the overall electrical design of the system.

Two types of joint-space sensing are integrated into the actuation module of the R3-RT: angular position (roll or cable pulleys) and motor rotor speed. The three position measurements

are generated by absolute encoders (US Digital MA3) coupled to the hollow shaft (roll DOF) or cable pulleys (segment DOFs). The roll-DOF encoder fits into the mount designated in Fig. 3.3 and is coupled to the actuation module using a timing belt mounted to the groove shown in Fig. 3.4. The two segment-DOF encoders are shown coupled to the cable pulley in Fig. 3.4 through the bevel gear. To measure motor rotor angular velocity, three incremental encoders (US Digital E4T) are mounted to the motor.

To generate high inertial loading, the R3-RT is actuated using three Maxon 100 W brushless DC motors (ECi 40) in closed-loop position control. These motors were chosen to exceed the requirements for experiments presented in this analysis to provide an experimental test platform capable of analyzing a wide variety of potential tail structures or various dimensions and mass properties. Gear reductions were selected to balance considerations for cable speed and force requirements estimated for a range of possible robotic tails.

Two of the three motors control the independent bending of the R3-RT segments through antagonistically-actuated cable mechanisms. A bevel gear train with 2:1 reduction drives the cable pulley, and a gearbox with reduction 51:1 is used to drive the pinion gear. The pulley radius matches the cylindrical cable routing radius r_{cbl} of the linkages, which results in a one-to-one ratio between the pulley rotation and segment bending angle (e.g., if the segment 1 pulley rotates 45°, segment 1 will bend 45°).

The third motor controls the R3-RT actuation module roll-angle using a spur gear coupled to an internal gear (with a gear reduction of 3:1 in addition to a 51:1 gearbox). Incorporating the roll motor within the actuation unit reduces the cross-section, as opposed to locating it externally, at the cost of increased power required to produce roll motion due to the additional inertia. However, in this design, the motors are not located far from the center of rotation, thereby minimizing their mass contributions to the net inertia of the system.

Figure 3.7 shows the electrical design of the R3-RT. To control the system, two Teensy 3.2 ARM microcontrollers (MCUs) are used in a master-slave configuration. These MCUs communicate over an UART link through the slip ring. The master MCU is mounted to the rigid housing and connects the user PC and the slave MCU. The master MCU receives the three desired joint angle trajectories from the user, interpolates this data into position set points and sends these set points to the slave MCU. The master MCU also allows the user to exercise software control

37

over motor power through a high side MOSFET switch. The master MCU housing also connects the power supply to the slip ring through an emergency cut-off switch.

The slave MCU is incorporated into the actuation module to ensure stable connections with the sensors and motor drivers. The slave MCU is programmed as a PD controller to control the three motors in closed-loop position control mode. The slave MCU obtains the three angles from the absolute encoders and commands the motor speeds to the motor drivers, with the proportional gain equal to 230 s^{-1} and the differential gain equal to 28.6. The controller gain coefficients were tuned for near-critical operation on the bases of empirical analysis. The position control loop operated at a control frequency of 450 Hz.

Each motor is controlled by a motor driver (Maxon ESCON 50/5) operating a PI velocity control loop. These motor drivers receive velocity commands from the slave MCU and regulate current to the motors using a proportional gain of 450 N-m-s/rad and an integral gain of 2.0 N-m/rad.
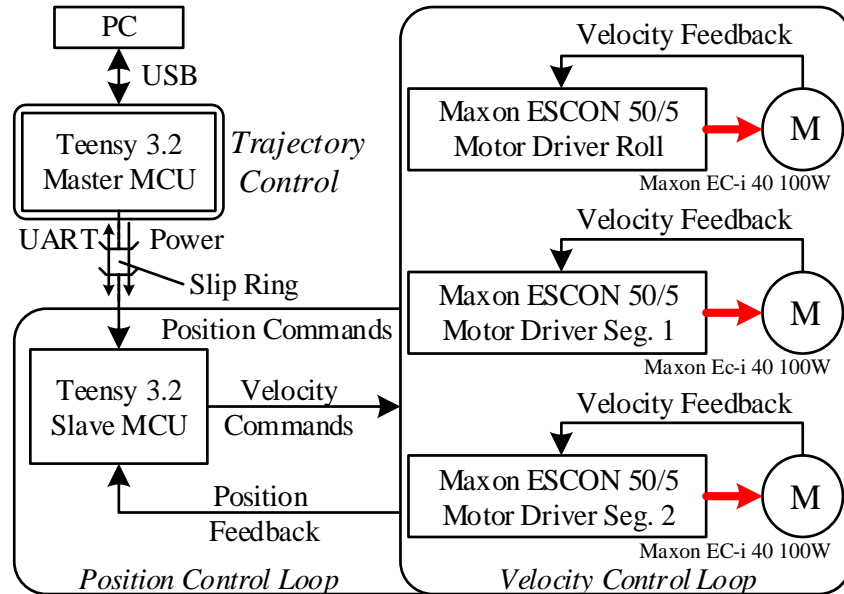
Figure 3.7: R3-RT electrical design with inner-loop velocity control and outer-loop.

3.4 Discrete Modular Serpentine Tail Design

This section presents the mechanical design of the DMST [16, 17], where the design specifications from section 3.2 are implemented in the proposed mechanism. As opposed to the R3-RT intended for use on a quadruped robot, presented in the previous section, the DMST is designed with a

smaller footprint and utilizes lower power motors since it is intended for inertial adjustment of a lighter weight biped robot attached in a vertical configuration, as demonstrated in Chapter 5 and 8.

Figure 3.8 presents a simplified schematic diagram of the proposed mechanism showing the actuation unit and two tail links. The tail structure is composed of a series of links connected to one another using parallel revolute joints and to ground through a revolute joint that is perpendicular to the other joints. The mechanism is capable of controlling two-DOF: 1) roll about the ground y-axis that changes the orientation of the bending plane to distribute loading, and 2) tail bending in the actuation unit XY plane that varies the tail COM location and generates loading profiles via high-speed tail motions. The roll-DOF ϕ is actuated directly using a high-torque servomotor, and the bending-DOF is actuated using a cable transmission system driven by a high torque servo motor that rotates a multi-diameter pulley (MDP) by an angle ϑ_m. The motors and MDP are located within the actuation unit that serves as a protective, rigid housing for electrical components and distributes routed cables to their respective pulley diameters.
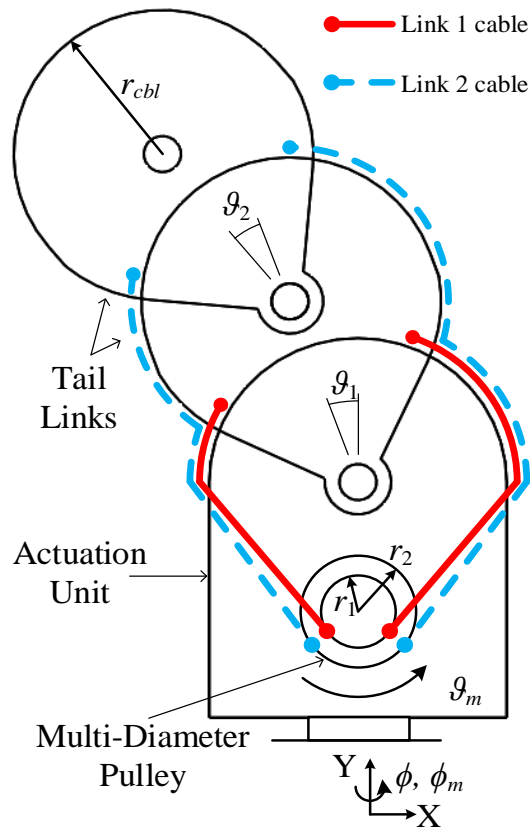
Figure 3.8: Simplified schematic diagram and kinematic model of a two-link DMST.

39

As shown in Fig. 3.8, each link is connected to the MDP using an antagonistic pair of low-friction, nylon coated steel braided cables with swaged ball bearings to secure the cable ends. The cables terminating at each link route through mid-links that separate the link at which the cables terminate and the actuation unit. A mid-link, such as link 1 in Fig. 3.8, is a link that has two or more cables routed through it that do not terminate at that particular link. Mid-links have a grooved, cylindrical surface that is used for cable routing to maintain equal cable displacements as the MDP is rotated as discussed in section 3.2.

Figure 3.9(A) shows the detailed mechanical design of a 3-link DMST. Tail links are designed to be lightweight, rigid structures capable of tolerating high loads produced by cable tension. The MDP consists of n grooved channels used for routing and terminating cables that control the positioning of n links. The maximum number of links the DMST structure can accommodate is dependent on geometric constraints required for the MDP grooved channel widths. Furthermore, additional links requires more routed cables that increase friction in the structure a concept that will be modeled and evaluated in Chapter 5. Varying the pulley diameter for each cable channel varies the net bending of the link at which that cable terminates; as a result, the desired tail bending motion can be achieved through the rotation of a single DOF. Previous work has presented an optimization procedure to compute mechanism dimensions to achieve a desired set of best fit tail curvatures [16].

A pair of tensioning systems are built into the two sides of each tail link (Fig. 3.9(B)). These are used to tension routed antagonistic cables to maintain a straight home configuration, keep cables routed along their cylindrical contours, and minimize backlash during operation. The tensioner consists of a sliding unit that is capable of translating within a slot using a screw and nut mechanism. Tightening the screw translates the sliding unit inward. With sufficient translation, the sliding unit engages and tensions the routed cables, which causes an angular adjustment of the link. Cable tensioning is performed on both sides of each link to align its orientation. The tensioning procedure is initiated at the lowest link and ends at the n-th link since the rotation of links nearer the base affect the orientation downstream due to the serial structure.

A flat link is placed at the end of the tail to serially connect DMST units. For example, Fig. 3.9(C) shows a robotic tail concept consisting of two 5-link DMSTs connected in series forming planar S- and U-shaped tail curvatures (also defined as mode-shape 1&2, the benefits of mode-

40

shapes for providing planer end effector and COM workspaces will be demonstrated in Chapter 4). If the tail is performing manipulation tasks, modular end effectors such as a robotic gripper can be attached to the end link to improve the tail's functionality. Spatial configurations can be achieved using the roll DOFs. The concept of modularity to enhance manipulation through the serial connection of DMSTs presents the authors' future envisionment of this mechanism to move beyond the paradigm in which a robotic tail is used for one function on board a mobile robot.
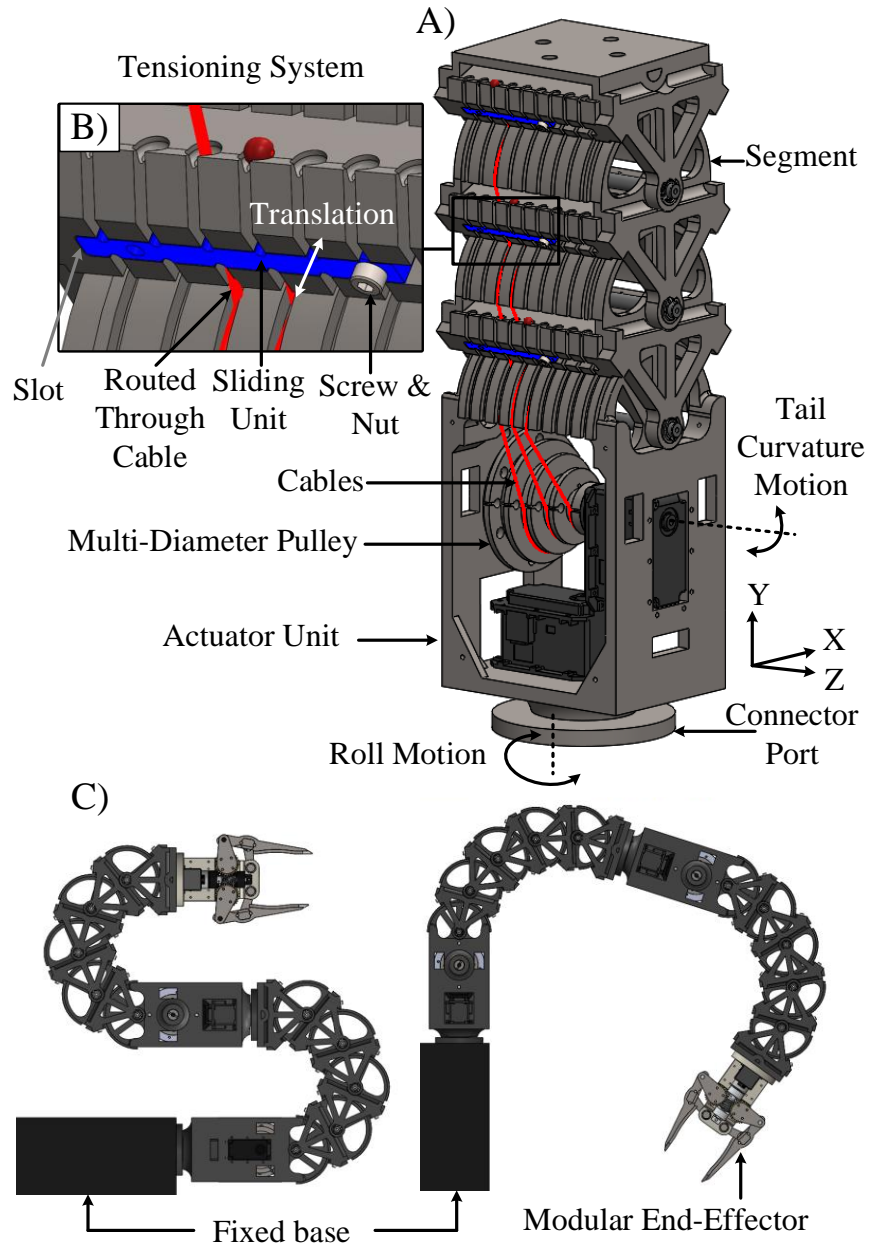
Figure 3.9: A) Mechanical design of a 3-link DMST, and B) Close up view of a mid-link and tensioning system, and C) Planar S- and U-shaped curvatures of two five-link DMSTs connected in series.

3.5 Summary and Outtake

Although pendulum-like and continuum tails have been previously used for inertial adjustment applications, recent simulation results presented by Rone and Ben-Tzvi [15] have demonstrated that articulated tail structures produce enhanced inertial loading for yaw angle rotation of a

quadruped robot in comparison to rigid-body pendulum-like tail mechanisms. However, articulated structures pose new challenges for the design and control of additional DOFs.

A thorough review of serpentine and continuum robots was performed to identify a set of useful design criteria to effectively design articulated spatial robotic tails. In addition, based on the literature review presented in Chapter 2, two design requirements were imposed to mimic the functionalities of tail usage found in nature. First the proposed tails should be capable of affecting the legged robot both dynamically and quasi-statically. Quasi-static loading reconfigures the tail to accurately adjust the net system COM positioning. Dynamic loading utilizes rapid tail motions to generate high-magnitude inertial loading to impact the system dynamics. A spatial tail will enable loading in the yaw, pitch, and roll directions. While the tail structure will not be able to apply an arbitrary loading profile with forces decoupled from moments, it should be capable of generating significant moments about all directions. Second, the mechanism should be articulated and capable of forming multiple curvatures. The use of an articulated structure allows for magnified acceleration of a tip mass due to the addition of the angular accelerations along the tail for enhanced loading capabilities [15, 51] and multiple curvatures enables a greater manifold for COM positioning.

Based on these requirements, a serpentine structure with a cable transmission system using extrinsic actuation was chosen for implementing two novel articulated spatial robotic tail mechanisms, each intended to be attached onboard either a quadruped or biped robot to enhance the legged robots stabilization and maneuverability.

The R3-RT is a 3-DOF serpentine tail structure (2 articulated tail curvatures, and 1 roll motion) mechanism, intended for use on a quadruped robot, which is composed of rigid links interconnected via revolute joints. Cable routing about circular contoured links and an S-shape cable routing scheme maintains equal antagonistic cable displacements and enables two mechanically decoupled tail curvatures. A spur gear train is used to regulate equal relative link rotations and kinematically resolve the redundancy within the two tail segments. A slip ring incorporated into the roll-DOF enables infinite rotation without the risk of breaking wires and allows the tail to act like a reaction wheel by imparting long duration, unconstrained reactive moments about the roll-axis.

The DMST is a 2-DOF serpentine tail structure (1 articulated tail curvature, and 1 roll motion), intended for use on a biped robot, that utilizes a cable transmission system routed about

circular contoured rigid links to enable equal antagonistic cable displacements. Therefore, the antagonistic cables can be connected to single active multi-diameter pulley that, upon rotation, creates a controlled articulated tail curvature. Each module is self-contained, a feature that enables infinite rotation about the roll-axis for reaction wheel like operation and the modular connection of multiple tail modules in series to achieve independently actuated multi-tail curvatures (configuration shapes).

The corresponding dynamic models and experimental evaluation for each tail are presented in the Chapters 4 and 5.

CHAPTER 4: MODELING, ANALYSIS, AND EXPERIMENTATION OF R3-RT

Chapter 3 presented the detailed design of the R3-RT tail mechanism that is intended for use onboard a quadruped robot, connected in cantilevered mode, that can create sufficient inertial loading to stabilize and maneuver a large robot due to its long articulated tail structure and high-power motors. This section presents the kinematic and dynamic model of the R3-RT (section 4.1) accounting for the system's rigid-coupling between linkages and the cable-driven actuation. These models are used to analyze the workspace and impact of tail motion and tail configuration on the loading profiles, generated forces and moments due to tail motions, transferred through the tail base that will eventually be applied to the legged robot for inertial adjustment applications (section 4.2). Then, experiments using integrated prototypes are performed (section 4.3) to validate the forward kinematic and dynamic models, determine the mechanism's accuracy and repeatability, and measure the mechanism's ability to generate inertial loading (an important feature for accurate experimental validation of developed control schemes presented in Chapter 8). The significant results of this chapter demonstrate that the R3-RT mechanism exhibits an enhanced workspace and inertial loading capabilities relative to conventional pendulum-like tail structures.

4.1 Roll-Revolute-Revolute Tail Model Overview

The tail model has three inputs—two prescribed cable displacements δ_k caused by pulley rotation $\beta_{seg,k}$ driving each segment for $k \in \{1,2\}$, and a prescribed roll rotation φ. Due to kinematic constraints of the gear train system, let β_k represent relative link rotations within a segment (Fig. 4.1). There are two cable tensions T_k, caused by pulley rotation, and a roll-DOF torque τ driving the system.

In the R3-RT, there are a total of 13 revolute joints that create spatial tail configurations. If the net moment $M_{i,jnt}$ is calculated at joint i, the dot product of $M_{i,jnt}$ and the joint i axis unit vector ς_i equals zero, due to the joint's inability to support a moment about its joint axis. This is defined in Eq. 4.1, where R_i is the link i orientation matrix, and y and z are the y- and z-axis unit vectors. Four loading effects will contribute to $M_{i,jnt}$: gravity ($M_{i,grv}$), inertia ($M_{i,inr}$), gear meshing

($M_{i,gear}$), and actuation ($M_{i,act}$), as shown in Eq. 4.2. Derivation of these loading effects and their mathematical formulations are detailed in [14].

$$\varsigma_i \cdot \mathbf{M}_{i,jnt} = 0, \quad \varsigma_i = \begin{cases} R_i \mathbf{z}, & i = 0 \\ R_i \mathbf{y}, & i > 1 \end{cases} \tag{4.1}$$

$$\mathbf{M}_{i,jnt} = \mathbf{M}_{i,inr} - \mathbf{M}_{i,grv} - \mathbf{M}_{i,gear} - \mathbf{M}_{i,act} \tag{4.2}$$

4.1.1 Kinematic Model

First, the tail kinematics are defined. Due to the R3-RT's cable geometry and gearing, there is a fixed relationship between δ_k, and $\beta_{seg,k}$, defined in Eq. 4.3, where r_{cbl} is the cable routing cylinder radius (Fig. 4.1). Using these variables, the pitch joint angles ϑ_i of tail linkages may be defined using Eq. 4.3. R_i is defined using Eq. 4.4, where $R_Z(\varphi)$ and $R_Y(\vartheta_i)$ denote z- and y-axis rotations by angles φ and ϑ_i, respectively (with reference to the coordinate frame shown in Fig. 4.2).

$$\beta_k = \delta_k / (6r_{cbl}), \quad \delta_k = r_{cbl}\beta_{seg,k}, \quad \vartheta_i = \begin{cases} \beta_1, & 1 \leq i \leq 6 \\ \beta_2, & 7 \leq i \leq 12 \end{cases} \tag{4.3}$$

$$R_i = \begin{cases} R_Z(\varphi) & i = 0 \\ R_{i-1}R_Y(\vartheta_i) & i > 0 \end{cases} \tag{4.4}$$

With reference to Fig. 4.2, using R_i, the joint positions $p_{i,jnt}$ and link COM positions $p_{i,COM}$ may be calculated using Eqs. 4.5 and 4.6, where $p_{0,jnt,lcl}$ is the position from the frame T origin to joint 0, $p_{1,jnt,lcl}$ is the position from joint 0 (roll-DOF) to joint 1, L_{J2J} is the distance between two adjacent joints, $p_{0,COM,lcl}$ is the position from joint 1 to the link 0 COM and L_{J2C} is the distance between a joint and its COM (Fig. 4.1). In addition, $p_{i,j,J2C}$ in Eq. 4.7 defines the position from joint i to the link j COM.

46

$$p_{i,jnt} = \begin{cases} p_{0,jnt,lcl} & i = 0 \\ p_{i-1,jnt} + R_{i-1}p_{1,jnt,lcl} & i = 1 \\ p_{i-1,jnt} + L_{J2J}R_{i-1}z & i > 1 \end{cases} \tag{4.5}$$

$$p_{i,COM} = \begin{cases} p_{i,jnt} + R_i p_{0,COM,lcl} & i = 0 \\ p_{i,jnt} + L_{J2C}R_i z & i > 0 \end{cases} \tag{4.6}$$

$$p_{i,j,J2C} = p_{j,COM} - p_{i,jnt} \tag{4.7}$$
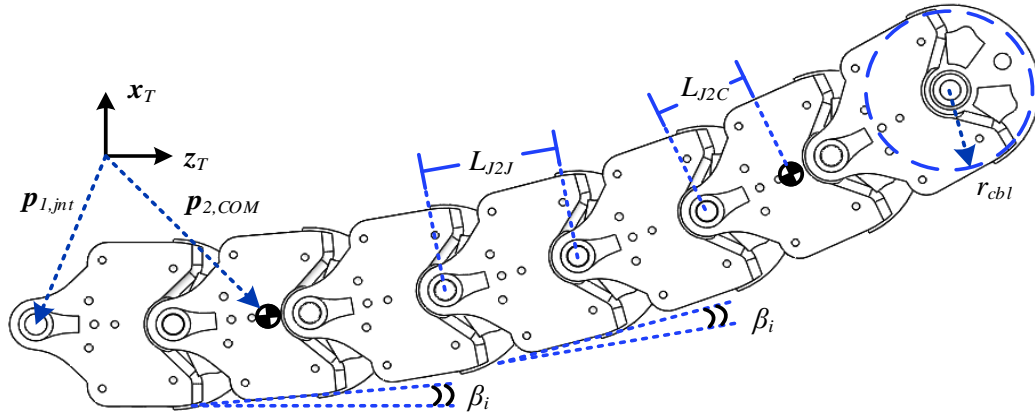
Figure 4.1: R3-RT kinematic variables in a single segment.

4.1.2 Dynamic Model

Substituting the moment loading expressions about each joint due to inertia, gravity, actuation, and gear forces into in Eq. 4.2 and evaluating Eq. 4.1 results in a set of 13 differential-algebraic equations defined by 3 state variables given by $q = [\varphi, \beta_{seg,1}, \beta_{seg,2}]$ (Fig. 4.2). Evaluation of the moment loading terms can be found in [14]. Algebraic manipulation can be used to reduce these 13 equations into the three ordinary differential equations, defining the R3-RT manipulator dynamics equation that are simplified into the form shown in Eq. 4.8 using 10 constraint equations

originating from equal and opposite gear forces since each of the R3-RT's two segments meshes 5 gear pairs.

$$M(q)\ddot{q} + C(\dot{q},q)\dot{q} + g(q) = u \tag{4.8}$$

where $M(q)$ is the inertia matrix, $C(\dot{q},q)$ is the tail's centripetal and Coriolis loading effects, $g(q)$ is the tail's gravitational loading, and is the actuation input where $T_{1,2}$ represents cable tension $u = [\tau, T_1, T_2]$ driving segment 1 and 2 respectively. This equation will be used in Chapter 7 to derive a tail motion control law for tail trajectory tracking.

4.1.3 Dynamic Tail Loading Model

When the tail is mounted to a load cell or mobile robot, an internal force F_B and moment M_B acting on the rigid housing is generated (Fig. 4.2). These forces and moments are significant since they are then transferred to the legged robot for inertial adjustment applications. The loading F_B and M_B depends on the inertia of the tail's moving links and the gravitational forces acting on all of the tail's bodies (including the rigid housing). All of these calculations are performed with respect to tail base frame $x_T y_T z_T$ (Fig. 4.2). As the gear and actuation loading are internal (i.e., forces are generated in equal, opposite and coaxial pairs), their net effects do not contributed to F_B or M_B.

Equations 4.9 and 4.10 define F_B and M_B, where m_F is the mass of the rigid housing, $F_{F,grv}$ is the rigid housing's gravitational loading and $p_{F,COM}$ is the position of the rigid housing COM relative to the tail base frame. Where the notation $\tilde{a}b$ denotes $a \times b$.

$$F_B = -F_{F,grv} + \sum_{i=0}^{n}\left(F_{i,inr} - F_{i,grv}\right), \quad F_{F,grv} = m_F g \zeta_{grv} \tag{4.9}$$

$$M_B = -\tilde{p}_{F,COM}F_{F,grv} + \sum_{i=0}^{n}\left(M_{i,inr} + \tilde{p}_{i,COM}\left(F_{i,inr} - F_{i,grv}\right)\right) \tag{4.10}$$

Where the gravitational force due to g acting about the unit vector $\zeta_{grv} = -x_T$ (Fig. 3.2), inertial force, are given by $F_{i,grv}$ and $F_{i,inr}$, respectively acting about joint i. Evaluation of these force loading terms can be found in [14] where Fig. 4.2 illustrates these variables for selected joints and rigid bodies.
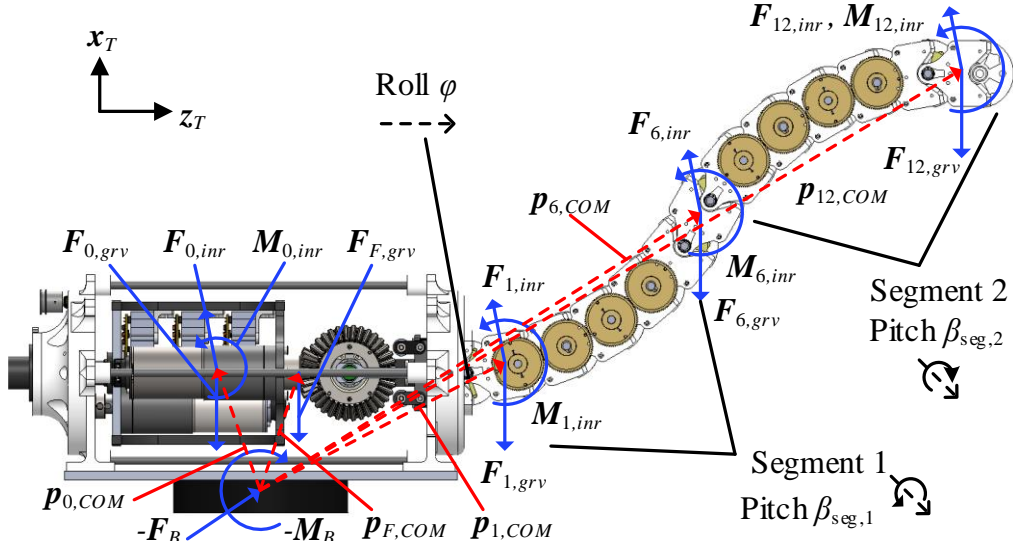
Figure 4.2: Free-body diagram of R3-RT for calculating F_B and M_B. Loading shown for links 1, 6 and 12 is representative of the loading for links 1-12.

4.2 Tail Analysis

This section analyzes the kinematic workspace (section 4.2.1) and loading capabilities of the R3-RT (section 4.2.2).

4.2.1 Kinematic Workspace Analysis

The proposed mechanism is articulated in structure and can form multi-curvature spatial tail configurations for enhanced flexibility and increased workspace. Figure 4.3 shows two configuration shapes that can be generated by the R3-RT's two segments. Configuration shape 1 is a C-shape curvature with segments rotated in the same direction. Configuration shape 2 is an S-shape curvature with the segments rotated in opposite direction.

The end effector and COM workspace are defined by the locus of positions the end effector tip (link 12) and COM can reach, respectfully. The defined workspaces can be computed using the forward kinematics (section 4.1.1) with the geometric parameters extracted from the R3-RT CAD (Fig. 4.2), defined in Table 4.1. Figure 4.3 shows the R3-RT's simulated planar workspaces (end effector and COM) with a fixed roll angle $\varphi = 0°$. The workspaces have been generated using 300×300 input combinations of the pulley angle inputs (resolution: 0.6° and 0.9° for input pulley rotation $\beta_{seg,1\text{-}2} = [-90{:}90]°$ and $\beta_{seg,1\text{-}2} = [-135{:}+135]°$, respectively). The coordinate frame origin is

the R3-RT joint 1. The ±135° spool rotation range is associated with the maximum R3-RT workspace possible without link 12 interfering with the rigid housing.

A tail's COM workspace is defined by its range of motion, mass distribution, link geometry, and number of independently actuated tail segments. For the R3-RT, the COM workspace, with no added tip-mass, is simply the end effector workspace scaled down, as shown in Fig. 4.3. In a single plane, the R3-RT has a COM workspace that spans 190°.

The reported workspace criteria presented in Table 2.1 for existing pendulum-like tails represents both the end effector and COM workspace since the mass is connected to the tip of a pendulum-like structure. However, for planar pendulum-like tails, the locus of points along which its COM can be moved is constrained along a circular arc (illustrated in Fig. 4.3); if a spatial pendulum is considered, this arc becomes a spherical surface. Compared to this, the R3-RT produces a higher dimensionality end effector workspace due to its increased articulation and has significantly greater ability to adjust its COM due to the ability to change the distance between the COM and tail base, which is important for static stabilization applications. The R3-RT end effector workspace spans 270° and exceeds the proposed workspaces of previously implemented pendulum-like tails presented in Table 2.1. However, the R3-RT COM workspace as shown in Fig. 4.3 falls 65° short with respect to [6, 40], reported in Table 2.1. This deficit can be overcome by adding a 450 g tip mass to match the 255° COM workspace and further increase the volume in which the COM can be positioned.

The benefits of two configuration shapes further increases the manifold of inertial loading about the base of the tail by actuating various configuration shapes during tail motions [51]. In applications such as disturbance rejection this feature is of importance since actuating the tail with different configuration shapes enables tail compensation for a larger variety of disturbances acting on legged robots as will be explored in Chapter 8.
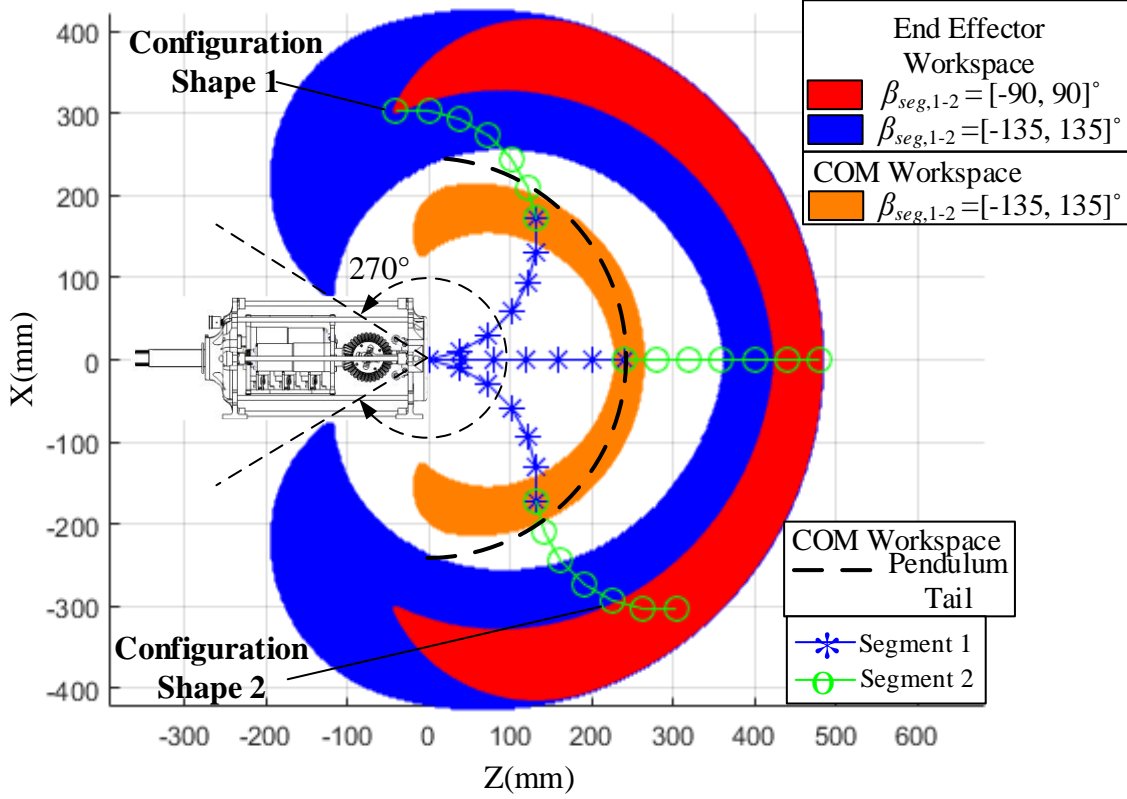
Figure 4.3: Workspace and configuration shapes of a 12 link, 2 segment R3-RT for $\varphi = 0°$.

Table 4.1: R3-RT simulation properties.

r_{cbl}	25 mm	L_{J2J}	40 mm	L_{J2C}	32.7 mm
m_0	3.144 kg	$m_{\{1\text{-}12\}}$	0.0759 kg	$p_{0,jnt,lcl}$	92.1x mm
$p_{1,jnt,lcl}$	159.24z mm	$p_{0,COM,lcl}$	$[-3.52, 0, -7.33]^T$ mm		

4.2.2 Dynamic Tail Loading Analysis

In order to utilize the R3-RT's kinematic and dynamic models to simulate the tail base loading, the parameters used to calculate F_B and M_B in Eqs. 4.9 and 4.10. Inertial and geometric properties used in this analysis, reported in [14], match that of the prototype in section 4.3, to allow comparison of the simulated and measured results.

In addition, trajectories of $\beta_{seg,k}$ and φ are required. For $\beta_{seg,k}$, trajectories of the input pulley rotation are defined using a sixth-order polynomial, where t is the simulation time, t_0 and t_f are the trajectory start and end times, $\beta_{seg,k,0}$ and $\beta_{seg,k,f}$ are the segment pulley angle initial and final values

and $a_{k,i}$ is the i-th order term coefficient for segment k. The coefficients are found using the Eq. 4.12 boundary conditions. A similar process is used to define the roll angle, with φ, φ_0 and φ_f replacing $\beta_{seg,k}$, $\beta_{seg,k,0}$, and $\beta_{seg,k,f}$.

$$\beta_{seg,k} = \begin{cases} \sum_{i=0}^{5} a_{k,i} t^i, & t_0 \leq t \leq t_f \\ \beta_{seg,k,f} & t > t_f \end{cases} \tag{4.11}$$

$$\begin{aligned} \beta_{seg,k}\left(t_0\right) &= \beta_{seg,k,0} & \dot{\beta}_{seg,k}\left(t_0\right) &= 0 & \ddot{\beta}_{seg,k}\left(t_0\right) &= 0 \\ \beta_{seg,k}\left(t_f\right) &= \beta_{seg,k,f} & \dot{\beta}_{seg,k}\left(t_f\right) &= 0 & \ddot{\beta}_{seg,k}\left(t_f\right) &= 0 \end{aligned} \tag{4.12}$$

Two case studies are considered: dynamic tail bending for a set of fixed roll angles, and dynamic tail rolling for a set of fixed bending angles. For both case studies, the tail's static loading when $\varphi = \beta_{seg,1\text{-}2} = 0°$ is subtracted from the calculated loading profile trajectories to show the loading as it would impact the legged robot on which the tail is mounted.

Figure 4.4 illustrates the $\boldsymbol{F}_B$ and $\boldsymbol{M}_B$ profiles for the first case, where $(t_0, t_f) = (0, 0.5)$ sec and $(\beta_{seg,1\text{-}2,0}, \beta_{seg,1\text{-}2,f}) = (0, 90)°$ with constant roll $\varphi = \{0, 45, 90\}°$. This means that the tail will perform dynamic tail motions where the 2 segments are synchronized in actuation to form configuration shape 1 where the input pulley angular displacements start at $0°$ (straight tail configuration) and ends at $90°$ for 3 distinct roll angles. The z-component of $\boldsymbol{F}_B$ ($F_{B,z}$), due primarily to centripetal acceleration, is invariant to the change in φ, given that the roll axis is z_T (Fig. 4.2); for the $\boldsymbol{M}_B$ z-component ($M_{B,z}$), as roll increases from $\varphi = 0°$, the gravitational forces acting over y-axis distances generates a larger moment at the base as φ increases. For the $\boldsymbol{F}_B$ x- and y-components, due to the centripetal and tangential accelerations of the tail masses, as φ increases, the time-varying component of $F_{B,x}$ re-allocates to $F_{B,y}$. The moments $M_{B,x}$ and $M_{B,y}$ are due to several factors: the moments due to the links' angular acceleration, the moments due to inertial forces from the links' linear acceleration, and the moments due to gravity acting on the links. Gravity primarily impacts $M_{B,y}$—the gravitational moment is greatest when $\beta_{seg,1\text{-}2} = 0°$ and least when $\beta_{seg,1\text{-}2} = 90°$. As with force, the roll angle re-allocates the inertial component between $M_{B,x}$ and $M_{B,y}$.

52

Figure 4.5 illustrates the loading profiles for the second case, where $(t_0, t_f) = (0, 0.5)$ sec and $(\varphi_0, \varphi_f) = (0, 90)°$ for the scenarios: $\beta_{seg,1\text{-}2} = [45, 45]$ °, $\beta_{seg,1\text{-}2} = [90, 90]$ ° , and $\beta_{seg,1\text{-}2} = [-21.75, 90]°$. In this case, the roll DOF is varied from 0° to 90° while maintaining a constant articulated tail configuration. The scenario $\beta_{seg, 1\text{-}2} = [-21.75; 90]°$ corresponds to a configuration shape 2 tail configuration with the tail COM located along the roll axis similar to a reaction wheel. For this case, the tail COM does not move during rotation, hence zero forces during the motion. However, since the tail is not axisymmetric (i.e., there are off-diagonal terms in the tail's inertia tensor), moments are generated in the x-, y- and z-directions.

For the three scenarios of $\beta_{seg,1\text{-}2}$, the tail COM is held at a fixed distance along the z-axis. Because there is no COM motion along the z-axis, there is no force in the z-direction, and the forces in the x-y plane are due to centripetal and tangential accelerations (as discussed earlier, static gravitational forces have been subtracted out). However for the $\beta_{seg, 1\text{-}2} = [45, 45]°$ and $\beta_{seg, 1\text{-}2} = [90, 90]°$ cases, gravity will generate moments in $M_{B,y}$ and $M_{B,z}$. For $M_{B,y}$, the non-zero initial moments are due to the reduced tail COM distance from the tail base for $\beta_{seg, 1\text{-}2} = [45, 45]°$ and $\beta_{seg, 1\text{-}2} = [90, 90]°$ compared to $\beta_{seg, 1\text{-}2} = 0°$ (the static loading for $\varphi = \beta_{seg, 1\text{-}2} = 0°$ includes a y-axis moment component). For $M_{B,z}$, as φ increases from 0 to 90°, the y-axis distance between the COM and tail base increases, creating a gravitational moment at the end time. For the inertial component of $M_{B,z}$, the tail's tangential acceleration generates a slight inertial moment that is secondary to the change due to gravity as $\beta_{seg, 1\text{-}2}$ increases.

It is important to note that the loading profiles of Fig. 4.5 can act over extended time durations due to infinite roll motion, similar to a reaction wheel, enabled via the slip ring; thus providing a performance advantage in comparison to existing tails reviewed in Chapter 2.
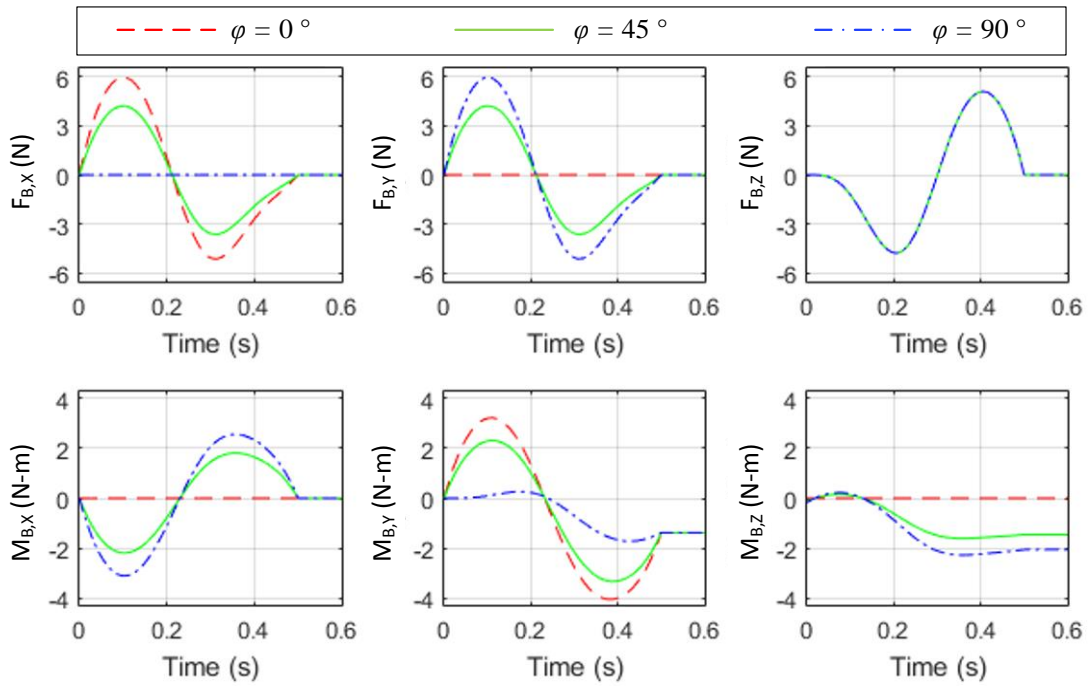
Figure 4.4: Simulation Results: Loading for dynamic tail bending at fixed roll angles.
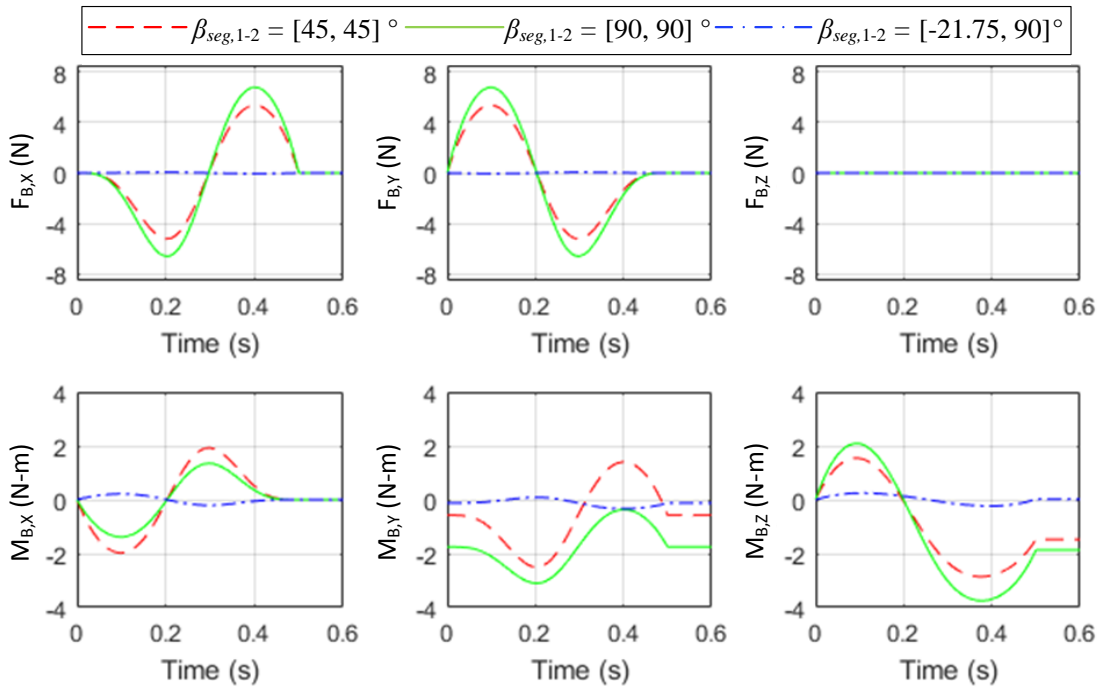
Figure 4.5: Simulation Results: Loading for dynamic tail rolling at fixed bending angles.

4.3 Experimental Prototype and Results

This section discusses the integration of the R3-RT prototype (section 4.3.1), along with experimental results demonstrating the R3-RT loading ability to verify the dynamic model (4.3.2), articulated structures' advantage over conventional pendulum structures in generating enhanced inertial loading (4.3.3), and the R3-RT's kinematic accuracy and repeatability (4.3.4).

4.3.1 Tail Implementation

Figure 4.6 shows the experimental prototype of the R3-RT. The links of the tail structure and frames of the rigid housing were printed using plastic. The remaining custom structural components were fabricated from metal (steel for shafts, aluminum for other components). Braided nylon cables (MagicShield) rated for 441 N (100 lbs) were used to actuate the tail; segment 1 actuation required double routed cable lines to accommodate the high impulsive tensions generated during tail motions. During integration, the cable routing was optimized though a series of experimental iterations to minimize friction effects by relieving aggressive cable routing angles about the small sized pins with passive rollers.

A distinctive feature of the R3-RT is its S-path and cylindrical cable routing scheme that enables decoupled actuation and equal antagonistic cable displacements as discussed in Chapter 3. Therefore, the two tail segments can be controlled by actuating their respective pulleys independently as illustrated in Fig. 4.7.
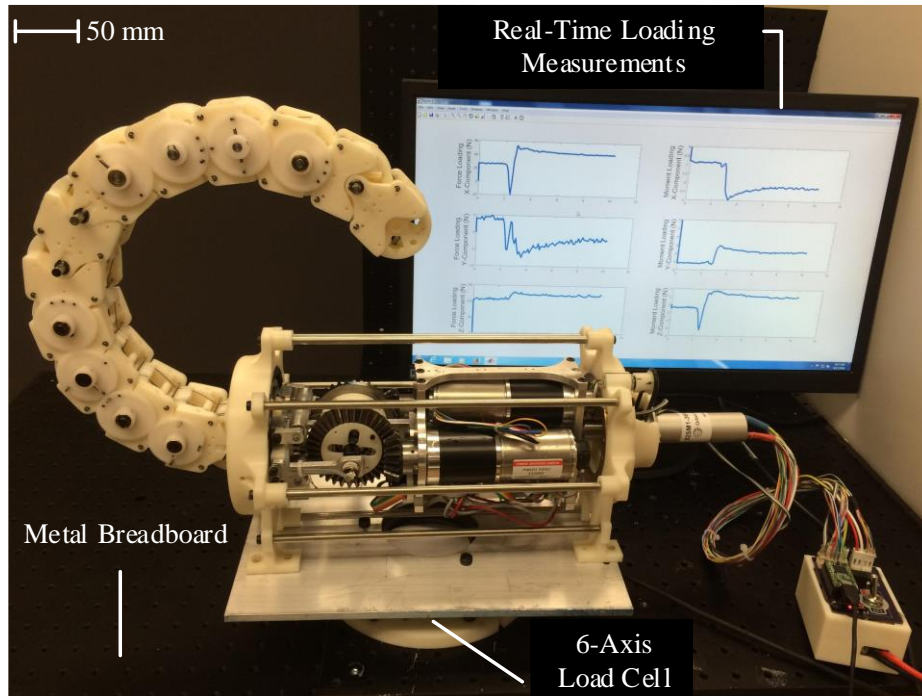
Figure 4.6: Experimental set-up of R3-RT.
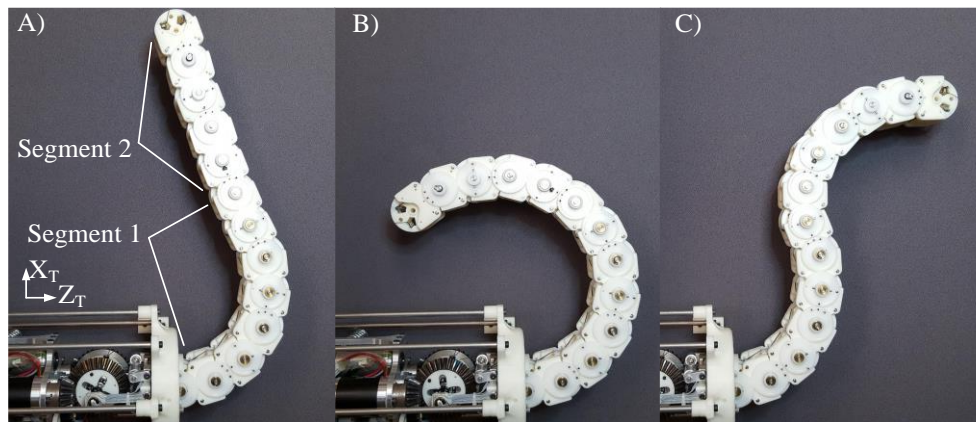
Figure 4.7: Flexibility of the R3-RT illustrating decoupled actuation with a constant roll angle of 0°: A) Variation of β_1 while β_2 remains fixed. Variation of β_2 while β_1 remains fixed depicting B) configuration shape 1, and C) configuration shape 2.

4.3.2 Loading Results

Experiments were performed to measure the tail's ability to generate dynamic loading using a 6-axis load cell as shown in Fig. 4.6. Sensor measurements were sampled at 400 Hz using a PCI data acquisition card. A moving window mean low-pass filter of width 50 sample points was used to

filter out high frequency sensor noise from the measured data; sufficient data was collected preceding the start of the tail motion to uniformly filter the relevant time span.

Tail bending motions, where $(t_0, t_f) = (0, 0.5)$ sec and $(\beta_{seg,1\text{-}2,0}, \beta_{seg, 1\text{-}2,f}) = (0, 90)°$ with constant roll $\varphi = \{0, 45, 90\}°$, were performed similar to the case scenarios presented in section 4.2.2, to compare measured loading profiles with computed simulation results. Figure 4.8 illustrates the measured loading profiles. Each case scenario was conducted three times with results averaged. From the plot, it can be observed that tail curvature motion is completed in 0.6 sec, after which the tail experiences vibrations that dissipate to steady state conditions.

Like the simulated results in Fig. 4.4, the measured loading profiles exhibit similar loading as the roll angle is varied: force loading about the z-axis shows an approximate invariance to various roll angles, gravitational moment loading offsets about the y- and z-axis at final tail configurations approximately match computed results, and profiles qualitatively match the shape of computed profiles and final steady state values, but do not exactly match the idealized smooth contours. This is considered to be acceptable performance and will validate the tails approach to replicated loading profiles about its base for experimental evaluation of developed control schemes conducted in Chapter 8.

As seen in Fig. 4.9, the experimental tail results exhibit similar peak magnitudes during the tail motion coupled with nontrivial lag behind the simulated trajectory. This is primarily due to the reliance on a feedback-based velocity controller for generating the tail motor inputs.
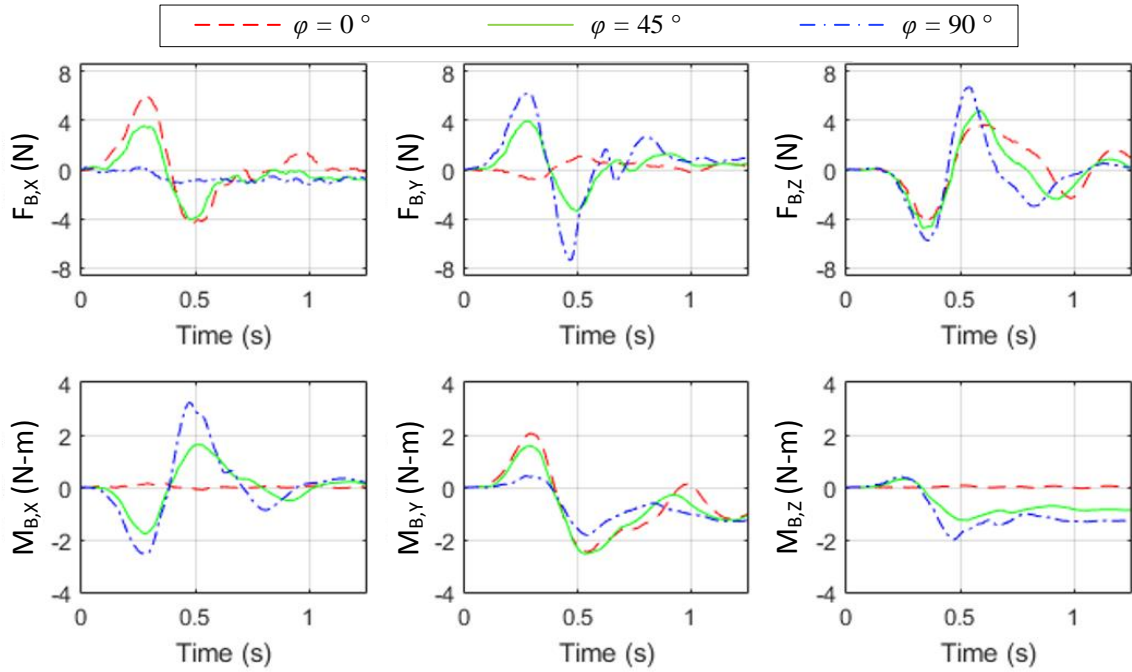
Figure 4.8: Experimentally measured loading profiles for fixed-roll experiments.
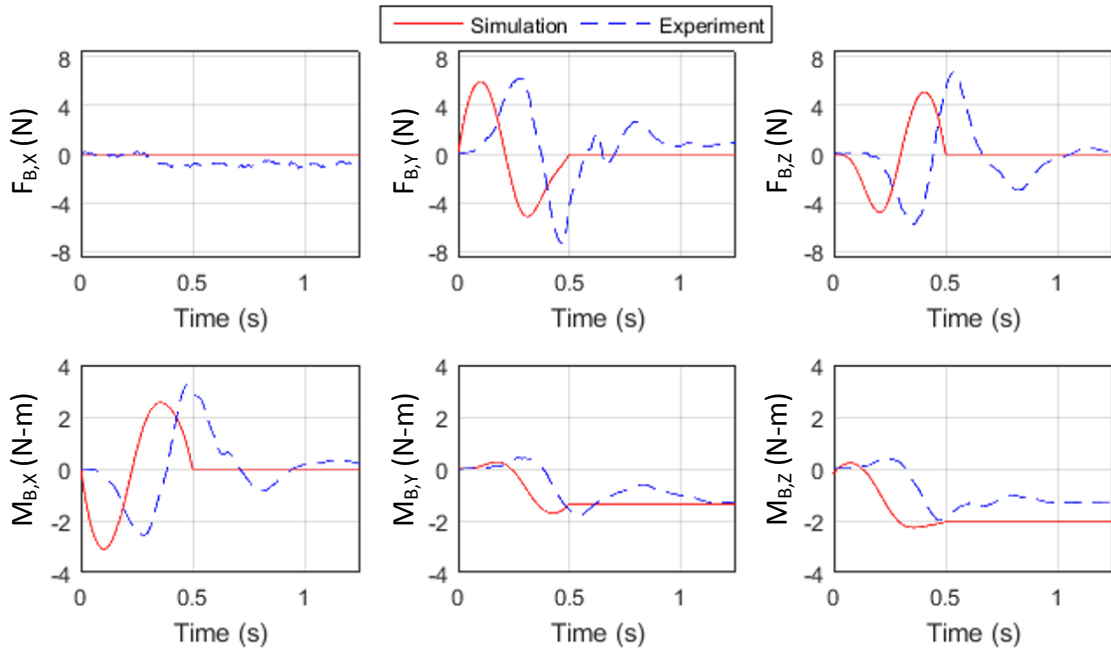
Figure 4.9: Comparison of simulation and experimental tail loading results when $\varphi = 90°$.

4.3.3 Comparing Articulated and Pendulum Inertial Loading

Experiments were performed to compare the inertial loading profiles of an articulated tail structure to a single-body rigid pendulum, a comparison that was analyzed in simulation in [15]. To maintain consistency in terms of mass distribution, the R3-RT tail consisting of 12 links was reconfigured into two structures: 1) an articulated single DOF tail segment with equal relative angle distribution constrained via 10 gear pairs (Fig. 4.10(A)), and 2) a single-body rigid pendulum with immobilized gears capable rotating about its link 1 revolute joint (Fig. 4.10(B)). For consistency in terms of power input and range of motion, both tail structures were actuated by prescribing a constant input cable tension as the tail rotated through its trajectory of equal cable displacement at a fixed roll angle of 90°, thus producing a planar horizontal tail motion unaffected by gravitational loading. The motions result in a COM angular displacement range equivalent to 104° and 180° for the articulated and pendulum-like tail, respectively.

Figure 4.11 illustrates the measured loading profiles for the articulated and single-body rigid pendulum tails for motions generated with constant cable tensions of 60 N and 110 N. These motions were performed three times for each tail structure with measured inertial loading results averaged to ensure consistency. The time spans to complete motions were slower for the articulated tail (60 N: 0.63 s, 110 N: 0.48 s) compared to the pendulum-like tail (60 N: 0.58 s, 110 N: 0.42 s). The articulated tail motions likely require slightly longer time spans due to cable friction along the structure. Table 4.2 presents the mean measured inertial loading of the loading shown in Fig. 4.11. Based off this data, for equivalent input cable displacements and constant cable tensions, the articulated tail, in comparison to the pendulum-like tail, on average provides: a 53% increase in generated moment about the base ($M_{B,X}$), a 52% reduction in $F_{B,Y}$, and an 8% increase in $F_{B,Z}$. Increased moments are beneficial for inertial adjustment applications because they produce angular re-orientation of the legged robot the tail is attached to. Decreased net forces are beneficial because forces may either aid or hinder inertial adjustment applications based on the state of the legged robot and due to the fact that forces result in system translation.

These experiments highlight the significance of increased articulation in tail structures to provide enhanced inertial loading about its attachment point in terms of increased moments and reduced forces that produce can produce more desirable effects in applications involving attitude adjustments, dynamic self-righting, and maneuvering as discussed in [31]; results which are corroborated in [15].
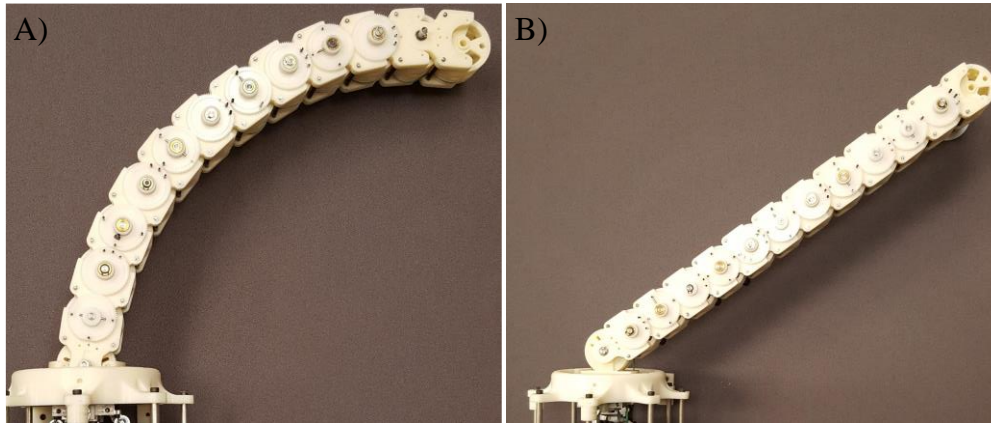
Figure 4.10: R3-RT structural configurations for comparative inertial loading experiments: A) Articulated, single DOF tail segment with motion distributed via 11 gear pairs, and B) Single-body rigid pendulum structure with immobilized gears.
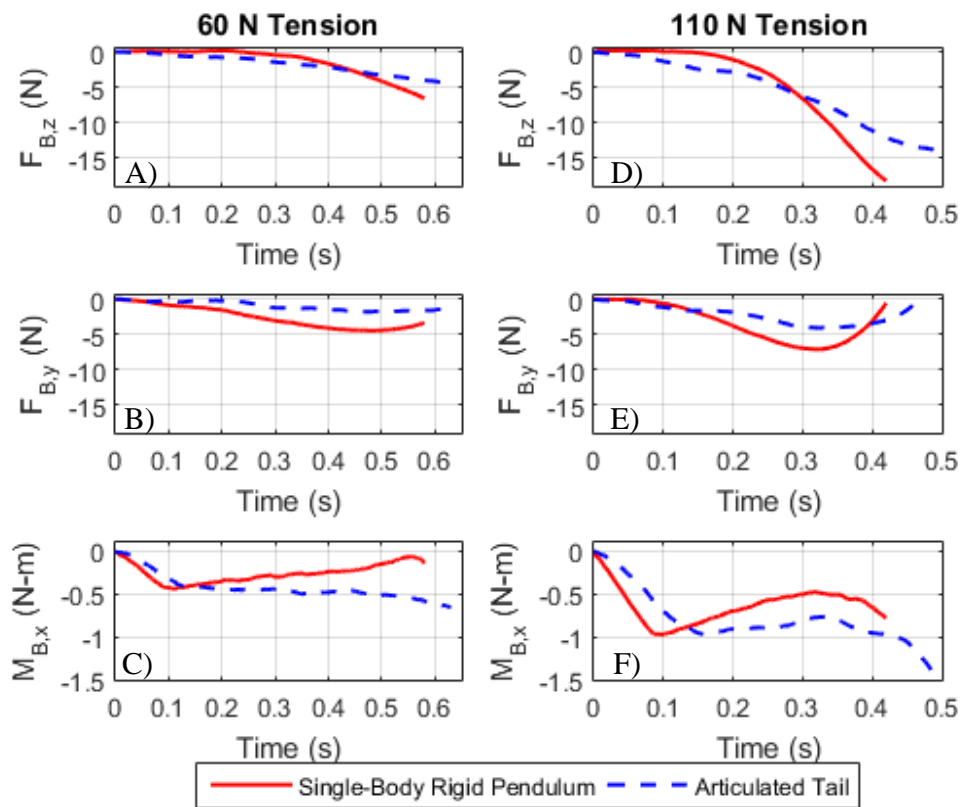
Figure 4.11: Experimentally measured loading profiles of articulated and rigid-body single pendulum tail strictures for a constant cable tension of 60 N (A-C) and 110 N (D-F).

Table 4.2: Mean measured loading profiles of articulated vs. single-body rigid pendulum tail in constant tension experiments.

Cable Tension	Tail Structure	$F_{B,Z}$ (N)	$F_{B,Y}$ (N)	$M_{B,X}$ (Nm)
60N	Articulated	-2.1	-1.06	-0.48
	Pendulum	-1.89	-2.83	-0.27
110N	Articulated	-6.7	-1.78	-0.93
	Pendulum	-6.36	-3.19	-0.72

4.3.4 Accuracy and Repeatability Results

In addition to analyzing the inertial loading generated by the R3-RT, the accuracy and repeatability of the cable-driven mechanism were also analyzed. Analyzing these parameters is critical for tasks involving precise COM adjustments and manipulation, due to the mechanism's need to effectively transition tension between the pair of cables actuating a segment without impacting the robot's configuration as it moves through a variety of configuration shapes and trajectories.

The R3-RT was programmed to cycle between the tail curvatures C1, C2 and C3 associated with pulley angles of $\beta_{seg,1-2} = [0]°$, $\beta_{seg,1-2} = [45]°$ and $\beta_{seg,1-2} = [90]°$ at a fixed roll angle of 90°. To measure the resulting individual joint angles, a Point Grey Blackfly camera (BFLY-U3-13S2M-CS) was mounted orthogonally to the R3-RT's bending plane. Image processing was used to measure the relative link orientations with respect to the tail's roll axis using 150 frames for each configuration over five consecutive cycles. Figure 4.12 shows the expected link angles (dotted line), and measured link angles (solid line with markers) for the twelve joints for the three configurations in the form of an error plot showing the measured mean ($\bar{\mu}$) and standard deviation ($\bar{\sigma}$).

For the C1 angles, slight offsets are observed from the home configuration—the largest offsets in each segment being 4.1° and 6.1° in segments 1 and 2, respectively. The primary factors that introduce these inconsistencies are gear backlash and slight cable slack. As each gear pair rotates, slight variations due to the tooth geometry will modify the relative angle between the links. For the cable tensions, it was found during set-up that a slight slack on one side of the cables was needed to prevent the mechanism from locking up during operation. Lock ups result from highly tensioned segment cables that prevent rotation in either direction and introduce a hysteresis-type effect in the links' responses to pulley inputs. These factors resulted in a repeatability that ranged from 2° to 5.1° in segment 1 and 3.1° to 6.7° in segment 2.

For configurations C2 and C3, Fig. 4.12 shows link 6 reaching angles 46.4° and 91.3°, minor variations from the predicted values, but a significant variation is noted in C3 joint 12: 169.5° measured for a predicted 180°. This is likely caused by the challenges of practical implementation of cable routing that are not nested perfectly along the link's cylindrical surfaces that cause slight variations of equal and opposite cable extension and retraction coupled with error accumulation over the joints.
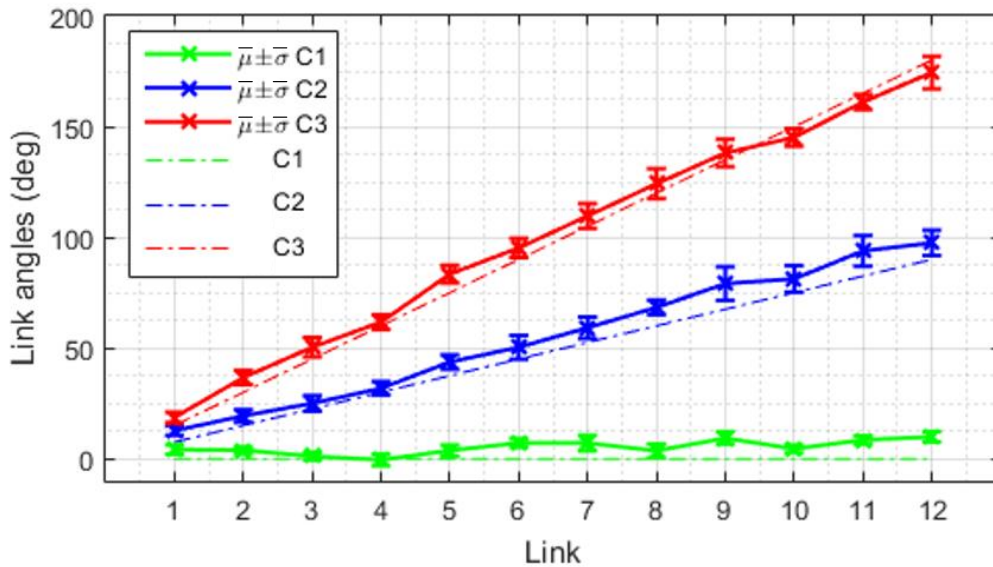
Figure 4.12: Repeatability experimental results showing mean and standard deviation of measured link angles and deviations (solid line and markers with standard deviation bars) from expected values (dotted line).

4.4 Conclusion

This chapter presented the kinematic and dynamic modeling of the R3-RT along with experimental results to validate models and test the mechanisms accuracy and repeatability for static stabilization applications and the performance in generating inertial loading for dynamic inertial adjustment applications.

Results of kinematic workspace analysis have demonstrated that the R3-RT produces a higher dimensionality end effector workspace due to its increased articulation and has significantly greater ability to adjust its COM due to the ability to change the distance between the COM and tail base, which is important for static stabilization applications. The R3-RT end effector workspace spans 270° and exceeds the proposed workspaces of previously implemented

pendulum-like tails presented in Table 2.1 However, the R3-RT COM workspace as shown in Fig. 4.3 falls 65° short with respect to [6, 40], reported in Table 2.1. This deficit can be overcome by adding a 450 g tip mass to match the 255° COM workspace and further increase the volume in which the COM can be positioned. The benefits of two configuration shapes further increases the manifold of inertial loading about the base of the tail by actuating various configuration shapes during tail motions [51]. For static stabilization applications, experimental results determined that the R3-RT can produce tail configurations with an accuracy and repeatability of 1.4±5.1° for segment 1 and 10.5±6.7° for segment 2.

To demonstrate an articulated tail's capability to generate enhanced inertial loading in comparison to previously implemented pendulum-like tails, experiments compared the generated inertial loading of the R3-RT in articulated mode with respect to the R3-RT configured in pendulum-like mode. Results indicate that for equivalent input cable displacements and constant cable tensions, the articulated mode, in comparison to the pendulum-like mode, on average provides: a 53% increase in generated moment about the base ($M_{B,X}$), a 52% reduction in $F_{B,Y}$, and an 8% increase in $F_{B,Z}$. These results demonstrate that articulated tails generate enhanced loading in comparison to pendulum-like structures because increased generated moments are beneficial for inertial adjustment applications since they result in rotation of the system to which the tail is attached to and can more significantly impact the system's performance, whether it be for maneuvering or stabilization applications. Generated forces result in undesirable translation that is not beneficial for inertial adjustment. Furthermore, the prototype demonstrated satisfactory accuracy and repeatability, which makes it appealing for use in static loading based applications for precise COM positioning, i.e. static stabilization of a legged robot.

Experimental results have demonstrated that measured peak loading profile values equal to 6 N and 3.1 N-m fall slightly below computed values using the dynamic loading model because the experimental tail motion duration was slightly longer than the 0.5 s time span used in computed results. This is expected since inertial loading decreases towards steady state gravitational loading conditions as the time spans of tail motions are lengthened. The performance of the R3-RT in producing inertial loading is considered to be acceptable performance and will validate the tails approach to replicate loading profiles about its base for experimental validation of developed control schemes demonstrated in Chapter 8.

CHAPTER 5: MODELING, ANALYSIS, AND EXPERIMENTATION OF DMST

Chapter 3 presented the detailed design of the DMST tail mechanism that is intended for inertial adjustment of a lighter weight biped robot attached in a vertical configuration as will be demonstrated in Chapters 5 and 8. This chapter presents the kinematic and dynamic model of the DMST (section 5.1) tail, accounting for the system's kinematic coupling between linkages and the cable-driven actuation using a multi-diameter pulley. These dynamic models are used to analyze the workspace and impact of motion and tail configuration on the loading profiles, generated forces and moments generated due to tail motions, transferred through the tail base that will eventually be applied to the legged robot for inertial adjustment applications (section 5.2). Then, experiments using integrated prototypes are performed (section 5.3) to validate the forward kinematic and dynamic models, determine the mechanism's accuracy and repeatability, and measure the mechanism's ability to generate inertial loading.

5.1 Kinematic and Dynamic Modeling

After analyzing the kinematic coupling created in the mechanism by the actuation cabling, the kinematics and dynamics of the mechanism are derived. Section 5.1.1 presents how joint angles change with respect to input angles due to kinematic coupling. Section 5.1.2 derives the position, velocity, and acceleration of each rigid link in the tail structure. An actuation loading model is then presented in section 5.1.3 to compute the required torques to produce tail motions and section 5.1.4 presents the method to compute generated inertial loading at the tail base as a result of tail motions.

5.1.1 Joint Angle Trajectory

The actuation cabling between the MDP and links creates a kinematic coupling between the MDP rotation and each link's joint angle (assuming the cable is inextensible). However, the cable routing for link $i > 1$ will route along the previous i-1 links. Therefore, the cable path length change due to these joint angles must be considered.

With reference to Fig. 5.1, Eq. 5.1 recursively maps the prescribed MDP motor joint angle ϑ_m into the relative linkage angles ϑ_i, where η_i (defined in Eq. 5.2) is the coupling ratio between r_i, the MDP i-th radius for the cable terminating at link i, and r_{cbl} is the radius of the circular cable routing surfaces. These parameters are shown in Fig. 2 for a two-link DMST. The roll joint angle ϕ equals the prescribed motor angle ϕ_m due to direct drive, also defined in Eq. 5.1. The associated joint velocities $\dot{\phi}$ and $\dot{\vartheta}_i$ and accelerations $\ddot{\phi}$ and $\ddot{\vartheta}_i$ may be found by differentiating Eq. 5.1.

$$\vartheta_i = \begin{cases} \eta_i \vartheta_m & i = 1 \\ \eta_i \vartheta_m - \sum_{j=1}^{i-1} \vartheta_j & 1 \leq i \leq n \end{cases}$$

$$\phi = \phi_m \tag{5.1}$$

$$\eta_i = r_i / r_{cbl} \tag{5.2}$$
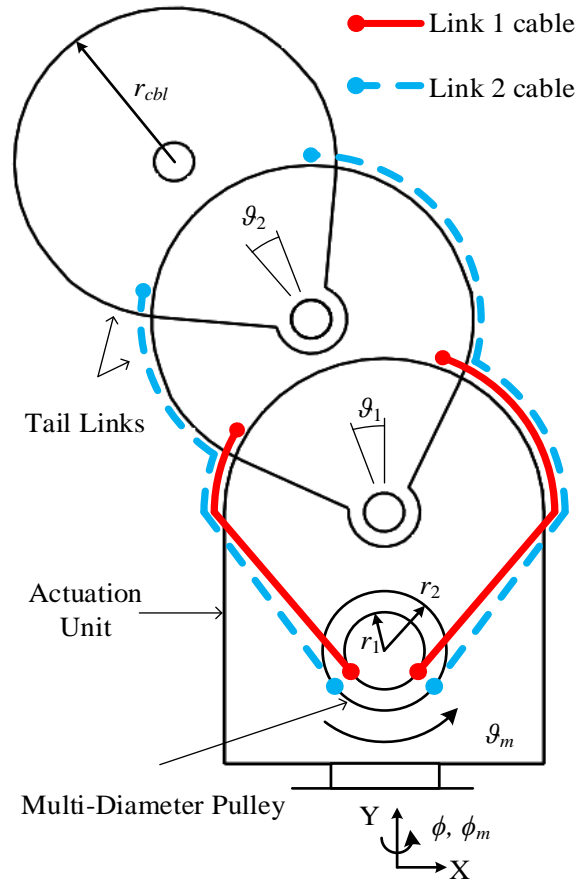
Figure 5.1: Schematic Diagram of DMST.

5.1.2 Linkage Position, Velocity, and Acceleration

Kinematic illustrations of the base link (link 0), intermediate links (links 1 through *n*-1), and terminal link (link *n*) are shown in Fig. 5.2, with relevant frame and kinematic parameters used in this analysis defined graphically.
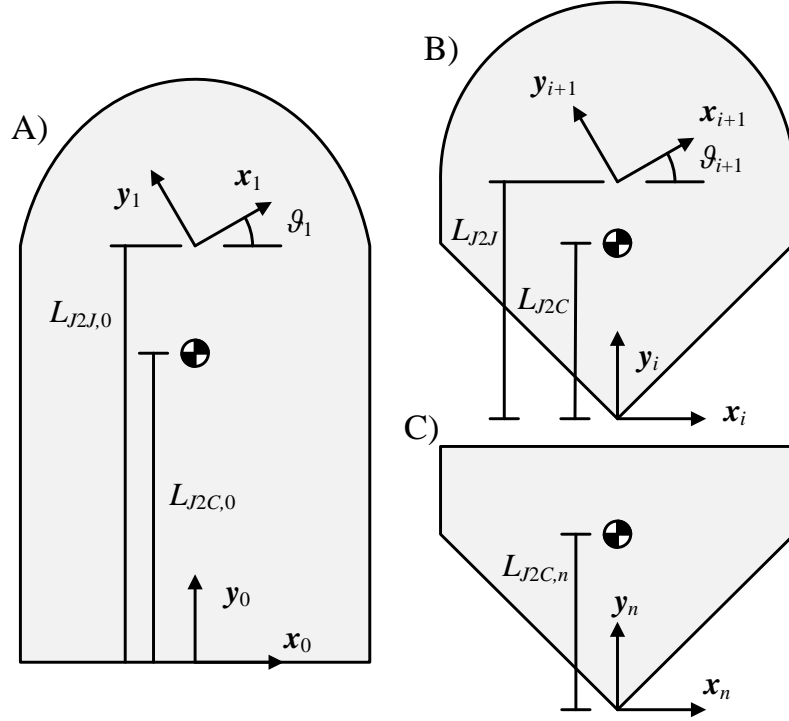
Figure 5.2: Kinematic illustrations of DMST links: A) base link 0, B) intermediate link 1-n, and C) terminal link n.

The link i orientation matrix $\mathbf{R}_i$ is defined in Eq. 5.3, where $\mathbf{R}_Y(\phi)$ is a y-axis rotation by angle ϕ and $\mathbf{R}_Z(\vartheta_i)$ is a z-axis rotation by angle ϑ_i. The body 0 rotation is due to the roll of link 0 with respect to the tail base frame, and the body i rotation is due to the pitch of link i with respect to link i-1.

$$
\mathbf{R}_i = \begin{cases} \mathbf{R}_Y(\phi) & i = 0 \\ \mathbf{R}_{i-1}\mathbf{R}_Z(\theta_i) & 1 \leq i \leq n \end{cases}
\tag{5.3}
$$

As shown in Fig. 5.2, the positions of the tail's i-th link joint centers $\mathbf{p}_{i,jnt}$ and link COM $\mathbf{p}_{i,COM}$, are calculated using Eqs. 5.4-5.5, where $L_{J2J,0}$ is the distance from the roll joint to pitch joint 1, $\mathbf{y}$ is the y-axis unit vector, L_{J2J} is the distance between adjacent pitch joints, $L_{J2C,0}$ is the distance from joint 0 to the link 0 COM, L_{J2C} is the distance between an intermediate link's pitch joint and COM, and $L_{J2C,n}$ is the distance between joint n and the link n COM.

$$\boldsymbol{p}_{i,jnt} = \begin{cases} \boldsymbol{0} & i = 0 \\ \boldsymbol{p}_{i,jnt} + L_{J2J,0}\boldsymbol{R}_{i-1}\boldsymbol{y} & i = 1 \\ \boldsymbol{p}_{i,jnt} + L_{J2J}\boldsymbol{R}_{i-1}\boldsymbol{y} & 2 \le i \le n \end{cases} \tag{5.4}$$

$$\boldsymbol{p}_{i,COM} = \begin{cases} \boldsymbol{p}_{i,jnt} + L_{J2C,0}\boldsymbol{R}_i\boldsymbol{y} & i = 0 \\ \boldsymbol{p}_{i,jnt} + L_{J2C}\boldsymbol{R}_i\boldsymbol{y} & 1 \le i \le n-1 \\ \boldsymbol{p}_{i,jnt} + L_{J2C,n}\boldsymbol{R}_i\boldsymbol{y} & i = n \end{cases} \tag{5.5}$$

Link i angular velocities $\boldsymbol{\omega}_i$ are defined in Eq. 5.6, where z is the z-axis unit vector.

$$\boldsymbol{\omega}_i = \begin{cases} \dot{\phi}\boldsymbol{R}_i\boldsymbol{y} & i = 0 \\ \boldsymbol{\omega}_{i-1} + \dot{\vartheta}_i\boldsymbol{R}_i\boldsymbol{z} & 1 \le i \le n \end{cases} \tag{5.6}$$

The linear velocities $\boldsymbol{v}_{i,jnt}$ and $\boldsymbol{v}_{i,COM}$ may be found by differentiating Eqs. 5.4-5.5, using the property $\dot{\boldsymbol{R}}_i = \tilde{\boldsymbol{\omega}}_i\boldsymbol{R}_i$, where $\tilde{\boldsymbol{a}}$ denotes the skew-symmetric matrix mapping of vector $\boldsymbol{a}$ such that $\tilde{\boldsymbol{a}}\boldsymbol{b} = \boldsymbol{a}\times\boldsymbol{b}$. The angular accelerations are found by differentiating Eq. 5.6. The linear accelerations $\boldsymbol{a}_{i,jnt}$ and $\boldsymbol{a}_{i,COM}$ may be found by differentiating $\boldsymbol{v}_{i,jnt}$ and $\boldsymbol{v}_{i,COM}$.

5.1.3 Actuation Loading Requirements

For this robotic structure, three sources of loading are considered: inertia, gravity and actuation. The inertial force $\boldsymbol{F}_{i,inr}$ and moment $\boldsymbol{M}_{i,inr}$ and gravitational force $\boldsymbol{F}_{i,grv}$ acting at each link i COM as external loading, while the actuation contributes to the joint moment $\boldsymbol{M}_{i,jnt}$ as discussed below. Because the joint angles are prescribed, the kinematics, the inertial loading can be directly calculated from the applied trajectories; the only unknowns are the joint forces $\boldsymbol{F}_{i,jnt}$ and moments $\boldsymbol{M}_{i,jnt}$.

Figure 5.3 illustrates free body diagrams for the terminal link and an intermediate link of the DMST. A recursive formulation of the equations of motion (starting from the n-th link and propagating to $n = 0$) based on these free body diagrams are defined in Eq. 5.7, where $\boldsymbol{p}_{i,j,CJ}$ is the position vector from the link i COM to joint j, defined in Eq. 5.8.
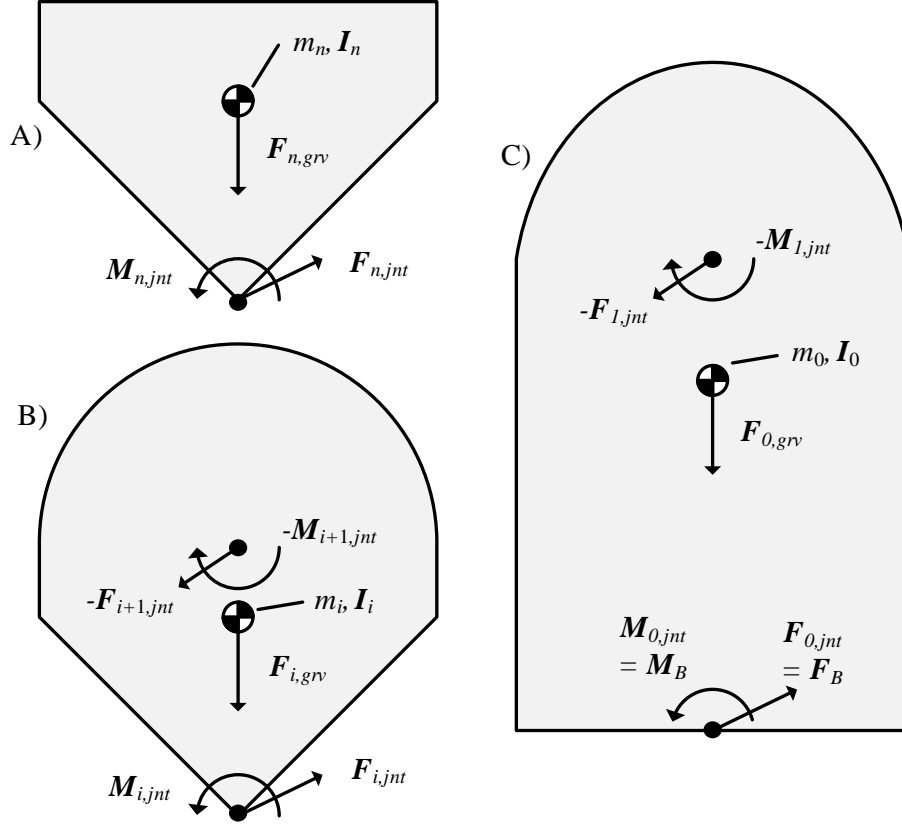
Figure 5.3: Free body diagrams of DMST links: A) terminal link n, B) intermediate link i, C) base link 0.

$$F_{i,inr} = \begin{cases} F_{i,jnt} + F_{i,grv} & i = n \\ -F_{i+1,jnt} + F_{i,jnt} + F_{i,grv} & 0 \le i \le n-1 \end{cases} \tag{5.7}$$

$$M_{i,inr} = \begin{cases} M_{i,jnt} + \tilde{p}_{i,i,CJ} F_{i,jnt} & i = n \\ -M_{i+1,jnt} + M_{i,jnt} - \tilde{p}_{i,i+1,CJ} F_{i+1,jnt} + \tilde{p}_{i,i,CJ} F_{i,jnt} & 0 \le i \le n-1 \end{cases}$$

$$p_{i,j,CJ} = p_{jnt,j} - p_{COM,i} \tag{5.8}$$

These equations of motion may be reorganized into recursive formulations of joint load forces $F_{i,jnt}$ defined in Eq. 5.9, where m_i is the link i mass and g is gravitational acceleration.

$$F_{i,jnt} = \begin{cases} m_i \left(\ddot{p}_{i,COM} - \mathbf{a}_{grv} \right) & i = n \\ F_{i+1,jnt} + m_i \left(\ddot{p}_{i,COM} - \mathbf{a}_{grv} \right) & 0 \le i \le n-1 \end{cases}, \quad \mathbf{a}_{grv} = -g\mathbf{y} \tag{5.9}$$

Equation 5.10 defines the recursive formulation of joint load moments $M_{i,jnt}$, for which $M_{i,inr}$ is defined in Eq. 5.11. In Eq. 5.11, I_i is the link i moment of inertia with respect to the ground frame, and $I_{i,lcl}$ is the link i moment of inertia with respect to the link i frame. The subscript lcl is used to identify the constant inertia tensor defined in the local body-fixed frame.

$$M_{i,jnt} = \begin{cases} M_{i,inr} - \tilde{p}_{i,i,CJ} F_{i,jnt} & i = n \\ M_{i,inr} + M_{i+1,jnt} + \tilde{p}_{i,i+1,CJ} F_{i+1,jnt} - \tilde{p}_{i,i,CJ} F_{i,jnt} & 0 \le i \le n-1 \end{cases} \tag{5.10}$$

$$M_{i,inr} = I_i \dot{\omega}_i + \tilde{\omega}_i I_i \omega_i \quad , \quad I_i = R_i I_{i,lcl} R_i^T \tag{5.11}$$

The defining property of a revolute joint is that it cannot support a moment along its axis of rotation. Therefore, for each revolute joint i, the actuation loading must provide the moment in $M_{i,jnt}$ aligned with the revolute joint axis of rotation. The actuation loading differs for joint 0 and joints 1-n. For joint 0, the revolute joint axis is $R_0 \mathbf{y}$, and the moment about this axis is a torque τ_r directly provided by the roll-DOF gear motor output shaft, defined in Eq. 5.12.

$$\tau_r = \left(R_0 \mathbf{y} \right)^T M_{0,jnt} \tag{5.12}$$

For joints $i = 1$-n, the revolute joint axis is defined as $R_{,i} \mathbf{z}$ and the moment along this axis is due to the cable tensions acting between links i-1 and i. For an n-link DMST, there will be n cable tensions contributing to this moment, and the normal distance from the revolute joint to these tensions is r_{cbl}, resulting in the cable tension formulation in Eq. 5.13, where $T_{i,j}$ is the tension at joint i of the cable terminating at link j.

$$r_{cbl} \sum_{j=i}^{n} T_{i,j} = \left(R_i \mathbf{z} \right)^T M_{i,jnt} \tag{5.13}$$

70

For the cable tensions, assuming there is friction between the cable and tail structure along its length, recursive calculation of the cables' tensions from their termination point to the base is required. For a given j, $T_{i,j}$ will be non-zero only for $i = [1, j]$.

Solving for $T_{i,j}$ consists of two steps performed recursively from joint $i = n$ to joint $i = 1$: 1) calculating the $T_{i,i}$ tension using Eq. 5.14, and 2) back-propagating the joint i tensions to joint i-1 using Eq. 5.15, where μ is the coefficient of friction and χ_i is the contact angle between the cable and routing surfaces. Equation 5.14 was derived from Eq. 5.13 knowing that $T_{i,j} = 0$ for all $j < i$, and Eq. 5.15 was found using a belt-friction model for the contact between the cable and routing surfaces between joints.

$$r_{cbl}T_{i,i} = \begin{cases} \left(R_i z\right)^T M_{i,jnt} & i = n \\ \left(R_i z\right)^T M_{i,jnt} - r_{cbl}\sum_{j=i+1}^{n} T_{i,j} & 1 \leq i \leq n-1 \end{cases} \tag{5.14}$$

$$T_{i,j} = \exp\left(\mu\chi_{i+1}\right)T_{i+1,j} \quad \forall j \geq i \tag{5.15}$$

The torque τ_s required to drive the MDP may be calculated using Eq. 5.16, which takes the sum of the moments due to each cable tension acting over that cable's pulley radius.

$$\tau_s = \sum_{i=1}^{n}\left(r_i T_{0,i}\right) \tag{5.16}$$

5.1.4 Dynamic Tail Loading Model

Beyond understanding the actuation requirements of the DMST, the dynamic model should also be capable of calculating the loading (force and moment) the DMST applies through its roll joint.

The recursive calculations of $F_{i,jnt}$ and $M_{i,jnt}$ accumulate the loading due to the links' inertial and gravitational loading from the tip to the actuation module. Therefore, using the joint loading at link 0, the tail base loading F_B and M_B may be calculated using Eq. 5.17. The ground frame in

which the tail model is defined is assumed to be located at the attachment point between the tail and legged structure.

$$F_B = F_{0,jnt} \quad , \quad M_B = M_{0,jnt} \tag{5.17}$$

5.2 Tail Analysis

This section analyzes the kinematic workspace (section 5.2.1) and loading capabilities of the DMST (section 5.2.2) while varying trajectory and design parameters to further understand the factors that contribute to generated forces and moments generated at the base of the tail.

5.2.1 Kinematic Workspace Analysis

The proposed mechanism is articulated in structure and a single DMST can form a single-curvature spatial tail configuration. Figure 5.4 shows the single configuration shape that can be generated by a single 5-segment DMST. Unlike the R3-RT that is capable of forming two configuration shapes as discussed in section 4.2.1, the DMST is capable of forming a C-shaped curvature with segments rotated in the same direction denoted as configuration shape 1.

The end effector and COM workspace are defined by the locus of positions the end effector tip (link 5) and COM can reach, respectfully. The defined workspaces can be computed using the forward kinematics (sections 5.1.1-5.1.2) using the geometric parameters extracted from the DMST CAD (Fig. 3.9), defined in Table 4.1. Figure 5.4 shows the R3-RT's simulated planar workspaces (end effector and COM with/without tip mass) for a fixed roll angle at 0° where the multi-diameter pulley is varied between $\vartheta_m = [-90:90]°$. The coordinate frame origin is the DMST joint 1.

The end effector workspace is capable of spanning 90°, falling much shorter than the end effector workspace of the R3-RT (section 4.2.1), that can span up to 270° for an input angle of $\beta_{seg,1\text{-}2} = [-135:135]°$ due to its less articulated DOFs. A tail's COM workspace is defined by its range of motion, mass distribution, link geometry, and number of independently actuated tail segments. For the DMST, the COM workspace with no added tip-mass, illustrated with a green line in Fig. 5.4, can be displaced along the X-axis up to 100 mm. With the addition of a tip mass with $m_5 = 3.5$ kg, illustrated with a red line, the COM workspace is increased and can be displaced 280 mm along the x-axis. As will be demonstrated in Chapter 8, the DMST requires this additional

tip mass to successfully stabilize the biped to position the system's combined COM within the support polygon during a walking gait.

Similar to pendulum-like tails, the DMST can only produce end effector and COM workspaces about a curve in a plane without considering roll motion. When considering roll motion, this curve becomes a surface. Therefore, a single 5 link DMST cannot produce a volume in space to position its COM as the R3-RT that is enabled via the motions of two independently actuated tail curvatures. However, these capabilities are achievable for multiple DMST modules connected in series, a concept presented in section 3.4 but not practically implemented as part of this research.

These results further emphasize the importance of increased articulation and multi-curvature tail configuration shapes that can produce a higher dimensionality end effector workspace and a greater ability to adjust its COM which is important for both dynamic inertial adjustment and static stabilization applications, as discussed in section 4.2.1.
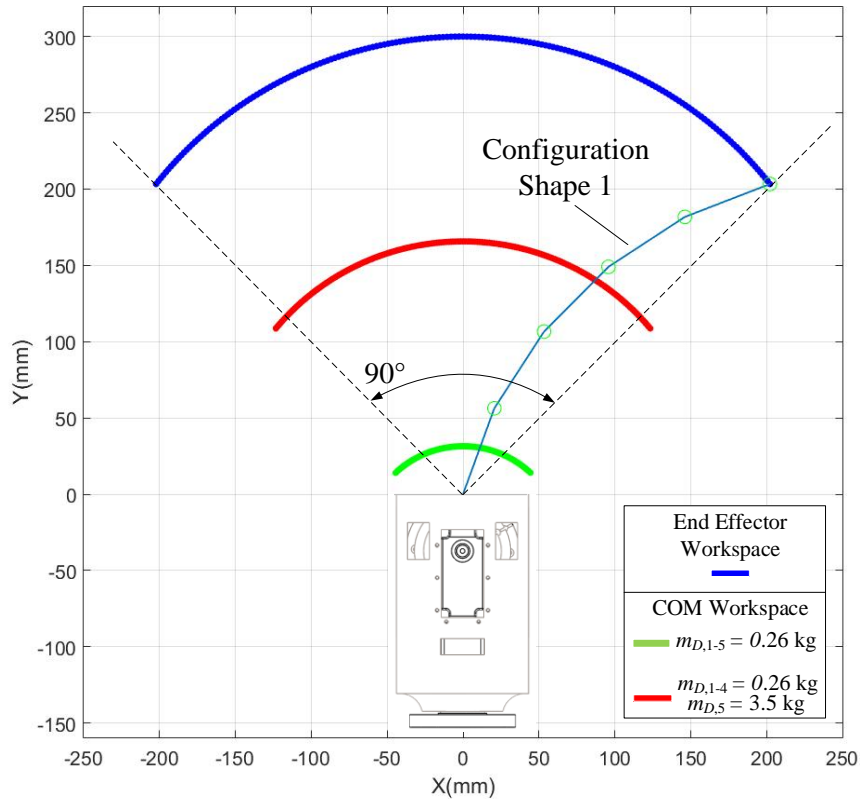
Figure 5.4: Workspace and configuration shape of a 5-link DMST for $\vartheta_m = [-90:90]°$.

Table 5.1: Simulation parameters for the 5-link DMST.

Property	Value	Property	Value
$L_{0,J2C0}$	63.3 mm	m_0	0.350 kg
L_{J2C}	59 mm	$m_{\{1\text{-}5\}}$	0.26 kg
$L_{J2C,n}$	49 mm	$L_{J2J,0}$	105.25 mm
r_i	[9, 16, 22, 28, 34] mm	L_{J2J}	60 mm
		r_{cbl}	25 mm

$$I_{0,lcl} = \begin{bmatrix} 0.0038 & 0 & 0 \\ 0 & 0.0014 & 0 \\ 0 & 0 & 0.0031 \end{bmatrix} \text{kg}-\text{m}^2, \; I_{1-5,lcl} = \begin{bmatrix} 0.6 & 0 & 0 \\ 0 & 0.6 & 0 \\ 0 & 0 & 0.5 \end{bmatrix} \times 10^{-3} \text{kg}-\text{m}^2$$

5.2.2 Dynamic Tail Loading Analysis

In the following analysis, the dynamic model of the DMST, developed in section 5.1, is used to simulate the system actuated with PID controlled servo motors. Experimentally measured data of the servo plant parameters including inertia, friction, damping and torque/speed saturations were extracted from [82] and controller gain coefficients were tuned for near-critical operation on the bases of empirical analysis that were set to $K_p = 60$, $K_i = 10$, and $K_d = 0.4$. The dynamics of the system were used to evaluate Eq. 5.17. A five-link DMST is considered with the simulation parameters presented in Table 5.1, unless otherwise stated, to compare results with experimental prototype results as discussed in section 5.3. Mass properties are estimated from a detailed CAD model. Furthermore, the dynamic loading profiles utilize the global coordinate frame of reference defined in Fig. 5.1.

5.2.2.1 Trajectory – Inertial Analysis

Tail loading profiles are influenced by both static loading (gravity) and dynamic loading (inertia). Since gravitational effects are time-invariant (do not depend on velocity or acceleration), they are the same for a prescribed tail trajectory regardless of the tail motion's time span. However, inertial effects are time-variant since greater accelerations correspond to greater magnitude loading profiles. Therefore, the inertial loading acts as perturbation to the steady-state gravitational loading. In this analysis, only planar bending is considered where ϑ_m is varied from 0 to the target position of $\pi/2$ rad to simulate a servo step response with various time spans, representing the

duration of tail motion, to study its effect on inertial loading. Figure 5.5 presents the force and moments loading diagrams for the three time span case studies $t = \{0.2, 0.3, 0.4\}$ sec. The time span of 0.2 sec represents the fastest step response the system can achieve the target position. Time spans were elongated by reducing the proportional gain constant. To better visualize the perturbations from equilibrium, steady state gravitational force offsets about the y-axis were set to zero.
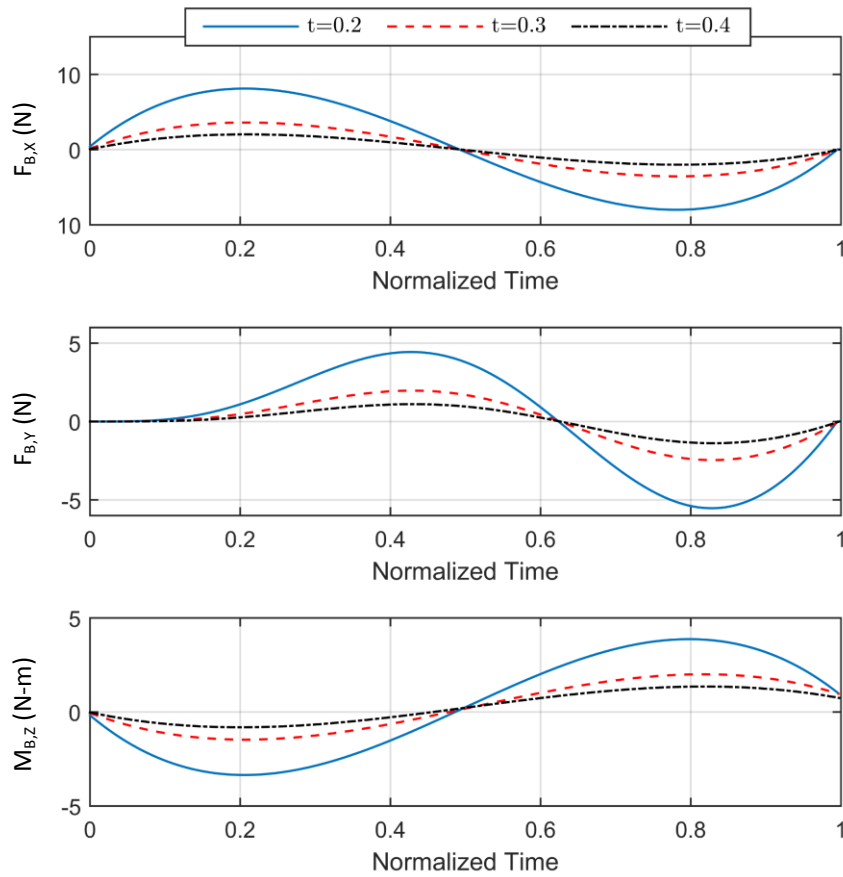
Figure 5.5: Inertial analysis: computed loading profiles for $t = \{0.2, 0.3, 0.4\}$ sec. The x-axis time is normalized as a fraction of the total duration to aid comparison.

It is observed from these plots that force loading profiles magnitudes: 1) increase as the time span decreases for each tail motion due to greater accelerations, and 2) approach a steady

state profile as time spans increase due to the time invariance of gravitational effects. It is also noted that x- and y-components of the force loading ($F_{B,x}$ and $F_{B,y}$) at the endpoints are zero because these instances represent static configurations with zero velocities and accelerations; however, the final z-component moment loading ($M_{B,z}$) is offset due to the gravitational induced moment at the tail's end configuration.

5.2.2.2 Trajectory – Roll Analysis

In section 5.2.2.1, a planar case study was analyzed in which the time span of the tail's bending motion was varied. However, roll angle is another trajectory parameter that can be varied to distribute loading. In this analysis, simulations are performed using the 0.2 sec time span tail trajectories (similar to motion used in section 5.2.2.1) where the roll angle is varied at constant values $\phi = \{\pi/4, \pi/2, 3\pi/4\}$ rad.

Figure 5.6 illustrates the associated loading results. Due to the rotational symmetry of the tail motions about the y-axis, the loading with respect to this axis (i.e., the y-components of force and moment) is invariant to the change in ϕ. Furthermore, since the tail is performing tail curvature motions at constant roll angles, the y-component moment loading is zero.

The x- and z-components show the impact of roll angle on the distribution of the loading profiles. For $\phi = \pi/4$ and $3\pi/4$ rad, x-component force and z-component moment profiles are equal and opposite, whereas the x-component moment and z-component force are equal in these two cases.
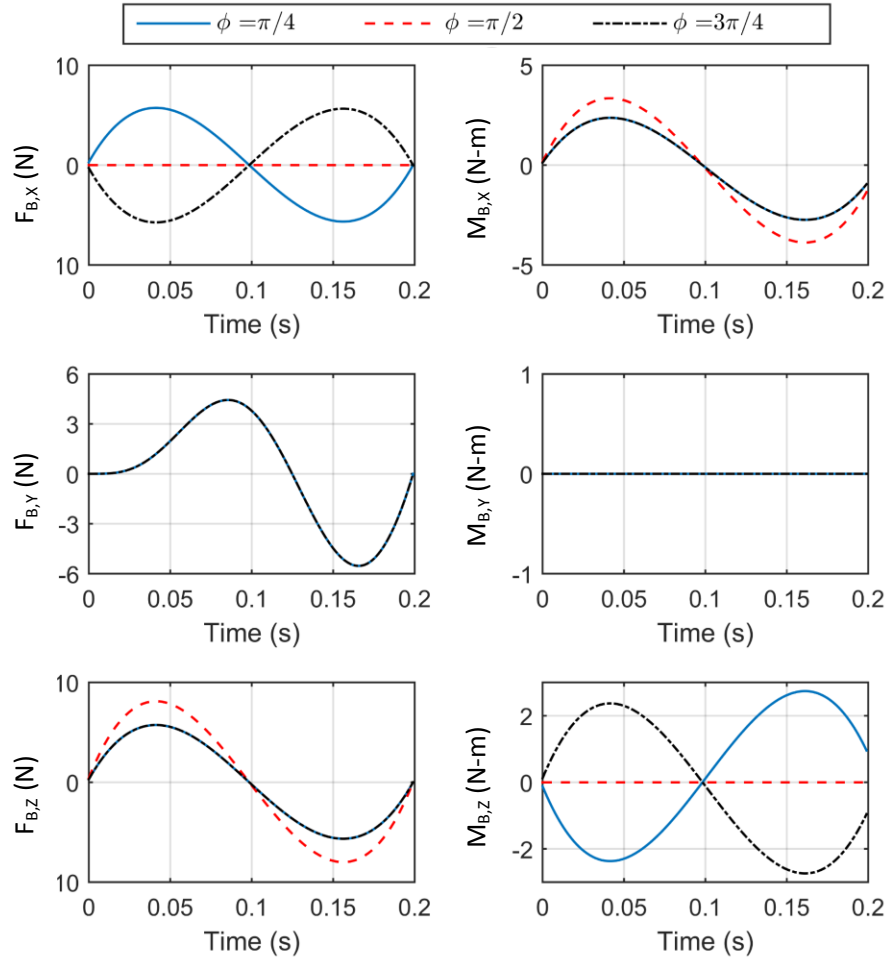
Figure 5.6: Roll angle analysis: computed loading profiles for $\phi = \{\pi/4, \pi/2, 3\pi/4\}$ rad.

5.2.2.3 Design – Mass Distribution Analysis

In addition to trajectory parameters, a tail's design properties also impact the dynamic loading. Two design factors will be analyzed in this paper: mass distribution and coupling ratio. All design parameter analysis will use tail curvature motion with a 0.2 sec time span (similar to motion used in section 5.2.2.1).

The DMST is designed to accommodate a tip mass to increase the loading capacity for a given tail motion. This section analyzes the effects of the mass distribution ratio η on loading profiles, where η represents the ratio between an additional tip mass and the total weight of the tail (links and actuation unit). In this analysis, the total weight of the 5-link DMST is 4.3 kg. All

other design variables and properties are held constant to compare results with inertial analysis loading profiles.

Three case studies are presented in Fig. 5.7 that show force loading profiles where the mass distribution ratio is varied between three values $m = \{0.5, 1, 1.5\}$ representing an additional tip mass equivalent to $\{2.1, 4.3, 8.6\}$ kg attached to link 5.

Results indicate a linear correlation between the increase of tip mass and loading profiles magnitudes. In comparison to inertial analysis results with no tip mass, loading profile magnitudes increase approximately by factors of 3.2, 5.5, and 7.8 for m equal to 0.5, 1, and 1.5 respectively.

Although increasing tip mass generates larger magnitude dynamic force loading profiles, a maximum limit of additional tip mass is imposed by motor specifications. Using Eq. 5.16, the MDP torque requirements were computed for the m values under consideration, with results shown in Fig. 5.8. It is observed that the required torque for all case scenarios initially take on positive values to overcome inertia to move the tail in the positive orientation, then changes to negative values and attains maximum magnitudes during the deceleration phase then remains offset in this region due to gravitational loading. Mass distribution parameters must be chosen based on MDP angular velocity and torque requirements to select a motor that is capable of producing a desired tail motion.
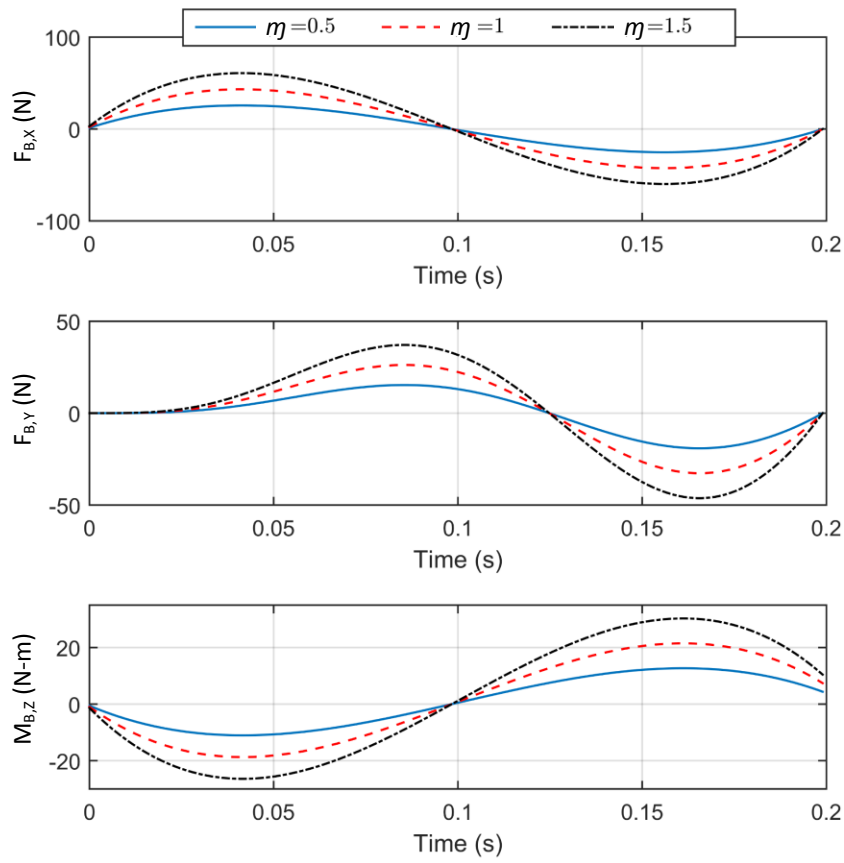
Figure 5.7: Mass distribution analysis: computed loading profiles for $m = \{0.5, 1, 1.5\}$.
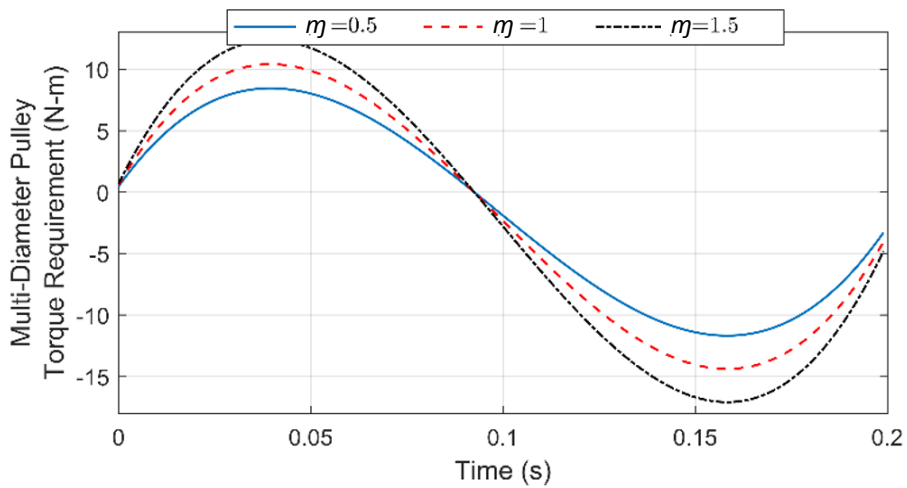
Figure 5.8: Computed MDP torque requirements for $m = \{0.5, 1, 1.5\}$.

5.2.2.4 Design – Coupling Ratio Analysis

The coupling ratio η_i is defined as the ratio between r_i and r_{cbl}, as discussed in section 5.1.1. This section will analyze the influence of the coupling ratios on loading profiles by varying MDP dimensions while maintaining a constant link circular routing curvature r_{cbl} = 25 mm using a 0.2 sec tail curvature time span. Table 5.2 presents the design parameters of two case studies for various coupling ratios. Case 1 represents the scenario where MDP dimensions are scaled by a factor of 2 in comparison to dimensions used in section 5.2.2.1 and Case 2 represents the scaled, inverted scenario where the largest coupling ratios are connected to links adjacent to the actuation unit and decrease in progression to the tip of the tail (link 5).

Figure 5.9 shows the loading profile for the two case studies. By comparing peak values and with those from Fig. 5.5, the scaled coupling ratios in Case 1 have nonlinearly increased loading profiles. The x- and z-component loading increased by a factor of approximately 1.8 whereas y-component loading by a factor of 3.4. This nonlinear increase is expected due to the differentiation of trigonometric terms that are a function of link orientation given by Eq. 5.1 that yield accelerations multiplied by η_i^2. It is interesting to note that the inverted scenario Case 2, generates larger loading profiles than Case 1 since the higher coupling ratios of the tail bottom links correspond to a greater tail rotation and accelerations of the top links, thus producing larger dynamic loading. Greater tail rotations also correspond to a larger moment arm that produce a larger steady state gravitational moment about the z-axis.

Table 5.2: Design parameters used for coupling ratio analysis.

Case	r_{1-5} (mm)	η_{1-5}
1	[18, 32, 44, 56, 68]	[0.7, 1.2, 1.7, 2.2, 2.7]
2	[68, 56, 44, 32, 18]	[2.7, 2.2, 1.7, 1.2, 0.7]
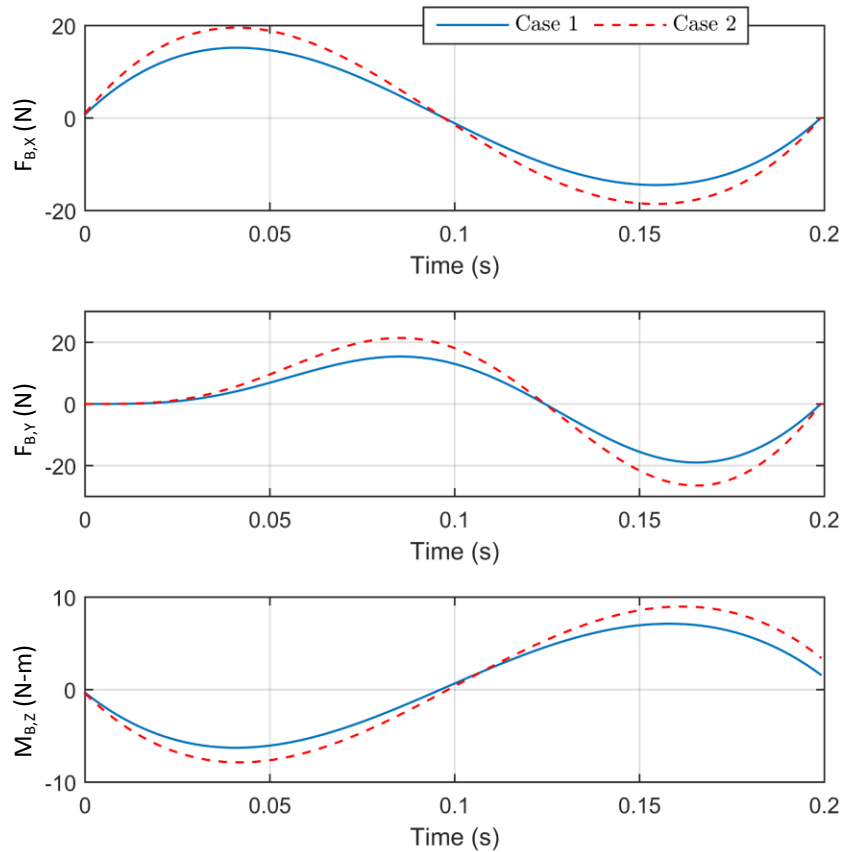
Figure 5.9: Coupling ratio analysis: computed force and moment loading profiles.

5.3 Experimental Prototype and Model Validation

In this section, experiments are performed using a five-link DMST prototype, section 5.3.1, to measure the mechanism's ability to generate loading at its base, section 5.3.2, and validate forward kinematic relations to determine the mechanism's accuracy and repeatability, section 5.3.3.

5.3.1 Tail Implementation

Figure 5.10 shows the experimental test platform under consideration. The prototype's structural components were printed from ABS plastic. High torque servo motors rated for a stall torque of 10 N-m and no load speed of 55 rpm operated at an input voltage of 14 V drive the mechanism's two DOFs with PID parameters set to $K_p = 60$, $K_i = 10$, and $K_d = 0.4$ to demonstrate critically damped behavior. Link lengths and pulley diameters were chosen to be $L_{J2J} = 60$ mm $r_{cbl} = 25$ mm,

and r_i = [9, 16, 22, 28, 34] mm for *i* ranging from 1 to 5 based on optimization scheme to produce a desired tail curvature [16]. These design parameters match the simulation parameters presented in Table 5.1 for comparison of results.
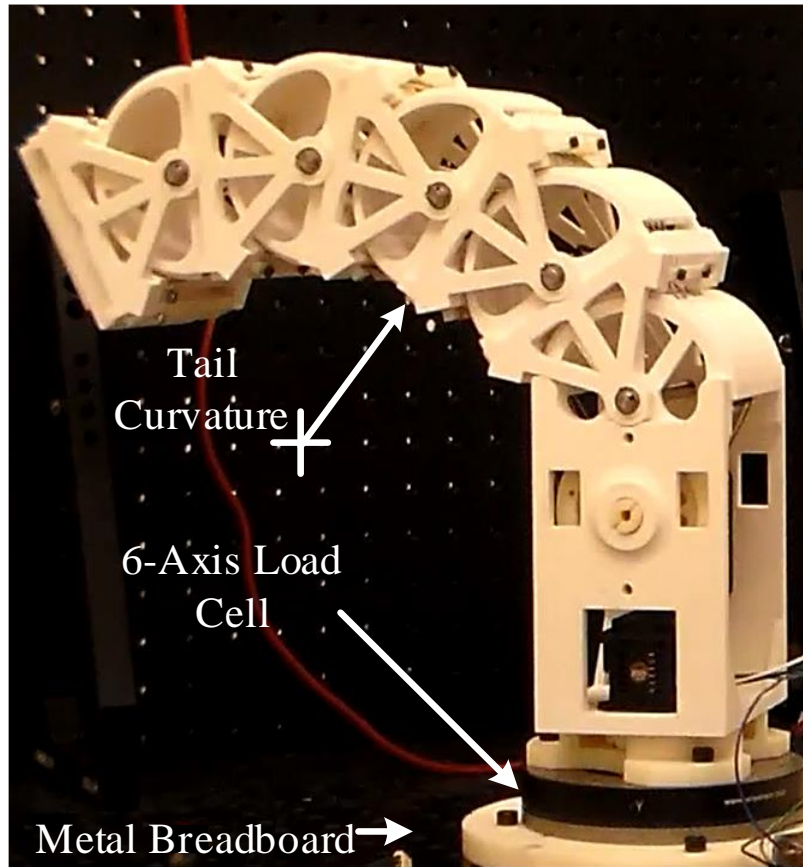
Figure 5.10: Experimental setup of a five-link DMST prototype.

5.3.2 Loading Results

In order to measure the generated loading profiles and verify the dynamic tail loading model presented in section 5.1.4, the five-link DMST prototype was connected to a six-axis load cell to measure the loading profiles generated by the tail, as shown in Figure 5.11. Sensor measurements were sampled at 400 Hz using a PCI data acquisition card. A moving window mean of 50 sample points was used to smooth the measured data.

In this experiment, the tail performed a tail curvature by sending a $\vartheta_m = \pi/2$ rad goal angle at maximum angular velocity and torque to the servo motor controlling the MDP rotation. Loading

profiles were measured for constant roll angles of $\pi/4$, $\pi/2$ and $3\pi/4$ rad, similar to the case scenarios shown in Fig. 5.6.

Figure 5.11 illustrates the measured loading profiles for various roll angles. From the plot, it can be observed that tail curvature motion is completed in 0.24 s, after which the tail experiences vibrations that dissipate to steady state conditions. It is expected that friction within the mechanism extended the response time above the 0.2 s obtained from simulated results that assumed no cable friction $\mu = 0$. In comparison to computed results shown in Fig. 5.6, the measured loading profiles do exhibit similar distributed loads as the roll angle is varied: 1) y-component moment loading maintains a zero value for the three case scenarios, 2) y-component force loading is approximately invariant to roll, 3) x-component force and z-component moment profiles, for $\phi = \pi/4$ and $3\pi/4$ rad, are approximately equal and opposite, whereas the x-component moment and z-component force are approximately equal in magnitude, 4) steady-state gravitational moment offsets closely match computed results, 5) the profiles qualitatively match the shape of computed profiles but do not exactly match the smooth contours due to vibrations in the long structure during tail motions that have not been modeled analytically.

Measured peak loading profile values, equal to 6 N and 1.8 N-m, fall below computed values because the experimental tail motion duration was slightly longer than the 0.2 s time span used in computed results. This is expected since as the time spans of tail motions are lengthened, dynamic loadings decrease towards steady state gravitational loading conditions as explained in section 5.2.2.1. The results of this experiment will be used to update simulation parameters, in particular dissipative friction, to better compute loading profiles as part of future work.
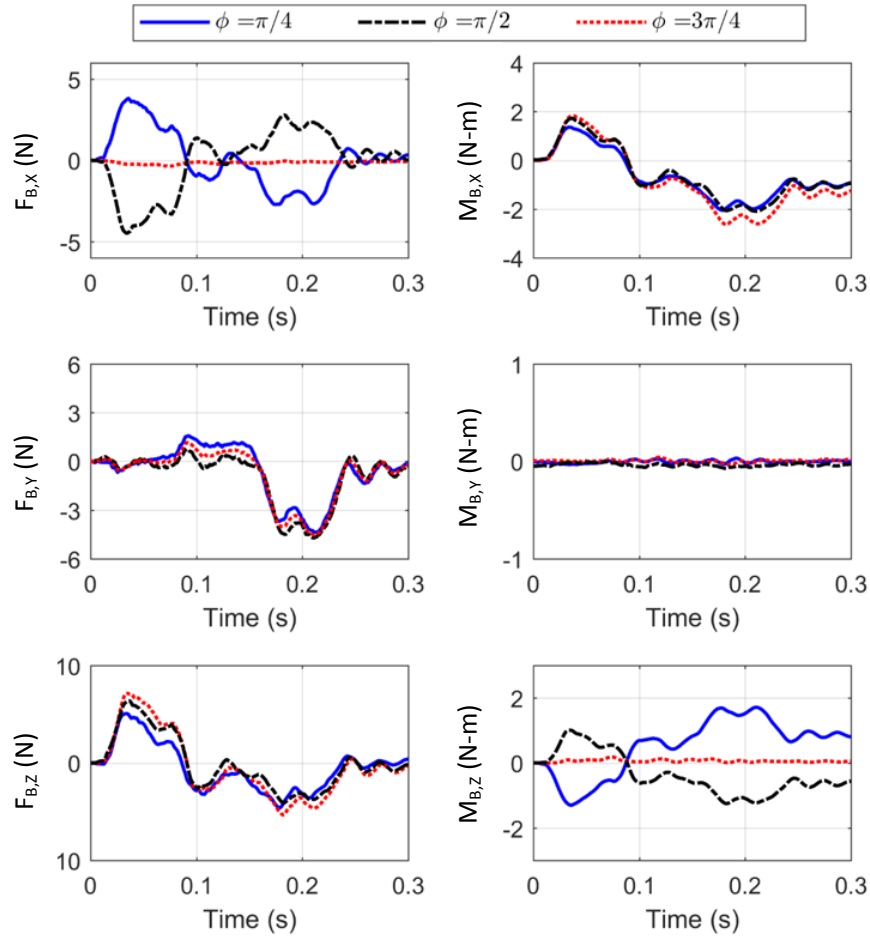
Figure 5.11: Experimentally measured loading profiles for various roll angles.

5.3.3 Accuracy and Repeatability Results

A series of experiments were performed to validate the forward kinematic relations derived in section 5.1.1. The DMST was programmed to perform repeated cycles of three distinct tail curvatures: {C1, C2, C3} where the MDP angle is varied between $\vartheta_m = \pm\{0, \pi/4, \text{and } \pi/2\}$ rad respectively with a fixed roll angle. The tail approached these curvatures in clockwise and counter clockwise sequences to determine if hysteresis due to cable friction and/or elasticity impacted performance. Tail curvatures were recorded using a high-resolution tracking camera mounted orthogonal to the tail curvatures. Image processing techniques were then implemented to measure the link orientations at each configuration. To test the mechanism's accuracy and repeatability, measurements were recorded for ten consecutive cycles. Table 5.3 presents the mean measured

global orientation ($\bar{\vartheta}_i$) and standard deviations ($\bar{\sigma}$) of the measured data and provides a comparison with link orientations computed using forward kinematics.

Table 5.3: Measured experimental results and computed link orientations.

LINK	MEASURED ORIENTATION CLOCKWISE SEQUENCE $-\bar{\vartheta}_i \pm \bar{\sigma}\,°$			COMPUTED ORIENTATION $\pm\bar{\vartheta}_i\,°$			MEASURED ORIENTATION COUNTER-CLOCKWISE SEQUENCE $+\bar{\vartheta}_i \pm \bar{\sigma}\,°$		
	C1	C2	C3	C1	C2	C3	C1	C2	C3
1	0.4±0.1	11±0.3	22.2±0.2	0	10	20.1	0.5±0.6	10.4±0.3	22.2±0.4
2	0±0	16.5±0.5	33.1±0.6	0	16.5	33	0.4±0.5	15.9±0.5	34.4±0.1
3	-1.2±0.5	22.7±0.6	46.4±0.5	0	22.5	45	0.1±0.2	20.8±0.3	45.5±0.3
4	-1.2±0.2	28.3±0.4	59.3±0.3	0	28.4	56.9	1.6±0.8	28.5±0.3	59.2±0.5
5	0±0	33.8±0.7	70.4±0.3	0	34.4	68.9	0.5±0.4	31.2±0.2	67.3±0.4

From the Table 5.3 C1 measured orientations, it is observed that slight offsets are present at the home configuration. Although the tensioning procedure was performed, kinematic coupling creates difficulties in achieving a perfectly aligned home configuration since tensioning of one cable induces slight orientation changes in the remaining links. In addition, it was observed that a slight slack on one side of the cables, terminated at an identical link, is necessary to prevent the mechanism from locking up during operation. Lock ups result from highly tensioned cables for a link that prevent rotation in either direction. The counter-clockwise sequences fall on average -0.3° below clockwise sequences. This result is expected because the steel braided cables used on the prototype are nylon coated and exhibit minimal friction and elasticity therefore the effects of hysteresis were unobservable from the data presented in Table 5.3. From the measured standard deviation data, the maximum repeatability of the mechanism ranged between ±0.8° for each link. Overall, measured angular orientations indicate close correlation with respect to computed orientations. On average, links 4 and 5 showed the largest deviations from computed orientations ranging from to 2.3-3.1°, due to the accumulation of error along the serial structure.

5.4 Conclusion

This chapter presented the kinematic and dynamic modeling of the DMST along with experimental results to validate models, test the mechanisms accuracy and repeatability for static stabilization

applications and the performance in generating inertial loading for dynamic inertial adjustment applications.

Workspace analysis determined that the DMST end effector workspace is capable of spanning 90°, falling much shorter than the end effector workspace of the R3-RT (section 4.2.1), that can span up to 270°, due to its less articulated DOFs. For the DMST, the COM workspace with no added tip-mass, illustrated with a green line in Fig. 5.4, can be displaced along the x-axis up to 100 mm. With the addition of a tip mass with $m_5 = 3.5$ kg, illustrated with a red line, the COM workspace is increased and can be displaced 280 mm along the x-axis. As will be demonstrated in Chapter 8, the DMST requires this additional tip mass to successfully stabilize the biped to position the system's combined COM within the support polygon during a walking gait. Results of kinematic workspace analysis have demonstrated that the DMST produces a lesser dimensionality end effector and COM workspace in comparison to the R3-RT, presented in Chapter 4, due to less articulation and its ability to form one tail curvature. However, higher dimensional workspaces are achievable for multiple DMST modules connected in series, a concept presented in section 3.4 but not practically implemented as part of this research. These results further emphasize the importance of increased articulation and multi-curvature tail configuration shapes that can produce a higher dimensionality end effector workspace and a greater ability to adjust its COM which is important for both dynamic inertial adjustment and static stabilization applications, as discussed in section 4.2.1.

A dynamic loading model was derived to analyze the loading generated by the tail in response to variations in trajectory and design parameters. Dynamic force loading analysis concluded that force loading profiles can be distributed about three axes by varying roll angle and magnified by: (1) reducing the time span of tail motions, (2) allocating a larger mass distribution at the tip of the tail while considering spool torque requirements to produce tail curvature, and (3) increasing coupling ratios of bottom segments adjacent to the tail base. Experimental results were used to validate the dynamic loading model. Experimentally measured peak loading profile values, equal to 6 N and 1.8 N-m, fall below computed values using the dynamic loading model because the experimental tail motion duration was slightly longer than the 0.2 s time span used in computed results. This is expected since as the time spans of tail motions are lengthened, dynamic loadings decrease towards steady state gravitational loading conditions.

Experimental results indicate that the DMST exhibits satisfactory accuracy and repeatability measured to be 3.1±0.8°. These results show better accuracy and repeatability in comparison to the R3-RT that can be attributed to the use of nylon coated steel braided wire with swaged ball bearing ends as described in section 3.4; while the R3-RT utilizes nylon braided cables that are secured at its ends using a screw and nut mechanism.

CHAPTER 6: REDUCED DEGREE-OF-FREEDOM LEGGED ROBOTIC PLATFORMS

This chapter presents the design and analysis of a reduced-DOF Robotic Modular Leg (RML) mechanism used to construct a quadrupedal and bipedal experimental platform to test the performance enhancement capabilities articulated tails can provide that will be demonstrated in subsequent chapters. A review of existing reduced-DOF legs is presented. However, the majority of proposed mechanisms utilize point of contact feet; this create difficulties in producing stable walking gaits for legged robots. Therefore, necessary walking criteria is established that the proposed legged robotic platforms must satisfy that include capabilities to produce a stable forward walking and turning gait while maintaining a constant body height and orientation. Based on this criteria, the RML is proposed that can produce trajectories of a flat foot without the use of an actuated ankle using mechanism kinematics. However, since the RML is a planar leg mechanism, the resultant quadrupedal experimental platform cannot maneuver or stabilize itself; thus, justifying the use of an attached R3-RT mechanism to enable these functionalities. The bipedal experimental platform cannot satisfy any of the aforementioned walking criteria; thus, justifying the use of an attached DMST mechanism to enable these functionalities. These performance enhancement capabilities enabled via the articulated tails as will be further demonstrated in Chapter 8.

6.1 Introduction and Related Work

In recent years, there has been a surge of research conducted in the field of multi-legged robotics due to the high adaptability of legged locomotion on unstructured terrain [83-86]. Conventional multi-legged robotic designs consist of a large number of active DOFs that enhance locomotion and tasking abilities; however, this increases the robots weight, energy consumption and increases the difficulty of trajectory planning and control [87, 88]. It is hypothesized that by using an articulated tail mechanism (presented in Chapter 3) to aid in tasks involving stabilization and maneuvering onboard a legged robots, the burden on the robot's legs to simultaneously maneuver

and stabilize the robot may be reduced. This could allow for simplification of the leg's control algorithms and design; therefore, making them of more practical use.

The majority of multi-legged robots are bio-inspired from animals that have evolved over the years to adapt to their natural habitats. These robots typically utilize 3-DOF leg mechanisms to arbitrarily position their single point of contact feet to perform forward walking gaits and steer on both flat and uneven terrain. Therefore, a $2n_{pair}$ legged robot requires $6n_{pair}$ actuators where n_{pair} is the number of leg pairs [89]. If flat feet are to be implemented into leg mechanism to enhance stability and disturbance rejection capabilities [90], additional DOFs are required to control foot orientation during a walking gait.

To address these challenges, researchers have investigated methods to reduce the number of actuated joints in multi-legged robotic systems. Torige et al. [91] developed a six-segment centipede-like walking robot, Fig. 6.1(A), with four motors per segment. In this design, point contact was sufficient to provide a stable support polygon since at least three feet were in contact with the ground during the demonstrated walking gait. Therefore, a $2n_{pair}$ legged robot utilized $4n_{pair}$ active joints. Similarly, Hoffman et al. [92] designed a micro-scale centipede robot, Fig. 6.1(B), with passive revolute joints located between repeated two-legged segments. For each segment, the two legs were passively coupled to two linear actuators that provide opposing moments about COM, causing the body to extend, raise the legs and propel robot forward. In this design, the $2n_{pair}$ legged robot utilized $2n_{pair}$ active joints. The RHex hexapod robot, a six legged robot Fig. 6.1(C), was designed with six actuated DOFs that continuously rotate compliant C-shaped legs that propel the robot forward with steering provided by differential drive [93]. A similar design concept utilizing continuous rotation legs was implemented on a centipede robot with an additional active DOF incorporated between body segments [94]. Yoenda et al. [95] designed a quadruped robot with four active DOF, Fig. 6.1(D). The quadruped robot, capable of performing a creeping gait, was separated into front and rear sections connected using an active revolute joint capable of rolling in the horizontal direction. The roll of the body coupled with rotation of U-shaped front and rear legs with point contact feet caused the robot to move forward. There has also been considerable amounts of research in one-DOF crank-driven mechanisms [96-100], two-DOF leg designs [101, 102] that approximate straight line foot paths similar to the Jansen mechanism path curve, and passive dynamic walkers [103] that utilize less control and energy in comparison to powered robots, some of which are shown in Fig. 6.1(E-J).
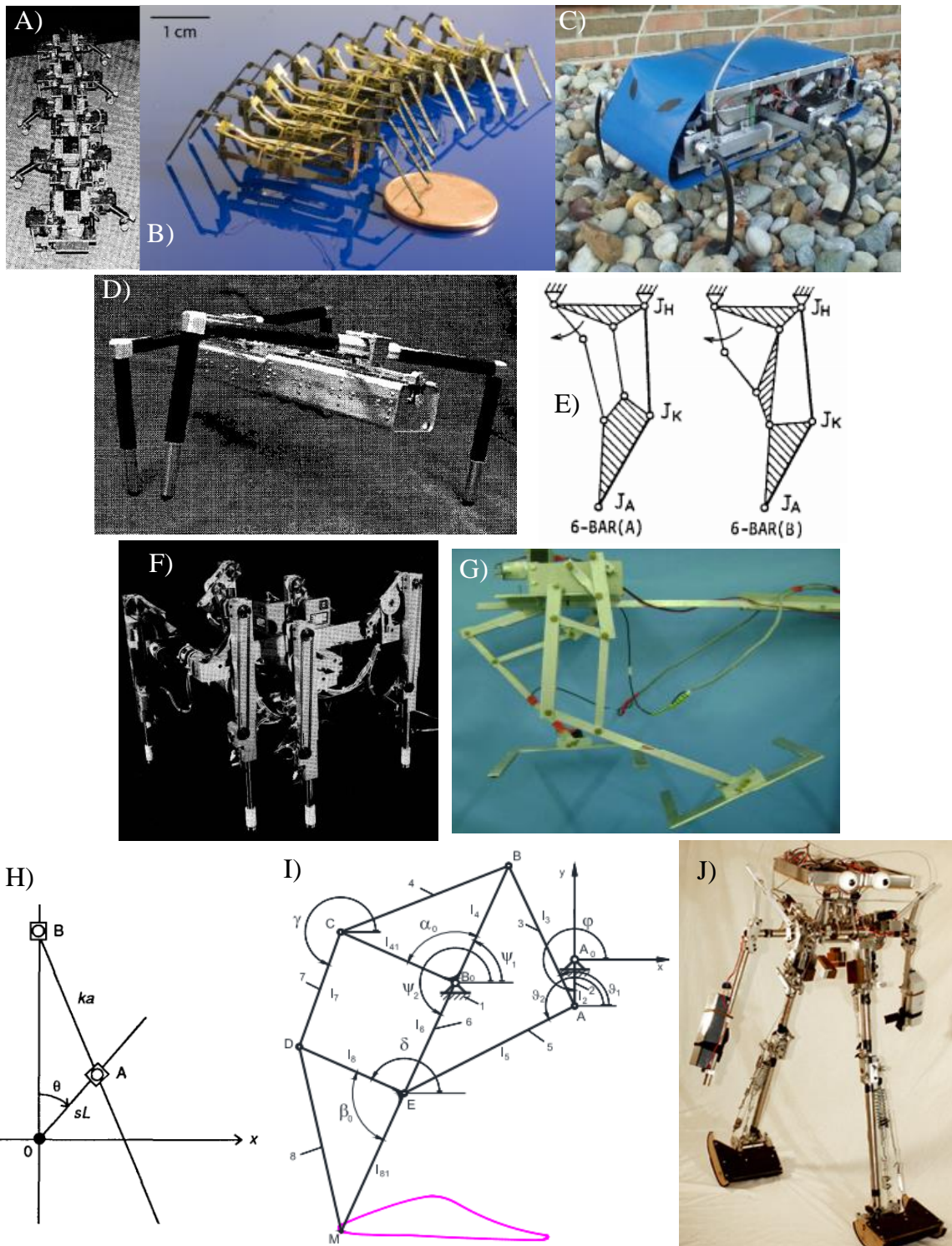
Figure 6.1: Proposed reduced DOF leg designs. A) Centipede Walking Robot [91], B) Centepede-inspired Millirobot [92], C) Rhex [93], D) Reduced DOF Quadruped [95], E) 6-Bar Ankle Generators [96], F) Melwalk-III [97], G) Pantograph Biped [98], H) 2-DOF Leg Mechanism [101], I) Jansen Mechanism [102] and J) Passive Walker Biped [103].

6.2 Necessary Walking Functions for Legged Robots

Although reduced-DOF leg mechanisms reviewed in the previous section do enable the construction of legged robots with reduced design and control complexity; however, the reduced articulation may hinders the robot's performance. For instance, the Rhex [93] and Reduced DOF Quadruped [95] are capable of walking forward, but the robots body height and orientation fluctuates during a walking gait. Such characteristics are undesirable since they may induce instances of instability during tail motions and should be accounted for as part of this research. Furthermore, the majority of existing leg mechanisms utilize point of contact feet that create difficulties in producing stable walking gaits. Therefore, we utilize the five walking ability criteria, presented in [104], to design and assess a legged robots' performance proposed as part of this work. These criteria are listed below as:

1) Maintain quasi-static stability during a waiting gait

2) Maintain a constant robot body height during a waiting gait

3) Maintain horizontal body orientation during a walking gait

4) Have the ability to move backward, forward

5) Have the ability to steer

Criteria (1) and (2) are required to maintain a stable robotic platform in static configurations and during a walking gait, in addition to improving the energy efficiency of the system since the legs will not be required to raise and lower the body cyclically. Criterion (3) ensures a sufficient COM margin of stability within the support polygon defined as the convex hull of the robot's feet in contact with the ground. Criterion (4) and (5) ensure the sufficient amount of locomotion capabilities to enable the robot can be steered in any desired position and direction.

6.3 Robotic Modular Leg Design

This section presents the mechanical design of the RML. Figure 6.2 shows a side view of the RML. The RML is a two-DOF mechanism composed of two serially-connected four-bar mechanisms

analogous to a thigh and shin. The thigh rotates at the hip joints, and the shin rotates at the knee joints. The two four-bar mechanism dimensions are designed to be parallelograms, which results in double-rocker behavior. Therefore, the knee and foot links remain parallel to the body as the thigh and shin links move. This method kinematically maintains a flat foot orientation without the use of an additional actuator at the ankle. On flat surfaces, planar feet provide a more stable support polygon in comparison to feet with a single point or line contact [90].

As seen in Fig. 6.2, the thigh is actuated directly by a hip motor mounted within the body link, while the shin is actuated by a thigh mounted motor. A timing belt system transmits the thigh mounted motor actuation to the shin link at the knee joint. This motor configuration controls the relative motion of these links without the need for input compensation for the hip motor. In addition, this also allows both motors to be placed in the vicinity of the body, thereby minimizing leg inertia. The utilization of two four-bar mechanisms and a timing belt system classifies the RML as a single DOF coupled serial chain mechanism that takes advantage of the mechanical constraints between articulations to guide end effector (foot) motions [105].

Although planar feet perform well on flat terrain, the foot should be capable of traversing uneven terrain as well. A passive suspension system, inspired by the active locking foot mechanism in [106], is integrated into the foot that permits vertical translation of four toes. Compression springs between the foot and each toe provide compliance that softens impact and maintains a stable support polygon with four points of contact, even in the presence of uneven terrain. Shock absorbent gel pads are placed at the end of each toe to further improve compliance and contact surface area. A linear pattern of retaining ring groves is incorporated into the toes to allow modification of each spring's pre-compression.

Linear potentiometers measure the displacement of each toe. Knowing the spring's stiffness, this sensory feedback can be used to determine the foot's contact forces with the ground and calculate the zero-moment-point stability criteria of the legged robot [107]. The passive suspension system enables the RML to walk on uneven terrain.
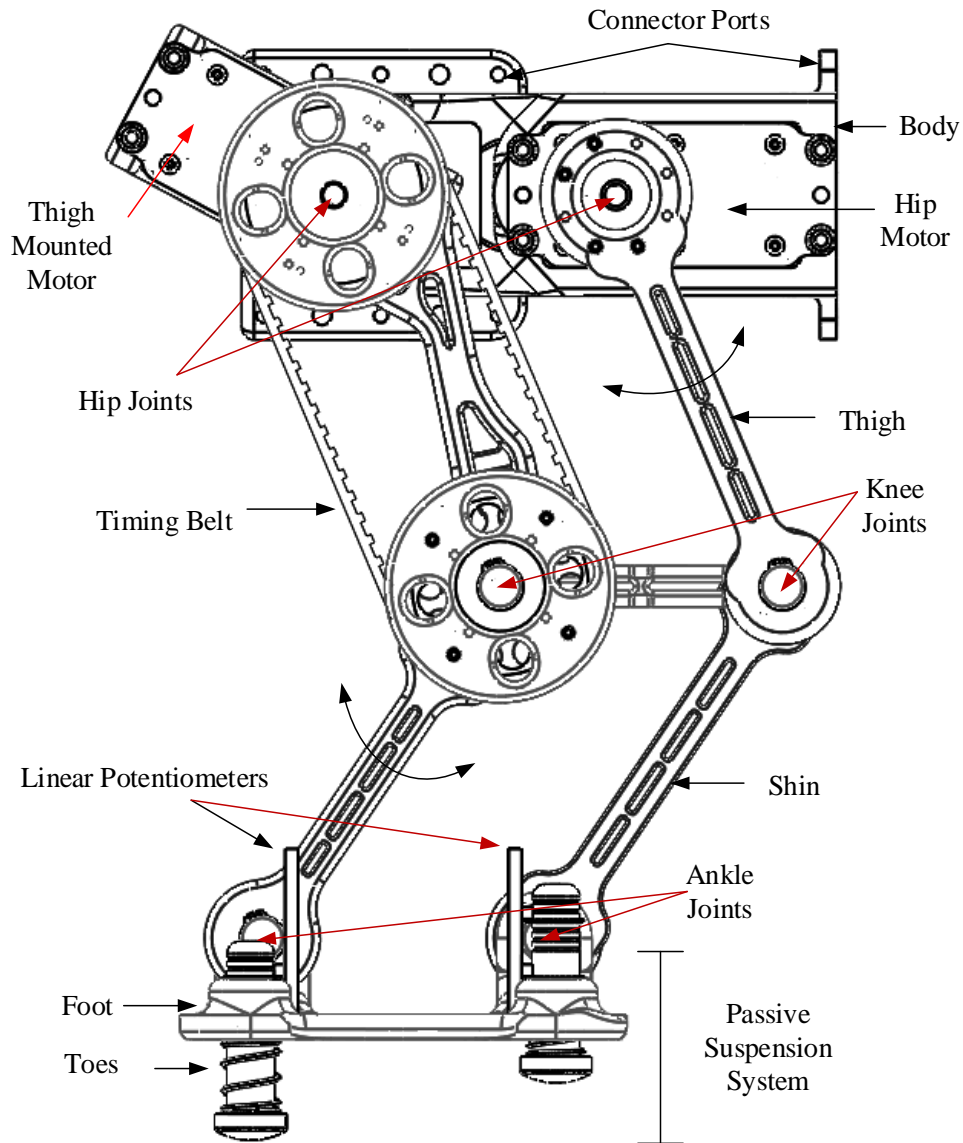
Figure 6.2: Side view schematic diagram of the RML mechanism.

6.3.1 Multi-Legged Robotic Platform- Quadruped and Biped Configurations

Design symmetry of the structural components of the RML enable the construction of multi-legged robots by interconnecting identical modules via its connector ports, Fig. 6.2. Figure 6.3 shows an isometric view of a quadruped configuration that is constructed from four RMLs. Extension units have been used to modify the overall length of the robotic system. A biped configuration can also be constructed by connecting two RMLs. However, since the RML is a planar leg mechanism the resultant legged robots shown in Fig. 6.3 cannot satisfy all of the mentioned walking criteria in

section 6.2. The quadruped configuration cannot maneuver or stabilize itself; thus, justifying the use of an attached R3-RT mechanism to enable these functionalities. The biped configuration cannot satisfy any of the aforementioned walking criteria; thus, justifying the use of an attached DMST mechanism to enable these functionalities. These performance enhancement capabilities enabled via the articulated tails will be investigated in Chapter 8.
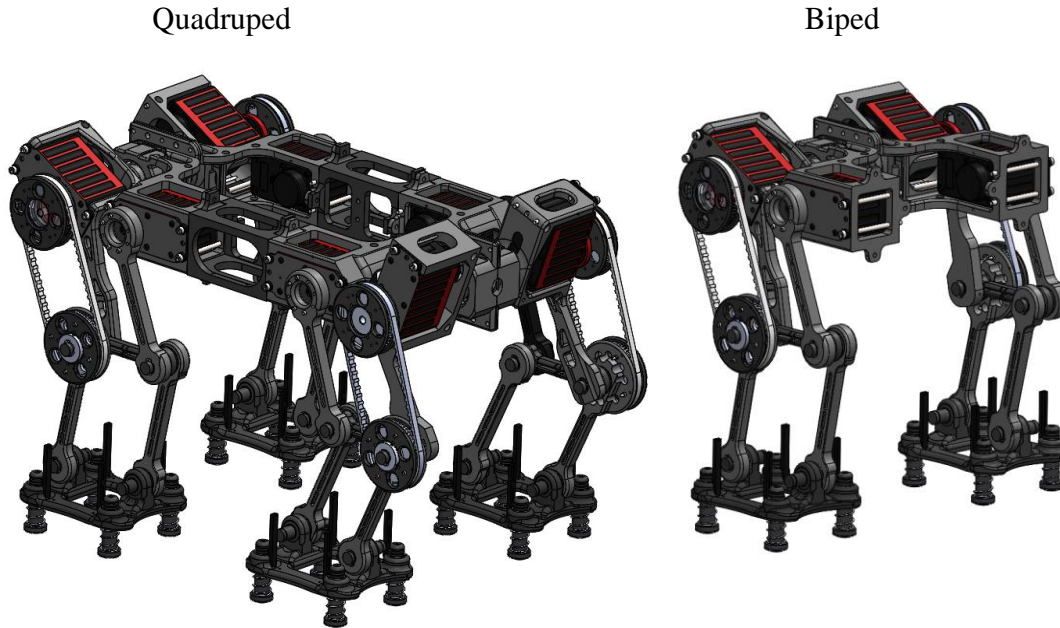
Quadruped   Biped

Figure 6.3: Isometric view of the quadruped and biped configurations constructed from 4 and 2 RML's respectively.

6.4 Single Leg Kinematics

The parallelogram structure of the RML discussed in section 6.3 allows for simplification of the single-leg kinematics model into a planar elbow manipulator [108]. The leg schematic shown in Fig. 6.4(A) defines the kinematic model parameters, including the hip length l_H, shin length l_S knee length l_K, and the position vector from the hip frame to the foot frame $\boldsymbol{p}_{HF}$. The forward kinematics of the leg are defined in Eq. 6.1 with respect to the hip frame coordinate system, for a hip angle of θ_H and shin angle of θ_S. Given the planar topology of the leg, the y-coordinates of each body remain constant.

$$\begin{cases} l_H \cos(\theta_H) + l_S \cos(\theta_H + \theta_S) = p_{HF,x} \\ -l_H \sin(\theta_H) - l_S \sin(\theta_H + \theta_S) = p_{HF,z} \end{cases} \qquad (6.1)$$

For a prescribed p_{HF} in the leg workspace, the leg's inverse kinematics are analytically calculable; within the workspace boundaries, two solutions can be found for a given p_{HF} (knee forward and knee behind), and on the workspace boundaries, one solution can be found.

The forward velocity kinematics are found by differentiating Eq. 6.1, as shown in Eq. 6.2. Joint angle velocities are calculable from prescribed $\dot{p}_{HF}$ when $\sin \theta_S$ (the Jacobian determinant) is not equal to zero.

$$\begin{bmatrix} -l_H \left(\sin(\theta_H) + \sin(\theta_H + \theta_S)\right) & -l_H \sin(\theta_H + \theta_S) \\ -l_S \left(\cos(\theta_H) + \cos(\theta_H + \theta_S)\right) & -l_S \cos(\theta_H + \theta_S) \end{bmatrix} \begin{bmatrix} \dot{\theta}_H \\ \dot{\theta}_S \end{bmatrix} = \begin{bmatrix} \dot{p}_{HF,x} \\ \dot{p}_{HF,z} \end{bmatrix} \qquad (6.2)$$
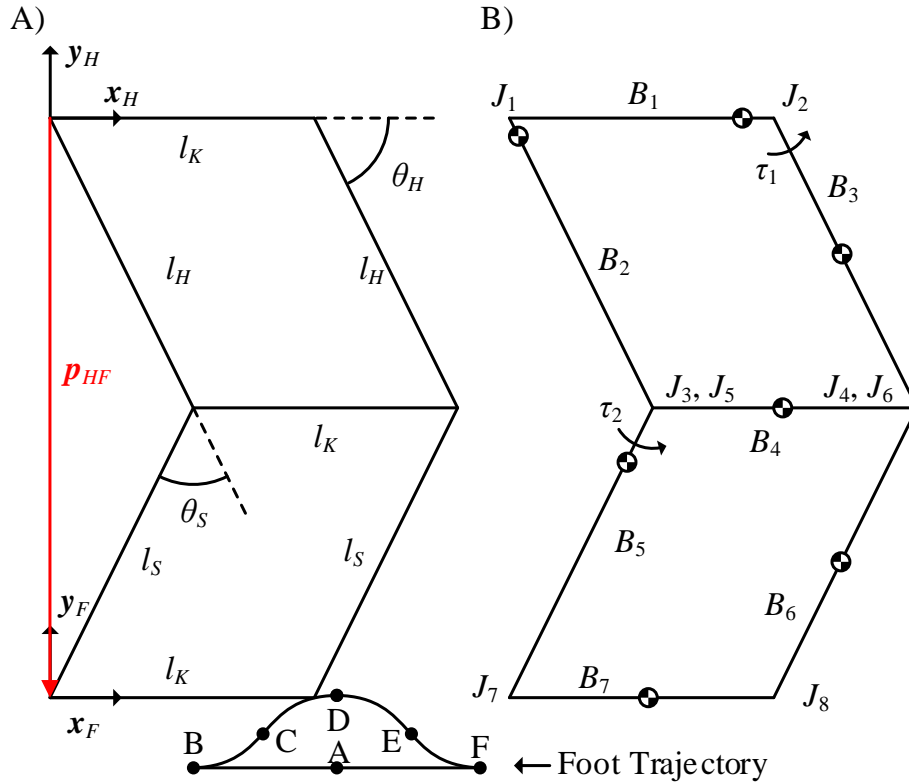
Figure 6.4: Single-leg model: A) kinematic variables, and B) dynamic variables.

6.5 Single Leg Dynamics

Unlike the single-leg kinematics, the single-leg dynamics cannot be generalized by a serial robotic structure; a model representing the double-four-bar structure is needed to extract the joint requirements to drive the thigh and shin linkages given the gravitational loading on each link, as well as the external loading applied on the leg from the hip/foot.

Given the closed-loop kinematic structure of the thigh and shin, spatial generalized coordinates are used to calculate the leg dynamics [109]. For each of the 7 bodies shown in Fig. 6.4(B) labeled as B_{1-7}, 7 coordinates are defined—3 Cartesian coordinates and 4 Euler parameters—which creates a joint space of 49 variables. Forty-nine constraint equations are required to ensure this model is well posed; the constraints utilized are described in Table 6.1.

Table 6.1: Dynamic model constraints

Constraint	Qty.	Eqs. Per Constraint	Total
Fixed	1	6	6
Revolute-5	6	5	30
Revolute-2	2	2	4
Angle Driver	2	1	2
Normality	7	1	7
Number of Constraint Equations			49

The fixed constraint rigidly connects either the hip (B_1) or foot (B_7) to ground and does not allow for relative linear or angular displacement. The revolute joint constraints, located at joints J_{1-8} as shown in Fig. 6.4(B), prescribe two points on two bodies to coincide and allow relative rotation about a shared axis. Because the linkages are topologically planar (i.e., the four revolute joint axes in each four-bar are parallel), for each parallelogram, one of the four revolute joints must be reduced DOF to avoid over constraining the model—after specifying the three 5-equation revolute joints, only the x- and y-coordinates of the final joint need to be prescribed as coinciding, hence the 2-equation revolute joint constraints. The angle driver constraint prescribes the relative angle between two bodies connected by a revolute joint. The normality constraint ensures the norm of each body's set of four Euler parameters remains 1, allowing these four coordinates to represent a generalized spatial rotation.

Equation 6.3 defines the dynamic model in terms of the 21 Cartesian coordinate accelerations $\ddot{\mathbf{p}}$, the 28 Euler parameter accelerations $\ddot{\mathbf{e}}$, and the 49 Lagrange multipliers λ, where $\boldsymbol{M_M}$ is a block diagonal matrix of the link mass tensors, $\boldsymbol{J}$ is a block diagonal matrix of the link inertia tensors, $\boldsymbol{\Phi_p}$ and $\boldsymbol{\Phi_e}$ are Jacobians of the constraint vector $\boldsymbol{\Phi}$ with respect to the Cartesian coordinates ($\boldsymbol{\Phi_p}$) and Euler parameters ($\boldsymbol{\Phi_e}$), $\mathbf{F}$ and $\mathbf{n}$ are forcing functions associated with the external forces, external moments acting on each body, and $\boldsymbol{\gamma}$ are the acceleration-independent terms associated with twice differentiating the constraint vector $\boldsymbol{\Phi}$ [109].

$$
\begin{bmatrix} \boldsymbol{M_M} & \boldsymbol{0} & \boldsymbol{\Phi_p^T} \\ \boldsymbol{0} & \boldsymbol{J} & \boldsymbol{\Phi_e^T} \\ \boldsymbol{\Phi_p} & \boldsymbol{\Phi_e} & \boldsymbol{0} \end{bmatrix} \begin{bmatrix} \ddot{\mathbf{p}} \\ \ddot{\mathbf{e}} \\ \lambda \end{bmatrix} = \begin{bmatrix} \mathbf{F} \\ \mathbf{n} \\ -\boldsymbol{\gamma} \end{bmatrix} \tag{6.3}
$$

The Lagrange multipliers λ correspond to the forces and moments required to maintain the various constraints. The Lagrange multipliers associated with the two angle driver constraints correspond to the torque required to actuate those joints. Other Lagrange multipliers may be utilized to estimate the force loading transmitted through various leg lengths.

6.6 Gait Planning

This section details how foot trajectories are generated (section 6.6.1) and sequenced (section 6.6.2) to produce the walking gaits that the virtual quadruped and biped configurations will utilize in simulations as demonstrated in Chapter 8.

6.6.1 Foot Trajectory

In this section, the set of walking functions defined in section 6.2 are used to design a foot trajectory to maintain a stable, constant body height and forward velocity with respect to the ground with minimal ground impact loading. Trajectory planning involves the process of generating foot trajectories in space relative to the fixed body coordinate frame.

Figure 6.4(A) shows a complete single-cycle foot trajectory that consists of two main phases: swing and support phase represented by segments B-C-D-E-F and F-A-B respectively. The swing phase advances the foot forward while the support phase supports the robot at the ground and propels the robot body forward. Point B and F are takeoff and landing points for the foot.

In order to achieve criteria (2) and (3), defined in section 6.2, for flat-terrain walking, it is required to have a straight line support phase, with respect to the body coordinate frame that is free of vertical translation of the passive suspension system fingers and impulsive forces at takeoff and landing instances. Vertical translation of the fingers will cause changes in body height and impulsive forces transmitted to the body will cause the body to deviate from its horizontal configuration. To prevent vertical finger translation, spring pre-compressions will be adjusted such that the summation of spring forces equal the weight of a single RML mechanism. Therefore, the robot body height will remain constant while walking since the suspension system will only dissipate energy in the presence of impulsive loading. To minimize impulsive forces, foot trajectories require zero vertical velocity and acceleration at takeoff and landing instances while the robot height is held constant.

Quintic polynomials were used to generate vertical foot position/velocity/acceleration trajectories. Boundary conditions include the start and end step heights, and zero velocity/acceleration at the start and end points. A linear equation was used to generate the trajectory for the straight line support phase. A vector of uniformly-spaced horizontal position points (providing a constant horizontal foot velocity) was used with the vertical foot trajectory to control the swing phase [19]. Joint angle trajectories were then computed using the kinematic model in section 6.4.

6.6.2 Forward Walking

For forward walking, a trot gait pattern will be utilized. Trot gaits can provide both quadrupeds and bipeds with flat feet a quasi-statically stable walking gait if the projected COM falls within the support polygon [110], satisfying criterion (1). Figure 6.5(A) shows a schematic diagram of the leg numbering, and Fig. 6.5(B, C) shows the gait diagrams for stable trotting for bipeds and quadrupeds. The plot's horizontal axis spans the normalized time for a foot trajectory cycle. The line segment for each leg represents the support phase, from landing (square at segment start) to takeoff (circle at segment end). The quadruped simply alternates between diagonal pairs of legs in contact with the ground; for the biped, a period of dual contact is required to shift the robot COM. For the quadruped, the two support phase feet move cooperatively (i.e., in the same direction). For the biped robot, there is a short time instance during the forward walking gait, as seen in Fig. 6.5(C), where both feet are in contact with the ground to provide the time required to adjust COM

position using an attached tail. Failure to provide this double support phase to the biped robot may induce instances of instability if the tail does not have a sufficient amount of time to adjust the COM position within the single support phase support polygon (as will be demonstrated in Chapter 8).
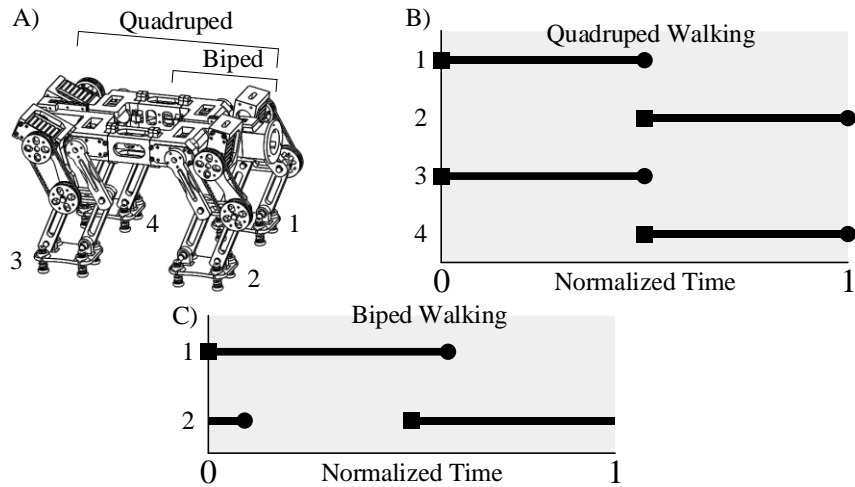
Figure 6.5: Gait diagrams: A) leg numbering, B) quadruped walking, and C) biped walking.

6.7 Results

In this section, results are presented that utilize the leg's dynamic model to analyze the motor actuation requirements (section 6.7.1) and to experimentally validate the leg's kinematic model on an integrated prototype of the RML by studying its performance in tracking a foot trajectory (section 6.7.2).

6.7.1 Estimating Actuation Requirements

After generating a preliminary design for the leg, the kinematics and dynamics models were used to analyze the speed and torque requirements to aid motor selection.

The kinematic and dynamic models presented may be utilized for two types of simulations: fixed-hip and fixed-foot. In the fixed-hip simulation, the body of the legged robot is assumed to be a fixed frame, with the foot lifting from the ground and moving with respect to the hip. In the fixed-foot simulation, the foot maintains contact with the ground while supporting the leg and any external force applied on the hip by the other components of the legged robot.

For the motor speed analysis (kinematic), the results from these two models are equivalent and may be mapped into one another by a kinematic transformation. However, for the torque analysis (dynamic), the fixed-hip and fixed-foot models represent distinct modes of operation for the leg (swing vs. support phases). Due to the need for the leg to support some of the weight of the legged robot during the support phase, the fixed-foot model will be used in this analysis to determine the maximum motor torque requirements.

After generating a preliminary design for the RML, the mass and geometric properties of this design were extracted using CAD software. The relevant properties used in these simulations are summarized in Tables 6.2 and 6.3. With reference to Fig. 6.4(B), the COM coordinates for each body are defined in a body-frame coordinate system centered at joint i with its x-axis defined along the unit vector from joint i (J_i) to joint j (J_j), the z-axis coming out of the page, and the associated y-axis completing the right-handed coordinate system.

Table 6.2: RML geometric properties.

Property	Value	Property	Value
l_K	120.1 mm	l_H, l_S	180 mm

Table 6.3: RML mass properties.

Body	J_i	J_j	Mass (kg)	z-axis Inertia (kg-m^2)	Center-of-Mass (mm)
B_1	J_1	J_2	1.708	0.0132	[109.26, 0, 0]
B_2	J_1	J_3	1.645	0.0081	[-4.64, -11.57, 0]
B_3	J_2	J_4	0.145	0.0009	[102.73, 0, 0]
B_4	J_3	J_4	0.108	0.0004	[56.83, 0, 0]
B_5	J_5	J_7	0.382	0.0020	[39.43, 0, 0]
B_6	J_6	J_8	0.171	0.0011	[90, 0, 0]
B_7	J_7	J_8	0.509	0.0031	[60.15, -31.97, 0]

The foot trajectory described in section 6.6 maintains a constant distance between the hip and foot joints during the straight line support phase. This is analogous to holding the hip trajectory

at a constant height $p_{FH,y} = -p_{HF,y} = 330$ mm relative to the foot joints. In addition, the foot trajectory in section 6.6 moves along a prescribed step length distance during its support phase. For a step length of 150 mm centered with respect to the foot and hip, the hip will move from 75 mm behind the hip joint ($p_{FH,x} = -p_{HF,x} = -75$ mm) to 75 mm before the hip joint ($p_{FH,x} = -p_{HF,x} = 75$ mm) over a prescribed time period T_s at a constant hip velocity speed $150/T_s$ mm/sec.

To mimic the additional loading from the legged robot during the support phase, an external force representing a second leg opposite the leg under consideration is applied to the hip link. To calculate this force and its point of application relative to the hip frame, the total mass of the leg (4.668 kg) along with the center-of-mass position with respect to the hip-fixed frame ([55.71, -71.60, 0] mm) when the each hip joint is directly above its respective foot joint (i.e., when $p_{FH,x} = 0$ mm and $p_{FH,y} = 330$ mm).

Figures 6.6 and 6.7 show the motor speeds and motor torques, respectively, required for support phases traversing the 150 mm step length in $T_s = \{0.5, 1.0, 1.5\}$ sec. The required joint velocity increases nonlinearly as the hip velocity increases, yet the required joint torques maintain similar profiles with different time scaling. This is due to the fact that the external loading acting on the leg does not vary with time. As a result, the mapping of this loading into the joint torques depends only on the instantaneous geometry of the leg at a given time and not the speed at which that geometry changes.
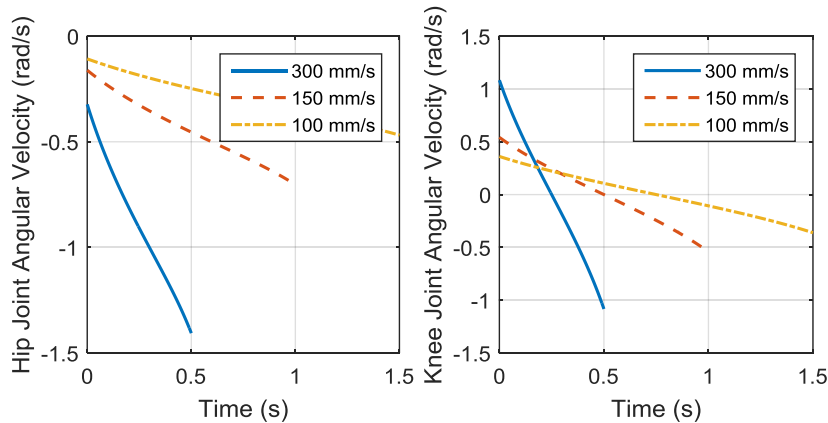
Figure 6.6: Motor speed analysis for varying hip speed.
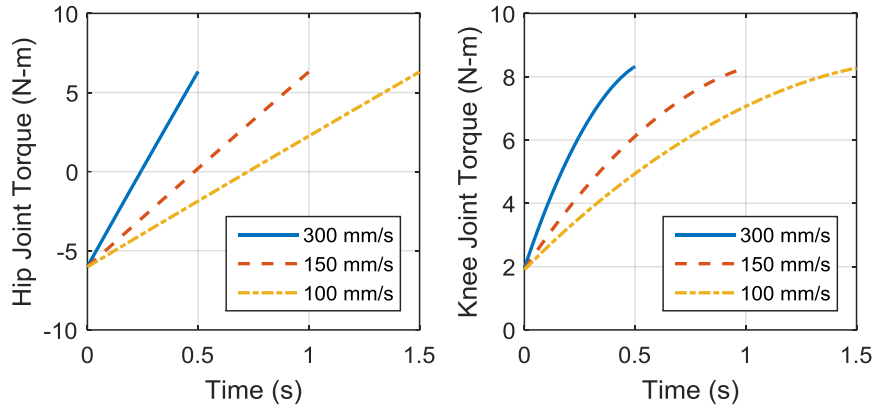
Figure 6.7: Motor torque analysis for varying hip speeds.

The knee angular velocity, shown in Fig. 6.6, changes sign due to the thigh link passing through a vertical configuration in relation to the foot, causing the shin to initially rotate toward the foot in the +z direction, then away from it, as the constant hip height relative to the foot is maintained. In Fig. 6.7, the knee torque is positive throughout each simulation to oppose the links' gravitational loading and the hip's external loading from 'collapsing' the knee. This torque changes over time despite the constant external loading on each rigid body due to the torque's dependence on the leg configuration.

The servomotors selected to actuate the hip and knee joints provide a maximum of 11.3 N-m of torque and 120 deg/sec (2.09 rad/sec) angular velocity. The estimated motor requirements fall within the motor specifications, with margins of 2.98 N-m and 0.68 rad/sec for the motor torque and speed, respectively.

6.7.2 Leg Prototype Tracking Experiment

In this section, experiments are carried out on an integrated prototype shown in Fig. 6.8 to evaluate the performance of the RML in performing walking gaits. Structural components were fabricated using with Acrylonitrile Butadiene Styrene thermoplastic using a 3D printer. The RML prototype's weight is 4.7 kg and measures 368 mm in a fully extended configuration.

A Teensy 3.1 MCU was connected to a computer via a USB-serial port and used to send joint trajectories to the servomotors. To ensure stable response of servo motors, the joint trajectories were sampled at an update rate of 50 Hz using linear interpolation.

A series of experiments were conducted to measure the accuracy and repeatability of the RML in tracking a desired foot trajectory. Analyzing these parameters is critical to measure the mechanism's effectiveness in reproducing a variety of walking gaits, since deviations from desired trajectories may cause undesirable effects. For example, large tracking errors during the support phase may create impulsive forces or swaying of the legged robot body that causes loss of stability and tipping over.

To test the mechanisms accuracy and repeatability, the RML prototype was rigidly grounded to a wall via its connector ports as shown in Fig. 6.8 and programmed to track 10 cycles of a foot trajectory in midair, in both clockwise and counterclockwise directions, with a step height of 50 mm and a step length of 150 mm. A tracking camera was mounted orthogonally to the RML to capture joint angles at key points A, B, C, D, E, and F (Fig. 6.4(A)) during the foot trajectory. This data was then used to compute the mean and standard deviation of measured joint angles. Measured data was then compared with desired joint angles computed from inverse kinematics.
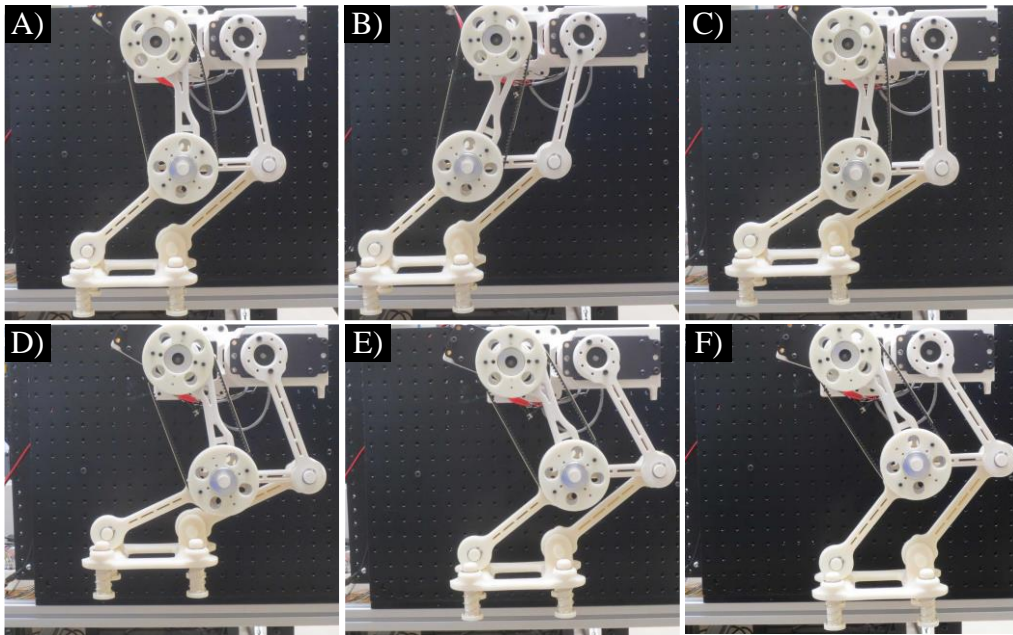
Figure 6.8: Integrated RML prototype tracking a foot trajectory at key points A, B, C, D, E, and F.

Initial experimental results indicated that the RML had two main sources of tracking error: 1) angular offsets at the home configuration measuring $\Delta\theta_H = 1°$ and $\Delta\theta_S = 6°$, and 2) a bi-directional timing belt backlash that caused θ_S to lead the desired trajectory by $2°$ in the positive

direction and lag by -2° in the negative direction. These sources of error were compensated for by calibrating the servo motor home configuration and providing additional angular rotations to account for the bi-directional lead and lag.

The experiments were then repeated after calibration and input compensation. Figure 6.9 presents measured results of joint angle mean and standard deviation at the key points compared with desired joint trajectories. Results indicate that θ_H and θ_S demonstrated an average angular error equivalent to 0.6° and 1.2° respectively and repeatability in the range of ±1.1°. A maximum deviation from the straight line support phase was recorded to be 5.2 mm, a significant improvement from the 20 mm deviations reported in [18].
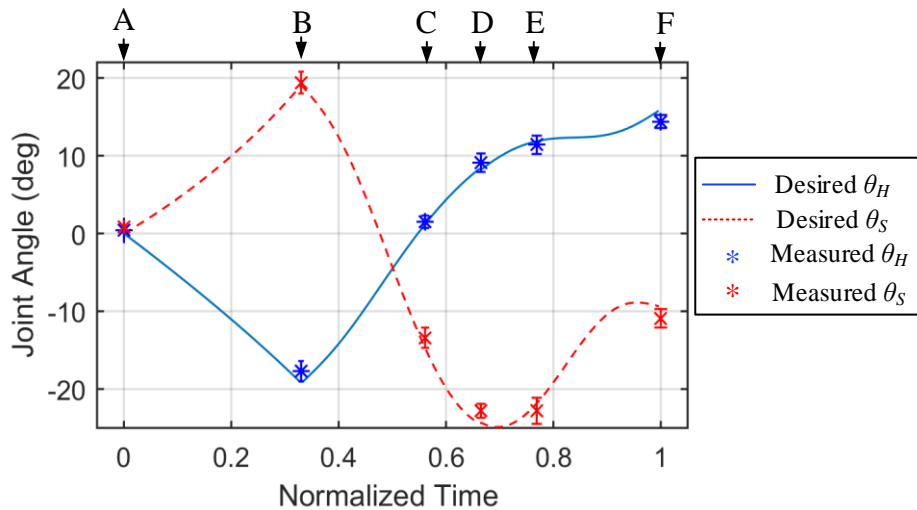
Figure 6.9: Measured results of joint angle mean and standard deviation bars at the key points (A-F) compared with desired joint trajectories.

6.8 Conclusion

This chapter discussed the conventional approach in designing legged robots that utilize leg mechanisms that require a minimum of 3 active DOF per leg to produce walking trajectories. To simplify the design and control of legged robots, researchers have proposed reduced DOF leg mechanisms that require 2 or 1 active DOF to produce walking gaits. However, the reduced articulation hinders the robot's performance. Furthermore, the majority of existing mechanisms utilize point of contact feet; this create difficulties in reproducing stable walking gaits for legged robots.

To match walking performance with respect to conventional legged robots, this chapter presents the necessary walking criteria the proposed reduced DOF legged robotic platforms with attached articulated tails must satisfy that include capabilities to: produce a stable forward walking and turning gait while maintaining a constant body height, and orientation. Based on these criteria, a reduced-DOF leg mechanism called the RML is proposed.

The RML is composed of two serially connected four-bar mechanisms that utilizes kinematic constraints to maintain a parallel orientation between the flat foot and body without the use of an actuated ankle. A passive suspension system integrated into the foot enables the dissipation of impact energy and maintains a stable four point of contact support polygon on both flat and uneven terrain. The modular design enables the construction of reduced-DOF quadruped and biped robots that are used as experimental platforms to test the articulated tails abilities in enhancing maneuverability and stabilization. However, since the RML is a planar leg mechanism, the resultant quadruped configuration cannot maneuver (turn) or stabilize itself and the biped configuration cannot satisfy any of the aforementioned walking criteria; thus, justifying the implementation of articulated tails to augment performance in terms of maneuvering and stabilization as will be further investigated in Chapters 8.

Kinematic and dynamic models were developed to analyze actuation requirements for the leg and aid motor selection for designed walking gait foot trajectories that exhibit straight line support phases to maintain a constant body height above the ground during walking gaits. Experimental results demonstrated the accuracy and repeatability of the mechanism in tracking a foot trajectory. Results indicate that the RML deviates from the straight line support phase by up to 5.2 mm; therefore, making this mechanism feasible for potential implementation to construct legged robot prototypes. However, in this research, only virtual simulations of the legged robots with tail aided maneuvering and stabilization capabilities are evaluated in experiments and simulations as will be demonstrated in Chapter 8.

CHAPTER 7: TAIL-AIDED LEGGED ROBOTIC SYSTEMS: DYNAMIC MODELING, OPTIMIZATION, AND CONTROL

This chapter reviews existing literature on dynamic modeling and control of robotic tails onboard mobile robots for inertial adjustment applications (section 7.1). Based on this review, a dynamic formulation is presented to model a generic robotic system consisting of a legged robot with an attached pendulum-like tail, in contact with the ground, to derive the relations governing the transition between low-speed and high-speed tail motions that induce inertial adjustment, translation and angular rotation, of the legged robot utilizing tail dynamics (section 7.2). This dynamic modeling approach is then extended to an articulated tail, R3-RT, attached to a quadruped robot (section 7.3). However, based on a comparison of estimated frictional forces and moments between the legged robot's feet and ground with respect to the R3-RT's generated inertial force and moment bandwidth (evaluated in Chapter 4), the inertial adjustment approach is modified to enable an airborne jump phase in the quadruped robot gait for tail-aided maneuvering. The proposed dynamic formulations are then used to select optimal ranges of tail mass and length ratio to produce effective inertial adjustment of the legged robot due to tail motions. Data on biological specimens was found to satisfy the optimal ranges defined based on this analysis. The dynamic formulations were then used to derive a maneuvering controller consisting of a Path Planner to plan tail trajectories for goal oriented maneuvering behavior, and a Tail Motion controller to track the planned tail trajectory- evaluated experimentally in Chapter 8.

7.1 Related Work

Various modeling techniques have been investigated to study the maneuverability of mobile robots using an attached inertial appendage for either mid-air or on ground applications.

The majority of research on robotic tail modeling has focused on attitude control applications during mid-air flight using the zero-net transfer of angular momentum, an approach that has been extensively proposed in space robots and satellites for attitude control [111-113]. A lizard-inspired tail has been successful employed on a wheeled robot to dynamically self-right and

control pitch to smoothly transition between various ground slopes, using the assumption of zero net angular momentum exchange [40, 114]. A similar approach was presented for a miniature jumping robot and a bio-inspired kangaroo robot with an active tail utilized for pitch control between jumping instances [35, 43]. A Newton-Euler approach was used to model a cheetah robot with a two DOF attached tail during mid-air flight. The authors developed and simulated an attitude controller and demonstrated preliminary experimental results of disturbance rejection to maintain stability[31]. A moth inspired robot successfully demonstrated self-righting and mid-air turning using an inertial appendage [115].

There has also been research conducted to analyze the dynamics of mobile robots with ground contact friction. Patel et al. derived a mathematical model of a wheeled robot with a single DOF tail capable of roll motion that was assumed to be rotating about a grounded pivot point using the Euler-Lagrange formulation. The authors developed a control algorithm and demonstrated with simulations that the robot could perform a high-speed roll faster than a tail-less robot [116]. Kohut et al. investigated dynamic turning of a hexapod robot using yaw motion of a tail [117, 118]. In this analysis, it was assumed that the tail torque occurs as soon as the tail is actuated that overwhelms static friction; therefore, dynamic friction between the feet and ground induces a moment about an effective radius during tail actuation. However, this model did not consider the effects of translation. Casarez et al. developed an analytical model of a mobile robot with a reaction wheel that transferred a pure moment to the robotic body to determine the effects of motor voltage, friction, and wheel inertia had on heading angle [119]. Chernous'Ko modeled multi-body mechanical systems consisting of several links which can perform snake-like locomotion's along a horizontal plane in the presence of dry friction. Periodic motions consisting of slow and fast phases were used to create controllable longitudinal, latitudinal translational and rotational motions using a sequence of elementary motions [120, 121].

The subsequent sections will first model and analyze a robotic system consisting of a generic legged robot with an attached rigid body pendulum-tail using an adapted framework from [118, 120, 121] (section 7.2). These dynamic formulations will then be extended to a quadruped robot with an attached R3-RT to develop a method to scale/optimize articulated tails onboard legged robots for effective inertial adjustment applications and develop a maneuvering control algorithm (section 7.3) that will be evaluated in Chapter 8.

7.2 Robotic System Modeling and Control– Rigid Body Pendulum Tail

This section presents the robotic system under study and the model that is used for analysis throughout this section. The robotic system consists of a generic legged robot model, that represents either the quadruped or biped configuration constructed with RML mechanisms presented in Chapter 6 [18, 19], with an attached inertial tail. The legged robots mass is assumed to be concentrated in the body region due to the locations of its motors in the RML design. It is assumed that during a walking gait the legs do not significantly change the mass properties of the robot since the RML legs are composed of low inertia mechanisms. The tail is modeled as massless rod with a point mass located at its tip, and is driven by an actuation unit located at the tail base on the legged robot body.

Figure 7.1 depicts the free body diagram (top view) of the robotic system. A body attached frame of reference (O', $\mathbf{b}_1$, $\mathbf{b}_2$) is fixed to the legged robot at $O' = (x_0, y_0)$. The bodies are modeled as point masses m_0 (actuation unit), m_1 (legged robot body), and m_2 (tail tip mass). In the figure, the legged robot and tail are disconnected at the tail revolute joint. The tail gearbox and actuator assembly is located at point O'. The bodies can translate in the inertial $\mathbf{e}_1\mathbf{e}_2$-plane and the legged robot and tail can rotate relative to one another, about the $\mathbf{e}_3$-axis. The yaw heading angle of the legged robot and relative yaw angle of the tail are defined as θ and β, respectively. Therefore, the system is modeled with four DOFs.

The following variables will be used to represent the physical parameters of the system in this analysis: m_i represents lumped masses, v_i is the mass velocities, $\mathbf{P}_i$ is the position vector locating the point masses relative to O', and l_i represents a length or effective radius, defined as half the diagonal distance between legs for the legged robot. The index $i = \{0, 1, 2\}$ refer to the actuation unit, legged robot, and tail bodies, respectively.

An input torque of magnitude M_a applied onto the tail produces yaw rotation about its revolute joint. A torque of equal magnitude and opposite direction acts on the legged robot body during tail actuation.

Coulomb friction is used to model friction forces that act on the system at points of contact between the legged robot's feet and ground. During instances of sliding contact motion, the summation of friction forces of magnitude F_f is equal to μmg that oppose the direction of sliding velocity. M_f represents the reactive friction moment equal to μmgl_1, where l_1 represents the distance between the legged robot's COM to the tail attachment point. Here, μ represents the friction

coefficient (static and dynamic friction coefficients are assumed to be equivalent), m is the total mass of the system $m = m_0 + m_1 + m_2$, and g is the gravitational acceleration.
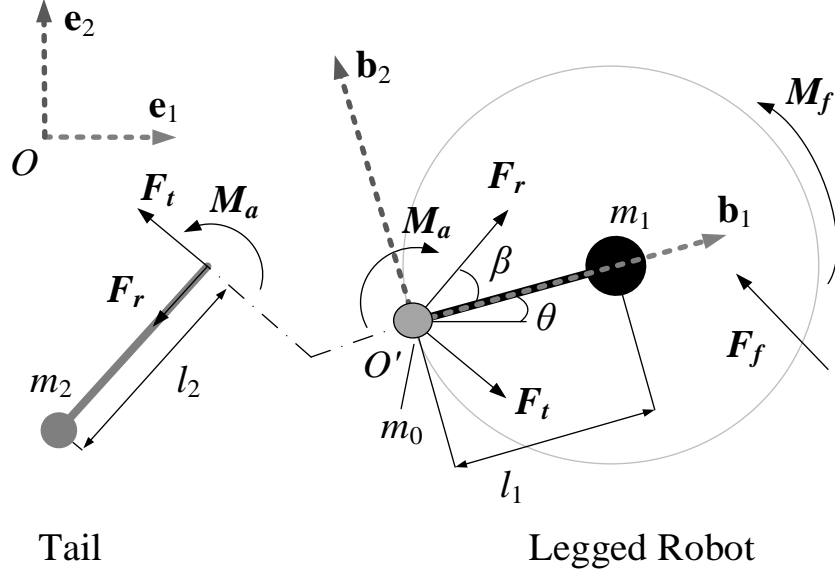
Figure 7.1: Free body diagram (top view) of the robotic system consisting of a generic legged robot and tail.

7.2.1 Kinematic Analysis

This section presents kinematic analysis of the robotic system, and derivations of the COM location and angular momentum of the robotic system.

With reference to Fig. 7.1, the COM of the system is computed as follows

$$\begin{aligned}
\boldsymbol{x}_c &= \frac{mx_0 + m_1 l_1 \cos(\theta) - m_2 l_2 \cos(\theta + \beta)}{m} \mathbf{e}_1 \\
\boldsymbol{y}_c &= \frac{my_0 + m_1 l_1 \sin(\theta) - m_2 l_2 \sin(\theta + \beta)}{m} \mathbf{e}_2
\end{aligned}$$
(7.1)

By defining the angular velocities of the quadruped and tail to be $\boldsymbol{\omega}_1 = \dot{\theta}\mathbf{e}_3$ and $\boldsymbol{\omega}_2 = \dot{\theta} + \dot{\beta}\mathbf{e}_3$, the total angular momentum of the robotic system about point O is given by Eq. 7.2

$$\boldsymbol{H}_O = \sum_{i=0}^{3} m_i \boldsymbol{P}_i \times \boldsymbol{v}_i \tag{7.2}$$

Substituting position and velocity relations into the above equation and evaluating the cross products yields the total angular momentum of the system:

$$\begin{aligned}
\boldsymbol{H}_O &= (\sin(\theta)l_1 m_1(y_0\dot\theta - \dot x_0) + \cos(\theta)l_1 m_1(x_0\dot\theta + \dot y_0) \\
&\quad -l_2 m_2[\cos(\beta+\theta)x_0(\dot\beta+\dot\theta) + \sin(\beta+\theta)(y_0(\dot\beta+\dot\theta) - \dot x_0) \\
&\quad +\cos(\beta+\theta)\dot y_0] - my_0\dot x_0 - mx_0\dot y_0)\mathbf{e}_3
\end{aligned} \tag{7.3}$$

7.2.2 Dynamic Analysis

This section analyses low and high-speed tail actuation to determine the conditions required to maintain equilibrium and derive the relations of maneuverability that result in translation and rotation of the legged robot.

Analysis of this low-speed tail motion will study the forces and moments produced by the tail to determine the conditions required to maintain equilibrium. Low-speed tail actuation involves rotating the tail to desired initial conditions while maintaining equilibrium. Equilibrium refers to steady state conditions where the system remains stationary due to resistive friction forces. To maneuver, a high-speed tail actuation will be performed to generate the necessary forces and moments to overcome friction. Let the magnitude of the moment induced by friction forces be denoted by M_f. During this type of actuation, it is assumed that the input torque magnitude is larger than the friction induced moment $M_a > M_f$; therefore, the external frictional forces between the quadruped's feet and ground can be neglected; thus, satisfying the conservation laws of linear and angular momentum. Since the system is initially at equilibrium, after fast tail motions, $\boldsymbol{x}_c$ and $\boldsymbol{y}_c$ are constants of motion and $\boldsymbol{H}_O = \boldsymbol{0}$. These conservation laws will then be used to analyze high-speed tail actuation, to formulate relations of maneuverability in terms of variations of translation and rotation of the robotic system.

7.2.2.1 Low-Speed Tail Actuation

In this section, the conditions to maintain equilibrium during low-speed tail actuation are derived. Assuming that the system is initially at equilibrium, estimated the upper bounds of generated forces

from tail actuation are used to analyze the resultant force balance on the legged robot, to determine the maximum threshold of tail motion such that friction induced forces cancel those caused by the actuator torque and loading generated by the tail.

For low-speed tail actuation, the maximum generated forces resulting from tail actuation that maintain system equilibrium occur at a certain upper, maximum threshold of tail motion parameters defined by ε and Ω, which represent the magnitude of angular velocity and acceleration, respectively. Using this notation and considering the tail as the system of study, the maximum magnitudes of F_t and F_r, tangential and radial force magnitude components exerted on the tail by the quadruped, and M_a can be estimated by

$$
\begin{aligned}
F_r &\leq m_2 l_2 \varepsilon^2 \\
F_t &\leq m_2 l_2 \Omega \\
M &\leq m_2 l_2^2 \Omega
\end{aligned}
\tag{7.4}
$$

Next, the effects of these maximum forces and moment on the legged robot consisting of masses m_0 and m_1 are studied. Rotational equilibrium will be maintained if the magnitude of the maximum induced moment $\boldsymbol{M}_B$, composed of the input torque and the moment resulting from maximum generated forces $\boldsymbol{F}_t$ and $\boldsymbol{F}_r$, about the combined COM does not exceed the friction induced moment magnitude M_f. Translational equilibrium will be maintained if the magnitude of the maximum combined generated forces, $\boldsymbol{F}_B$, does not exceed the friction force magnitude F_f. This means that the generated loading due to the low speed-tail actuation will not cause the legged robot to maneuver, since it is opposed by the friction induced forces and moments. Therefore, the conditions to maintain equilibrium are defined as

$$
\begin{aligned}
\left| \boldsymbol{F}_B \right| &\leq F_f \\
\left| \boldsymbol{M}_B \right| &\leq M_f
\end{aligned}
\tag{7.5}
$$

A balance of forces and moments about the combined COM with respect to the body attached frame yields the following equation for $\boldsymbol{F}_B$ and $\boldsymbol{M}_B$

$$\boldsymbol{F}_B = (F_r \cos\beta + F_t \sin\beta)\boldsymbol{b}_1 + (F_r \sin\beta - F_t \cos\beta)\boldsymbol{b}_2$$
$$\boldsymbol{M}_B = [x_c(F_t \cos\beta - F_r \sin\beta) - M_a + y_c(F_t \sin\beta + F_r \cos\beta)]\boldsymbol{b}_3 \qquad (7.6)$$

Substituting Eq. 7.4 into Eq. 7.6 and using the Cauchy- Schwarz inequality, relations for $|\boldsymbol{F}_B|$ and $|\boldsymbol{M}_B|$ can be defined as

$$|\boldsymbol{M}_B| \le m_2 l_2{}^2\Omega + 2m_2 l_2\left(\frac{m_1 l_1 + m_2 l_2}{m}\right)(\Omega + \varepsilon^2)$$
$$|\boldsymbol{F}_B| \le m_2 l_2\sqrt{\Omega^2 + \varepsilon^4} \qquad (7.7)$$

For multi-legged robotic systems, F_f can be estimated as a force proportional to the total weight of the robotic system mg and μ. Similarly, M_f is proportional to F_f and the effective radius l_1. Substituting these relations and Eq. 7.7 back into Eq. 7.5 yields the necessary condition to maintain equilibrium:

$$m_2 l_2{}^2\Omega + 2m_2 l_2\left(\frac{m_1 l_1 + m_2 l_2}{m}\right)(\Omega + \varepsilon^2) \le \mu m g l_1$$
$$m_2 l_2\sqrt{\Omega^2 + \varepsilon^4} \le \mu m g \qquad (7.8)$$

If the above inequalities are satisfied, the system will maintain equilibrium and remain stationary, enabling the robotic system to position the tail during low-speed tail actuation prior to maneuvering using high-speed tail actuation.

7.2.2.2 High-Speed Tail Actuation

In this section, the laws of conservation of linear and angular momentum, discussed in Section 7.4, are applied to derive the relations of maneuverability during high-speed tail actuation. Using the relation $\dot{\boldsymbol{x}}_c = \dot{\boldsymbol{y}}_c = \boldsymbol{0}$ from conservation laws, the time derivative of Eq. 7.1 is computed to derive the velocity of point mass m_0:

$$\dot{x}_0 = \frac{m_1 l_1 \dot{\theta} \sin\theta - m_2 l_2 (\dot{\theta} + \dot{\beta}) \sin(\theta + \beta)}{m} \mathbf{e}_1$$

$$\dot{y}_0 = \frac{-m_1 l_1 \dot{\theta} \cos\theta + m_2 l_2 (\dot{\theta} + \dot{\beta}) \cos(\theta + \beta)}{m} \mathbf{e}_2$$

(7.9)

Substituting Eq. 7.9 into the relation for total angular momentum, Eq. 7.3, where $\mathbf{H}_O = \mathbf{0}$ due to conservation laws, yields an expression for the heading angle rate of change

$$\dot{\theta} = -\frac{l_2{}^2 m_2 (m_0 + m_1) + d}{m_1 l_1{}^2 (m_0 + m_2) + m_2 l_2{}^2 (m_0 + m_1) + 2d} \dot{\beta}$$

(7.10)

Where $d = l_1 l_2 m_1 m_2 \cos\beta$. It can be observed from Eq. 7.10 that $\dot{\theta}$ is inversely related to $\dot{\beta}$. This relation is intuitive since any action of the tail will have an equal and opposite reaction on the quadruped. Numerical integration of Eq. 7.10 yield the relation of heading angle variation defined by

$$\Delta\theta = -\int_{\beta_0}^{\beta_f} f(\beta) d\beta$$

(7.11)

where β_0 and β_f represent the initial and final values of β. By integrating Eq. 7.9 over the initial and final values of tail motion, the translation of the system is computed to be

$$\Delta x_0 = \frac{-m_1 l_1 \Delta \cos\theta + m_2 l_2 \Delta \cos(\theta + \beta)}{m} \mathbf{e}_1$$

$$\Delta y_0 = \frac{-m_1 l_1 \Delta \sin\theta + m_2 l_2 \Delta \sin(\theta + \beta)}{m} \mathbf{e}_2$$

(7.12)

Equations 7.11 and 7.12 represent maneuverability relations of the legged robot due to high-speed tail actuations.

7.2.3 Evaluation of Maneuvering Applications with Ground Contact

This section modeled a generic legged robot in contact with the ground to derive the necessary conditions to enable inertial adjustment using dynamic motions of a pendulum-like tail. However, evaluation of Eq. 7.8 for quadruped robot with an attached R3-RT with the following parameters $m = 9.1$ kg, $l_1 = 0.5$ m, assumed to be walking on low friction terrain $\mu = 0.1$, requires up to 4.4 Nm to induce angular variation for maneuvering applications. This requirement exceeds the tails measured peak generated inertial force and moment bandwidth equivalent to 6 N and 3.1 N-m (evaluated in Chapter 4). Therefore, the approach to achieve maneuvering for this robotic system is modified to avoid ground friction by enabling a short airborne phase during the walking gait to achieve tail-aided maneuvering as will be further discussed in section 7.3 that will extend the dynamic formulations to a quadruped robot configuration with an attached R3-RT.

7.3 Robotic System Modeling and Control– Quadruped and R3-RT Tail

This section extends the dynamic modeling approach defined in section 7.2 to model the effects of an articulated tail (R3-RT) onboard a quadruped robot to optimize articulated tails onboard legged robots to maximize inertial adjustment applications. A controller is then defined to achieve goal oriented maneuvering behavior.

7.3.1 Robotic System

Figure 7.2 shows isometric views of the robotic system under consideration that consists of a quadruped robot with an attached R3-RT [14]. The quadruped robot is composed of four Robotic Modular Legs (RML) capable of performing planar walking gaits that enable planar forward locomotion. It is envisioned that dynamic motions of the articulated tail will enable enhanced maneuvering capabilities without the requirement of ground contact. For the quadruped robot, the majority of legged robot mass is concentrated in the body region due to the locations of the motors and low inertia leg mechanisms. It is assumed that during a walking gait the legs do not significantly change the mass properties of the robot since the legs are low inertia mechanisms (Chapter 6). The tail is composed of an actuation unit that houses a geared motor assembly and two articulated tail segments that are driven via cable transmission systems (Chapter 3 and 4).
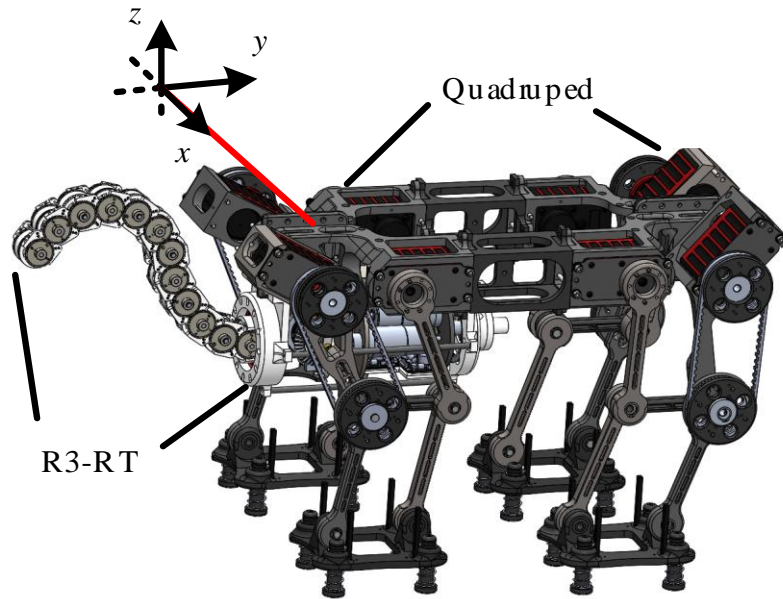
Figure 7.2: Legged robotic system: Quadruped with an attached R3-RT.

7.3.2 Kinematic Analysis

This section presents kinematic analysis of the robotic system, to derive the relations that will be used to develop the dynamic relations derived in the next section.

Figure 7.3 shows free body diagram of a generic legged robot with an attached n-link articulated tail. A global reference frame is defined as (O,$\mathbf{e}_1$,$\mathbf{e}_2$). A body attached frame of reference (O', $\boldsymbol{x}$, $\boldsymbol{y}$) is fixed to the legged robot at $O' = (x_0, y_0)$. The bodies are modeled as point masses m_0 (tail actuation unit), m_1 (legged robot body), and $m_{2\text{-}n}$ (tail linkage mass). The indices $i = \{0, 1, 2\text{-}n\}$ refer to the tail actuation unit, legged robot, and tail linkages, respectively. In the figure, the legged robot and tail are disconnected at the articulated tail attachment point to its actuation unit. The tail actuation unit is located at point O'. The legged robot and tail can rotate relative to one another, about the $\mathbf{e}_3$-axis. The yaw angle of the legged robot and relative angle of the tail input pulley rotation for segment 1 and 2 are defined as θ, $\beta_{seg,1}$, and $\beta_{seg,2}$, respectively. For an articulated tail that has n-kinematically coupled DOF's, we define the relative link rotations to be $\beta_{1\text{-}n}$.
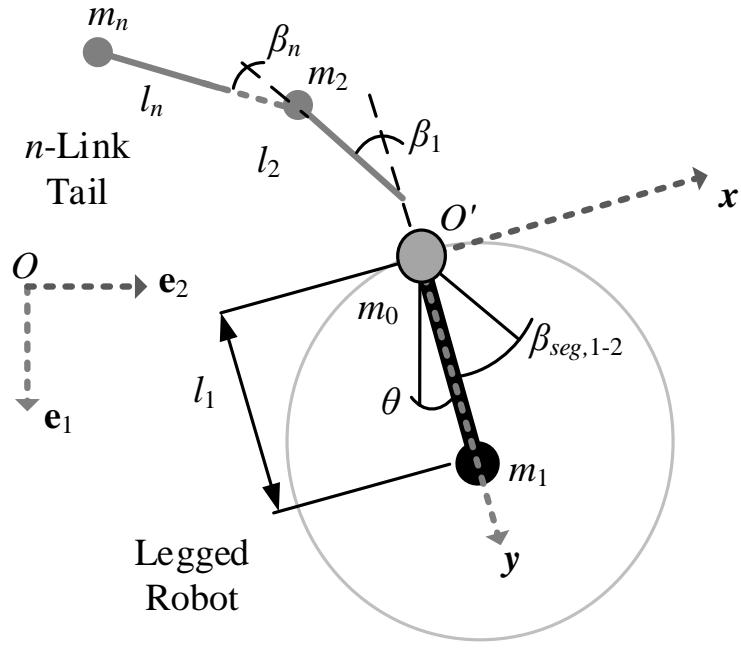
Figure 7.3: Schematic diagram of a robotic system consisting of a lumped parameter legged robot and an n-link articulated tail.

The following variables will be used to represent the physical parameters of the system in this analysis: m_i represents lumped masses, v_i is the mass velocity, $\mathbf{P}_i$ is the position vector locating the masses relative to O', and l_i represents a length of body i or effective length of the robot.

For an articulated tail with kinematically coupled DOF's, we define the relation of joint angles to be

$$\beta_i = \begin{cases} \eta_i \beta_{seg,1}, i=1 & \eta_i \beta_{seg,1} - \sum_{j=1}^{i-1} \beta_j, 1 < i \le 6 \\ \eta_i \beta_{seg,1}, i=7 & \eta_i \beta_{seg,1} - \sum_{j=1}^{i-1} \beta_j, 7 < i \le 12 \end{cases} \tag{7.13}$$

where η_i represents the coupling ratio of the i-th tail joint angle with respect to the input pulley rotation. Since the R3-RT tail is constrained with gears of equal pitch diameter and each segment has six links; therefore, $\eta_i = 1/6$. With reference to Fig. 7.3, the COM location and the total angular momentum of the system about point O are defined to be

$$\begin{bmatrix} x_c \\ y_c \end{bmatrix} = \sum_{i=0}^{n} \frac{\mathbf{P}_i m_i}{m_i} \tag{7.14}$$

$$\boldsymbol{H}_O = \sum_{i=0}^{n} m_i \mathbf{P}_i \times \boldsymbol{v}_i \tag{7.15}$$

7.3.3 Dynamic Analysis

Multi-segment models that conserve angular momentum during air born phases have been presented for describing the motion of a falling cat [122], geckos jumping between planes of various angular orientation [123], humans in space [123], and active-hinged cellular phones [124]. In this analysis we utilize the assumption of conservation of angular momentum to develop the dynamic formulations describing the angular variation of a legged robot due to high-speed articulated tail motions.

In the previous section, it was found that the friction at the feet during a quasi-static walking gait limited effective turning using high-speed tail motions [21]. This challenge could be mitigated by choosing to actuate the tail during an airborne gait phase in which all legs are lifted from the ground. However, for the quasi- static stable gait under consideration, at least two legs are in contact with the ground at all times. To enable an airborne phase, a small hop is added during the walking trajectory to lift the legged robot off the ground for 0.45 seconds and actuate the tail during this time for maneuvering. Furthermore, since quasi- static walking consists of forward walking velocities that do not exceed 0.3 m/s, it will be assumed that during tail motions for maneuvering applications, angular momentum will be conserved, therefore, $\boldsymbol{H}_0 = \boldsymbol{0}$, and $\boldsymbol{x}_c$ and $\boldsymbol{y}c$ are constants of motion.

Using this reasoning, taking the time derivative of Eq. 7.14 knowing that $\dot{\boldsymbol{x}}_c = \dot{\boldsymbol{y}}_c = 0$ yields the relation for the velocity of the actuation unit given by

$$\dot{\mathbf{P}}_0 = \begin{bmatrix} \dot{x}_0 \\ \dot{y}_0 \end{bmatrix} = f(m_i, l_i, \eta_i, \theta, \dot{\theta}, \beta_{seg,1-2}, \dot{\beta}_{seg,1-2}) \tag{7.16}$$

Substituting Eq. 7.16 into the relation for total angular momentum Eq. 7.15, where $\boldsymbol{H}_0 = 0$ due to conservation laws yields an expression for the legged robot angular velocity variation as result of articulated tail motion

$$\dot{\theta} = -f(m_i, l_i, \beta_{seg,1})\dot{\beta}_{seg,1} - f(m_i, l_i, \beta_{seg,2})\dot{\beta}_{seg,2} \tag{7.17}$$

Numerical integration of Eq. 7.17 yields the relation of angle variation defined by

$$\Delta\theta = -\int f(m_i, l_i, \beta_{seg,1})d\beta_{seg,1} - \int f(m_i, l_i, \beta_{seg,2})d\beta_{seg,2} \tag{7.18}$$

It can be observed from Eq. 7.18 that $\Delta\theta$ is inversely related to $\Delta\beta_{seg,1\text{-}2}$. This relation is intuitive since any action of the tail will have a proportional but opposite reaction on the legged robot.

7.3.4 Tail Geometric and Mass Parameter Optimization

Previous approaches of scaling pendulum-like tails have utilized efficacy that relates constant inertia of a pendulum to that of the legged robot [53]. This criteria cannot be used for scaling an articulated tail due to varying inertia properties during motion. This section presents analysis to optimize the articulated R3-RT onboard the quadruped robot to maximize angular variation effects due to high-speed tail motions. For design purposes, the articulated tail can be scaled relative to the legged robot by varying its relative mass distribution and length. Therefore, let the mass and length ratio be defined as σ and λ, respectively

$$\sigma = \sum_{i=2}^{n} m_i / (m_0 + m_1) \tag{7.19}$$

$$\lambda = \sum_{i=2}^{n} l_i / l_1 \tag{7.20}$$

118

Where σ represents the ratio between the of the summation of the articulated tail linkage masses with respect to the legged robot and tail actuation unit mass, and λ represents the ratio between the total articulated tail length with respect to distance between the legged robot COM and the tail attachment point (Fig. 7.3).

For the robotic systems under consideration consisting of a quadruped robot with a 12–link tail with constant properties $m_1 = 5.7$ kg, $m_0 = 3.1$ kg, and $l_1 = 0.5$ m, Eq. 7.18 was evaluated to compute $\Delta\theta$ for a prescribed tail motion of $\Delta\beta_{seg,1-2} = 60°$ while varying σ and λ computed using Eq. 7.19 and 7.20, respectively. Results of this analysis are presented as a contour plot in Fig. 7.4. The tangency of the contour lines of constant $\Delta\theta$ or observable rate of color change indicates the amount of sensitivity with respect to variations of σ and λ. For large values of σ and λ, tangency nearly approaches but never reaches a zero value, indicating that sensitivity is reduced for large mass and length ratios and that a global maximum does not exist in a constrained design space. By first analyzing the effects of varying mass ratio, it is interesting to note that the tangency for the lines of constant $\Delta\theta$ is greatest within the range of $\sigma < 0.5$. Similarly, by observing the contour plot rate of color change along the vertical axis, the rate of change is greatest for $\lambda < 2$. Thus, indicating that angular variation becomes less sensitive with increased mass and length ratios beyond these thresholds.

These trends physically make sense since adding additional tail mass does increase the tails inertial leverage; however, it also increases the effective weight of the entire system that can result in impeded motion. Since tail inertia increases quadratically to length it would be advisable to design a robotic tail as long as possible within the desirable mass ratio ranges while satisfying actuator torque/angular velocity and workspace constraints to prevent contact with the robot body or ground during operation.

A similar analysis was conducted for the DMST mechanism onboard the biped robot; however, the same trends and optimal regions were observed similar to Fig. 7.4.
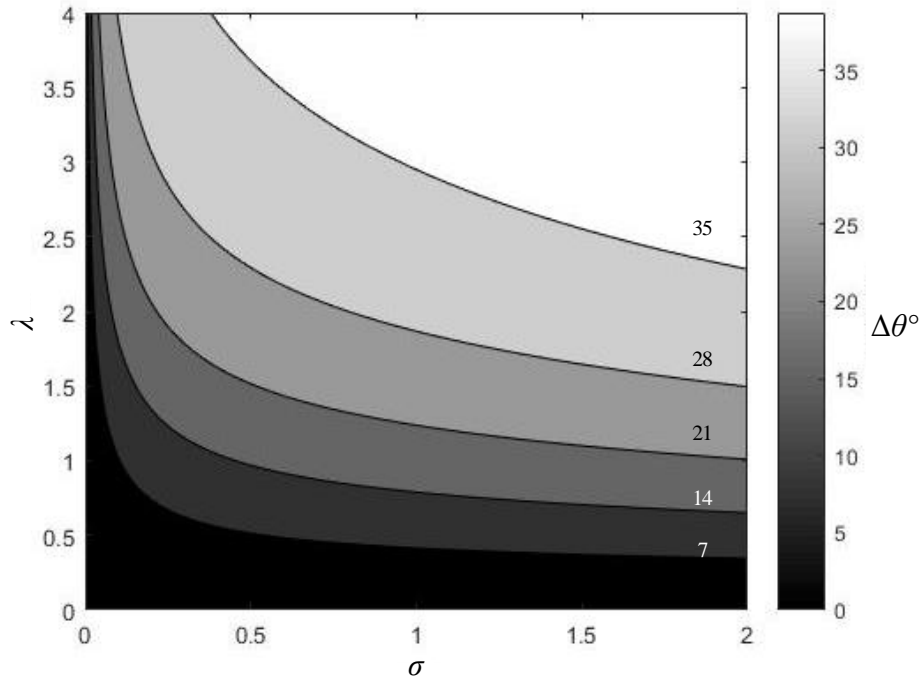
Figure 7.4: Angular variation contour plot for the quadruped and R3-RT system resulting from a $\Delta\beta_{seg,1\text{-}2} = 60°$ tail motion for various mass and length ratio.

7.3.4.1 Comparison to Biological Tails

This section compares the optimal ranges computed via the angular variation relation as observed from Fig. 7.4 with measured mass and length ratios of biological animals which range in topology but utilize their tails for maneuvering and stabilization applications as described in Chapter 1.

Table 7.2 presents the mean measured mass and length ratio for animals that utilize their tails for maneuvering and stabilization. The first observation that falls in line with analysis is that mass and length ratios of these animals fall within high sensitivity ranges observable Fig. 7.4 equivalent to $\lambda < 2$ and $\sigma < 0.5$. Both the green anole lizard [125], and gecko [34] utilize their tails during aerial flight to induce zero angular momentum reorientations in mid-air to prevent the possibility of injury; thus, permitting effective maneuvering and/or avoiding undesirable environments. It is interesting to note that the green anole has a mass ratio that is a factor of 0.5 less than the gecko's; however, to compensate its length ratio is approximately twice as large. In comparison to the gecko, the cheetah's tail length ratio closely matches with a value of $\lambda = 0.9$; however, its mass ratio is significantly lower. Recent research by Patel et.al [126] indicates that cheetah's long tail fur results in aerodynamic effects where the tail is used like a rudder in air to

compensate for its low mass ratio and enhance inertial loading resulting from high-speed tail motions. The wall lizard uses its tail for static stabilization applications, similar to a balancing weight, to more evenly distribute weight over flimsy vegetation and as a counterpoise or coil it wraps around branches while climbing [127]. It is interesting to note that since the tail is not used for dynamic high-speed motions, it tail length and mass ratio is relatively longer and heavier than other animals where $\sigma = 0.28$ and $\lambda = 2.1$; however, both are a factor of ~2 larger than that of the Gecko.

Although there does not exist sufficient measured data from biological animals found in nature to conclude an optimal compromise between mass and length ratios for tail-aided inertial adjustment applications. The results of this comparative analysis corroborate the optimal ranges concluded from analysis of the contour plot presented in Fig. 7.4 that can be used to further aid the process of scaling articulated tails onboard legged robots to maximize angular variation resulting from high speed tail motions.

Table 7.1: Measured mass and length ratios from animals that utilize tails for inertial adjustment applications.

Animal	Tail Parameter	
	σ	λ
Green Anole [125]	0.05	1.82
Gecko [34]	0.1	0.92
Cheetah [126]	0.02	0.9
Wall Lizard [127]	0.28	2.1

7.3.5 Maneuvering Control

This section details the maneuvering control laws, illustrated in Fig. 7.5, used to operate the robotic system. The Path Planner control law plans the desired tail trajectory that implements goal oriented maneuvering behaviors, and the Tail Motion control law calculates the desired input angular rotation to be tracked by the articulated tail.
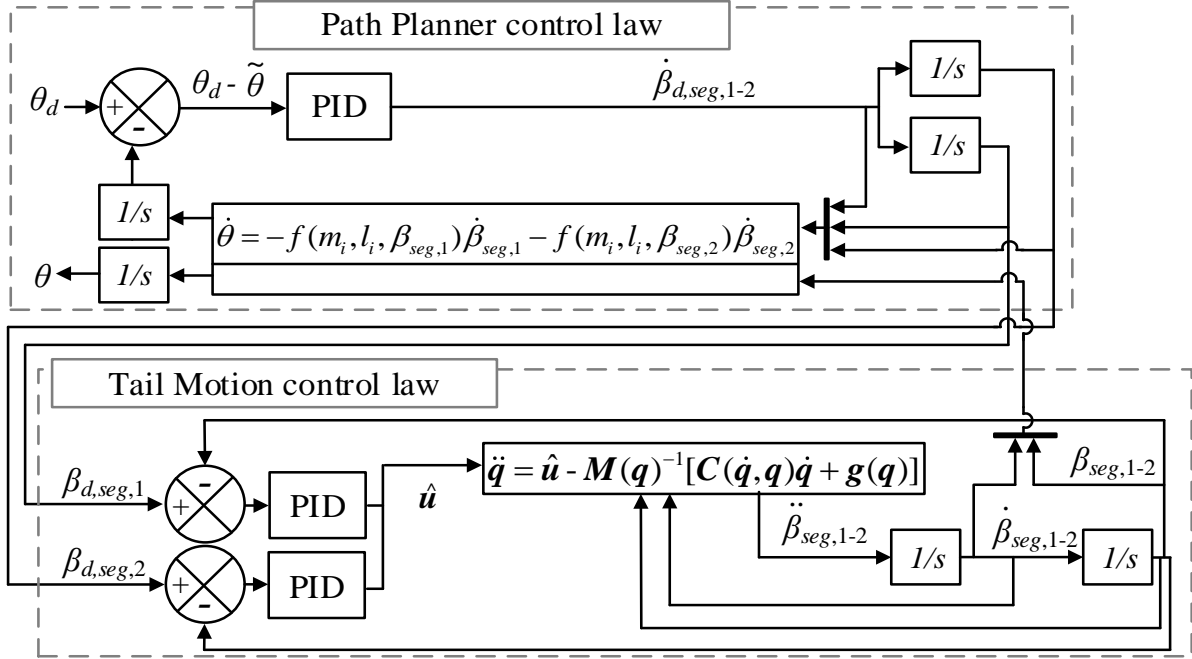
Figure 7.5: Tailed quadruped maneuvering control concept.

The set point of the Path Planner controller, Fig. 7.5, is a desired legged robot orientation θ_d that represents a desired yaw turning angle for maneuvering. For maneuvering, the tail will produce a planar motion with a fixed roll angle to orient the articulated tail in the *xy* plane (Fig. 7.2), a PID comparator outputs a desired tail input velocity that is used to synchronize the two tail segments based on feedback from an estimated quadruped angle ($\tilde{\theta}$) by integrating the output of the legged robot angular velocity variation Eq. 7.17. The synchronized angular velocities are integrated to obtain a desired tail trajectory $\beta_{d,seg,1\text{-}2}$ that is fed to the Tail Motion control law which is used to control the tail motion to achieve the desired goal orientated behavior.

The controlled tail state variables are defined as $\boldsymbol{q} = [\beta_{seg,1}, \beta_{seg,2}]$. To develop a state based Tail Motion control law, the tail dynamic model, previously derived in section 4.1.2 [14], can be represented as

$$M(q)\ddot{q} + C(\dot{q},q)\dot{q} + g(q) = u \tag{7.21}$$

122

Where $M(q)$ is the inertia, $C(\dot{q},q)$ is the tail's centripetal and Coriolis effect, $g(q)$ is the gravitational effect, and u is the input torque. However, to implement a PID based controller for tail trajectory tracking, the dynamic model is decoupled by multiplying Eq. 7.21 by $M(q)^{-1}$ and using a nonphysical torque input, $\hat{u}$, as follows

$$\ddot{q} = \hat{u} - M(q)^{-1}[C(\dot{q},q)\dot{q} + g(q)]$$
$$\text{where } \hat{u} = M(q)^{-1}u \tag{7.22}$$

Using this approach, a PID comparator for each segment is used to convert the tail input trajectory errors into that is fed into the decoupled dynamic model, Eq. (7.22), to obtain the tail input angular acceleration as seen in Fig. 7.5. Integration yields tail angular velocity and orientation that is fed back into the decoupled dynamic model and angular velocity relation for a more accurate calculation of θ. The tail segment angular velocities are sent to motor drivers that regulate current to the motors as described in section 3.3.1 [14] to generate accurate dynamic tail motions. Experimental results of this control approach are evaluated in Chapter 8.

Evaluation of this controller, that utilizes non-linear equations, requires a computation time of approximately 0.76 seconds using Matlab ODE45 solver with a time step of 0.001 seconds. Therefore, as will be demonstrated in Chapter 8, elementary tail motions will be pre-calculated for a desired set of yaw maneuvering angles of the quadruped robot. For real-time control, a series of these pre-calculated elementary tail motions will be performance sequentially during separate robot jump phases to achieve desired quadruped maneuvering yaw angle.

7.4 Conclusion

This chapter presented a dynamic modeling approach of a robotic system composed of a legged robot with an attached articulated robotic tail.

Section 7.1 reviews existing literature on dynamic modeling and control of robotic tails onboard mobile robots for inertial adjustment applications.

Section 7.2 presented the analytical formulation to derive inertial adjustment relations, resultant translation and rotation, of a rigid pendulum-like tail onboard a legged robot in contact with the ground to study the transition between low-speed tail motions to maintain stability (no

motion) and high-speed tail motions to achieve inertial adjustment- translation and angular variation of the legged robot.

These dynamic formulations were then extended in section 7.3 to model and articulated tail (R3-RT) onboard the proposed reduced-DOF quadruped robot. Significant contributions involve analysis for scaling articulated tails to select optimal mass and length ratios to maximize inertial adjustment capabilities in the form of angular rotation of the legged robot as a result from tail motion. Results indicated that past a certain mass ratio threshold, the addition of tail mass does not significantly cause large variations of angular variation. This trend physically makes sense because tail mass does increase the inertial forces transferred to the legged robot, but also increases the overall weight of the system, resulting in a larger friction induced moment that impedes motion of the system. A similar trend was observed for increasing length ratio, past a certain threshold heading angle variation decreased due to inertial forces in the tangential and radial directions that counter act rotation of the system.

The dynamic formulations were then used to derive a maneuvering control law consisting of a Path Planner controller to plan tail trajectories for goal oriented maneuvering behavior, and Tail Motion controller to decouple manipulator dynamics and control an articulated tail to track the planned tail trajectory. However, evaluation of this controller, that utilizes non-linear equations, creates challenges for real-time computation of tail motions to achieve goal-oriented maneuvering. Therefore, elementary tail motions will be pre-calculated for a desired set of yaw maneuvering angles of the quadruped robot and evaluated in experimental and simulation based case studies in Chapter 8.

CHAPTER 8: EXPERIMENTAL AND SIMULATION RESULTS OF TAIL-AIDED MANEUVERING AND STABILIZATION

This chapter investigates the articulated tails (R3-RT and DMST) abilities to augment the performance of the proposed reduced-DOF legged robots (quadruped and biped) and evaluate the performance of the combined systems, legged robots with attached articulated tails, in satisfying the walking criteria defined in section 6.2.

Section 8.1 demonstrates the effectiveness of the R3-RT prototype in conjunction with a virtual quadruped in experiments, with a comparison to simulation results, to demonstrate various maneuvering case studies to validate the control approach defined in section 7.3.5 and produce compensatory tail motion to reject external disturbances to enhance the legged robot's stability.

Section 8.2 demonstrates the effectiveness of the DMST onboard a biped robot in simulation based case studies where the tail is used for disturbance rejection to enhance stabilization while standing and to enable a quasi-static forward walking gait and left/right turning for enhanced maneuvering.

8.1 Quadruped with Attached R3-RT: Maneuvering and Stabilization

As a precursor to full scale implementation of the tailed-quadruped, a prototype R3-RT is used in conjunction with a simulated quadruped walking in a virtual environment on flat terrain using a multi-body dynamics physics simulator MSC-ADAMS. This software enables a comprehensive simulation and motion analysis of the legged robot capable of solving for the kinematics and dynamics in the presence of foot/ground contact and friction.

Figure 8.1 illustrates the experimental setup used in this section. The R3-RT prototype is mounted on a six-axis load cell (Sunrise Instruments M3716B) to measure the inertial forces and moments generated by the tail motions, which are then mapped in real-time into the equivalent forces and moments at the tail frame origin on the virtual quadruped robot using a Simulink-ADAMS co-simulation. As mentioned in section 7.3.5, to enable real-time experimentation, pre-calculated tail motions to achieve goal oriented yaw maneuvering of the quadruped robot are

performed in conjunction with the quadruped simulation to affect its heading angle to enable left and right turning.
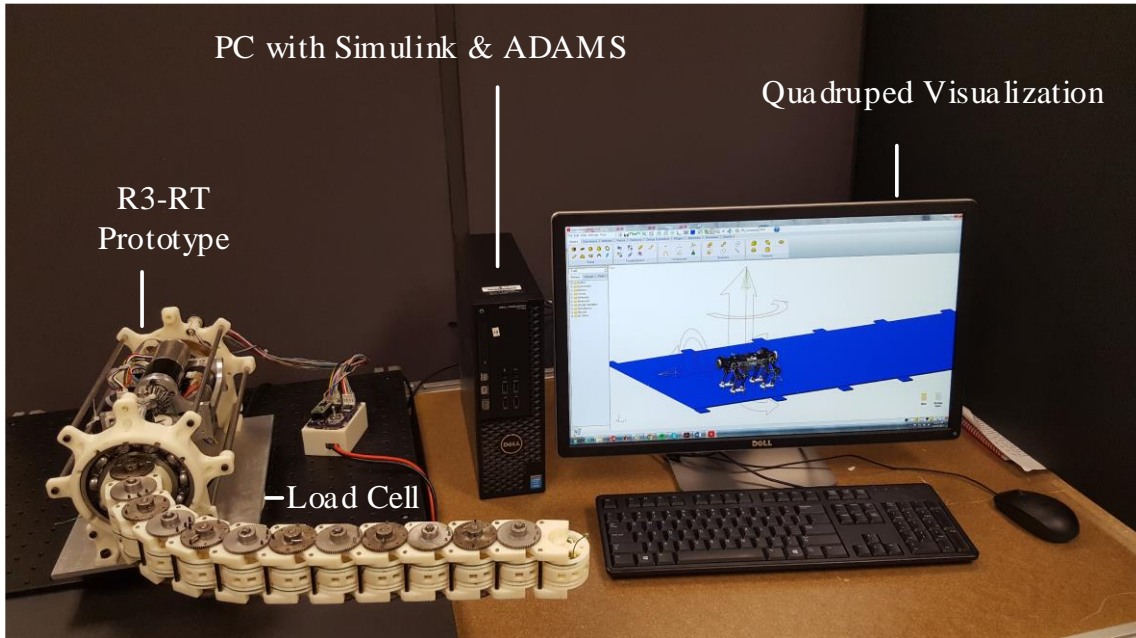
Figure 8.1: Experimental setup: Quadruped with R3-RT.

8.1.1 Maneuvering Case Studies

For the maneuvering case studies, the quadruped produced a 0.45 sec jump (as described in section 7.3.2) during which the tail, starting from a straight home configuration, produced planar tail motions to a final segment configuration while maintaining a fixed roll angle to enable rotation of the robotic system about the z-axis (Fig. 7.2). With reference to Figs. 7.3 and 7.6, to measure the repeatability of these experiments and identify variability due to foot/ground impacts or friction upon landing of the quadruped robot upon completion of the airborne phase and tail motions, 5 trials were produced to achieve a desired set point $\theta_d = \{20, 10, 5\}°$ where the tail input angles were varied between $\beta_{seg,1,2} = -\{0{:}106, 0{:}52, 0{:}26\}°$, respectively. Results of the legged robot yaw angle θ from the simulated controller (section 7.3.5) and measured values from the quadruped virtual simulation are shown in Fig. 8.2. The RMS errors between steady state simulation and experimentally measured θ values of the virtual quadruped at 0.8 sec are reported in Table 8.1. The maximum quadruped turning the tail can produce without reaching its workspace limit of $\beta_{seg,1,2} = 120°$ was for the $\theta_d = 20°$ case scenario. For this case scenario, the tail produced the largest

angular displacement. At the final tail configuration, static gravitational loading induced the greatest pitch and roll angular variation of the robot equivalent to 16° and 18.3° prior to ground impact of the rear, right leg – considered to be destabilizing effects due to maneuvering. Such an unbalanced orientation of the legged robot upon impact with the ground produces unbalanced forces that cause un-modeled rotational effects and deviation from the angular momentum conservation assumption; therefore, resulting in the largest RMS error of 5.14°. For the remaining case scenarios $\theta_d = 10°$ and 5°, since the tail produced motions with less angular displacements, the legged robot angular roll and pitch variation during the airborne phase is decreased due to less unbalanced gravitational loading effects which result in the quadruped landing in a more symmetric configuration; thus, reducing the undesirable effects of ground impact. It is for this reason the RMS error decreases with a reduction of θ_d.
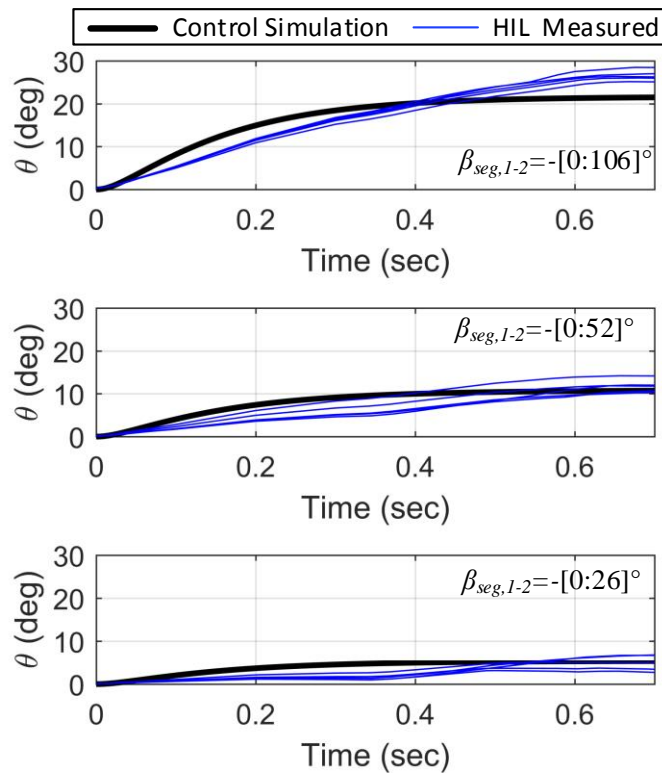
Figure 8.2: Maneuvering control simulation and measured results for the quadruped yaw angle turning of set points $\theta_d = \{20, 10, 5\}°$ listed from top to bottom respectively.

Table 8.1: Desired set point turning angle and RMS error

Desired Angle θ_d	RMS Error
20°	5.14°
10°	0.47°
5°	0.36°

Future work will investigate articulated tail motion in combination with tail roll motion to reduce the effects of undesirable pitch and yaw motions of the legged robot during maneuvering applications for a smoother landing to minimize the yaw angle RMS error of the legged robot.

8.1.2 Stabilization Case Studies

The stabilization controller in this case study will prescribe a tail motion that utilizes the tail's inertial and gravitational loading to counteract a destabilizing load applied to the quadruped [128]. Based on the quadruped's geometry and mass distribution, the moment of inertia with respect to the roll axis **y** is significantly lower than that of the pitch axis **x** (axes defined in Fig. 7.2), making roll angle destabilization more likely for a lower magnitude disturbance. Therefore, the stabilization controller is designed to counteract a destabilizing moment about this roll axis.

Roll destabilization can be detected from the quadruped's roll angle ρ. During steady-state locomotion, slight variations in ρ are expected, and the range of acceptable roll angles without requiring tail intervention can be defined as $\rho \in [-\rho_b, \rho_b]$. Beyond these limits, the tail should be actuated to oppose the destabilizing roll influence. The required stabilizing tail actuation is parameterized by the variable $\kappa \in [-1, 1]$, defined in Eq. 8.1, where ρ_{lim} is the roll angle magnitude beyond which $|\kappa| = 1$, 'sat' is the unit saturation function, and 'sgn' is the signum function. The $-\text{sgn}(\rho)$ term ensures that stabilizing control action acts in opposition to the quadruped's roll angle.

$$\kappa = \begin{cases} 0 & |\rho| \leq \rho_b \\ \text{sat}(-\text{sgn}(\rho)\dfrac{|\rho|-\rho_b}{\rho_{\text{lim}} - \rho_b}) & |\rho| > \rho_b \end{cases} \tag{8.1}$$

When $|\kappa| > 0$, a methodology for mapping κ into a second-order continuous tail trajectory is needed; the variable ψ is used to parameterize this continuous trajectory of roll DOF φ of the

R3-RT mechanism (Fig. 3.2). In this analysis, the tail segments are held constant in a maximum inertial configuration where $\beta_{seg,1} = 90°$ and $\beta_{seg,2} = 0°$. The tail segments initially are oriented along the negative z axis (Fig. 7.2) to achieve an initial roll angle of $\varphi = 180°$. A unit damped harmonic oscillator for ψ is defined in Eq. 8.2 with κ as its forcing function, where ξ and ω_n are the oscillator's damping ratio and natural frequency, respectively. To minimize the system's settling time without overshoot, ξ is set equal to 1.

$$\frac{1}{\omega_n^2}\ddot{\psi} + \frac{2\xi}{\omega_n}\dot{\psi} + \psi = \kappa \quad , \quad \{\psi_0, \dot{\psi}_0\} = 0 \tag{8.2}$$

The solution of Eq. 8.2 for $\psi \in [-1,1]$ is then mapped linearly to tail roll angular displacements of $\varphi \in [-90, 90]°$ to induce the maximum gravitational loading to reject destabilizing roll disturbances during a walking gait.

To replicate destabilization scenarios during a walking gait in the simulation, an impulse moment of magnitude ΔM is applied about the roll axis for 0.2 seconds. Stabilization capability is studied by comparing the response of the robot in controlled and uncontrolled mode.

When $|\Delta M| \leq 10.1$ Nm, the disturbance is sufficient enough to start tipping the robot; however, for a value of 10.1 Nm $\leq |\Delta M| \leq 25.6$ Nm, the robot is marginally stable since it can stabilize itself without the use of tail compensatory motion due to gravitational loading of the robotic system that inherently rejects disturbances. For $|\Delta M| \geq 25.6$ Nm, the external disturbance is sufficient to cause tipping over, destabilizing the quadruped, without active tail motion. However, when the tail is used to stabilize the quadruped, the robot can tolerate larger disturbances without tipping over.

Figure 8.3 illustrates two case scenarios of measured roll angle trajectories of the virtual quadruped in controlled and uncontrolled mode. In controlled mode, the parameters of Eq. 8.2 are set to $\rho_b = 3°, \rho_{lim} = 13°, \omega_n = 20\,\text{rad}/\text{sec}$. For $\Delta M = 30.2$ Nm, in uncontrolled mode the robot loses stability and tips over. In controlled mode, the roll DOF is contained to a maximum value of 42.2° where the tail roll angle is varied to between $\varphi = [0:90]°$, representing maximum tail compensation. The tail was unable to compensate for disturbances $|\Delta M| > 30.2$ Nm. For $\Delta M = 20$ Nm, in uncontrolled mode the quadruped roll is varied to between $\varphi = [0:16.92]°$ before returning to its stable walking gait in 0.65 sec after the quadruped was disturbed. In controlled mode the tail

reduces the quadruped roll angle to a maximum value of 5.1°and enables the quadruped robot to gain stability in 0.35 sec; thus, enabling more effective forward walking.

Controlled	Uncontrolled	ΔM
●—	●—	30.2 Nm
○—	○—	20 Nm
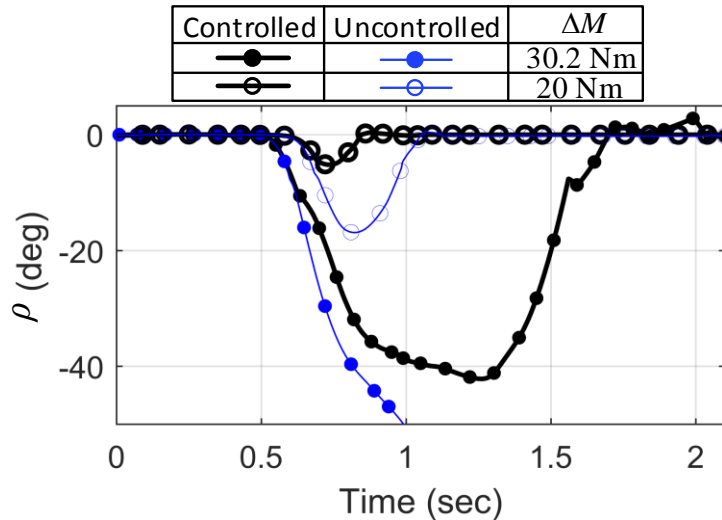
Figure 8.3: Stabilization case scenario for $\Delta M = \{30.2, 20\}$ Nm illustrating measured roll rotation of the quadruped robot in both controlled and uncontrolled state.

8.2 Biped with Attached DMST: Stabilization and Maneuvering

The biped configuration as a standalone machine without the use of an articulated tail cannot satisfy the aforementioned walking criteria defined in section 6.2; thus, justifying the use of an attached DMST mechanism to enable enhanced stabilization and maneuvering. The performance enhancement capabilities enabled via the DMST tail are investigated for enhanced stabilization (disturbance rejection) in section 8.2.1 and to enable stable walking gait with the ability to maneuver (turn left and right) in section 8.2.2.

8.2.1 Stabilization: Pitch Angle Disturbance Rejection

Figure 8.4 shows the DMST mounted vertically on a biped robot constructed of a pair of planar of connected RML mechanisms (chapter 6). Figure 8.5 shows the schematic diagram of the system. In this analysis, the y-axis of the DMST (at point D) aligns with the y-axis of the biped body-fixed frame B (at point B), and the x-axes of these frames are aligned when the tail roll $\phi = 0°$ (Fig. 3.8-3.9). To model the pitching behavior of the robot in the $+z$ direction, a revolute joint between the

130

ground and rear foot contact is prescribed at frame J (at point J), where z_J is the axis of rotation of the joint.
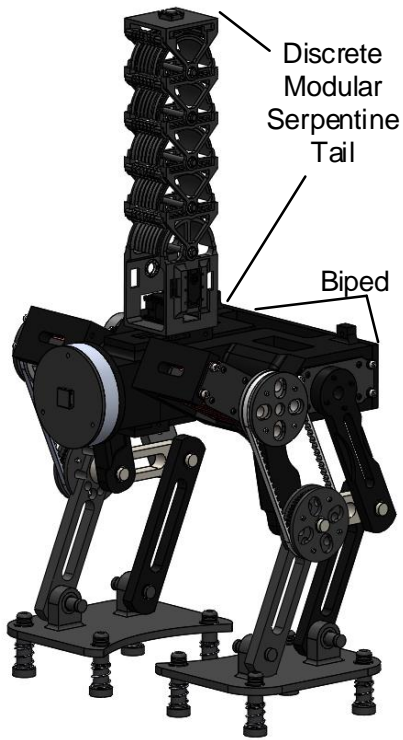
Figure 8.4: Bipedal robot with vertically mounted DMST.
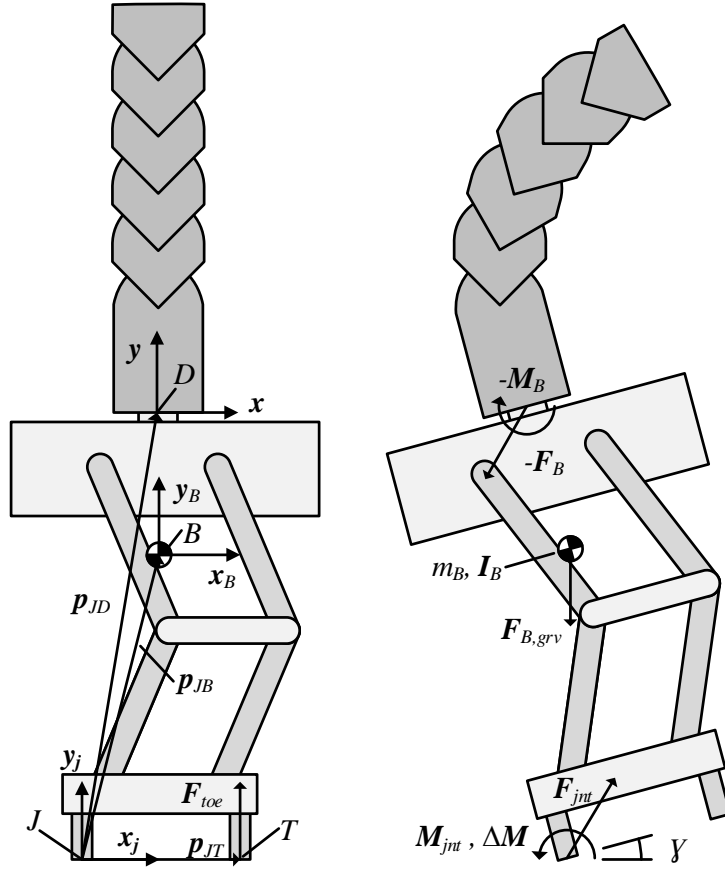
Figure 8.5: Schematic diagram showing the biped and tail frame definitions, kinematic parameters and system loading.

This analysis will study how the tail can actively to prevent the biped from tipping over. The system will be modeled as two-bodies consisting of a 5-link DMST capable of producing pitch bending motions and a stationary biped robot. The kinematics of the system are defined with respect to the ground fixed frame J in Fig. 8.5. The pitch of the system is defined by the angle γ, and the orientation of the biped-fixed frame at point B is defined by R_B in Eq. 8.3 along with the biped's angular velocity (ω_B). Three points at which loading is applied on the biped are located at the biped COM position at point B (origin of biped frame), the DMST connection point D, and the forward toe contact at point T. In the biped frame, the position vectors from the origin of frame J to the origin of frame B ($p_{JB,lcl}$) and point D ($p_{JD,lcl}$) are fixed, and their definition in the global frame J may be found using Eq. 8.4. The position p_{JT} is fixed in the global frame and will be prescribed based on the foot geometry.

$$R_B = R_Z(\gamma), \quad \omega_B = \dot{\gamma}z \tag{8.3}$$

$$p_{JB} = R_B p_{JB,lcl}, \quad p_{JD} = R_B p_{JD,lcl} \tag{8.4}$$

Furthermore, due to the motion of point D fixed to the biped, the formulations for several kinematic parameters for the DMST defined in section 5.1 need to be modified for this analysis. Equation 8.5 defines modifications for the tail link 0 orientation R_0, the link 0 angular velocity ω_0, and the joint 0 position $p_{0, jnt}$.

$$R_0 = R_B R_Y(\phi), \quad \omega_0 = \omega_B + \dot{\phi}R_0 y, \quad p_{0, jnt} = p_{JD} \tag{8.5}$$

The loading associated with the tail ($-F_B$ and $-M_B$, defined in section Chapter 5), joint (F_{jnt} and M_{jnt}), toe (F_{toe}), gravity ($F_{B,grv}$) and disturbance (ΔM) are shown in Fig. 8.5. The disturbance moment ΔM represents a generalized disturbance to the system, such as an impact force on the body of the biped robot, or an unexpected shift in height of the ground. Loading equal and opposite to the DMST loading is applied to the biped at point D as the control input to the system. When $\gamma = 0°$, the forward toes of the leg will be in contact with the ground, generating a force to prevent the pitch angle from becoming negative. In addition to the gravitational and inertial loading from the tail incorporated into F_B and M_B, a gravitational force $F_{B,grv}$ is also applied at the biped COM. Finally, F_{jnt} and M_{jnt} act at the revolute joint to counteract loading other than pitch angle rotation. For F_{jnt}, all three components can be non-zero to ensure equilibrium, and M_{jnt} can be non-zero in the x-y plane of frame J. The z-component of M_{jnt} must be zero, since the z-axis is the revolute joint axis and a revolute joint by definition cannot support a constraint moment about its joint axis.

The force and moment equilibria of the system taken with respect to the biped COM is defined in Eq. 8.6, where m_B and I_B are the biped mass moment of inertia and the vectors p_{BJ}, p_{BD} and p_{BT} are the position vectors from the frame B origin to frame J, and points D, T respectively.

$$m_B \ddot{p}_{JB} = F_{jnt} + F_{toe} + F_{B,grv} - F_B$$

$$I_B \dot{\omega}_B + \tilde{\omega}_B I_B \omega_B = \Delta M + M_{jnt} + \tilde{p}_{BT} F_{jnt} + \tilde{p}_{BF} F_{toe} - M_B - \tilde{p}_{BD} F_B \tag{8.6}$$

133

Equation 8.6 moment equation may be reformulated in relation to point J to utilize the vectors $\boldsymbol{p}_{JB}$, $\boldsymbol{p}_{JD}$ and $\boldsymbol{p}_{JT}$, as shown in Eq. 8.7. Where $\boldsymbol{p}_{JT}$ is the position vector from frame J to point T.

$$
\begin{aligned}
&\left(\boldsymbol{I}_B - m_B \tilde{\boldsymbol{p}}_{JB} \tilde{\boldsymbol{p}}_{JB}\right) \dot{\boldsymbol{\omega}}_B + \tilde{\boldsymbol{\omega}}_B \left(\boldsymbol{I}_B - m_B \tilde{\boldsymbol{p}}_{JB} \tilde{\boldsymbol{p}}_{JB}\right) \boldsymbol{\omega}_B \\
&= \Delta \boldsymbol{M} + \boldsymbol{M}_{jnt} + \tilde{\boldsymbol{p}}_{JT} \boldsymbol{F}_{toe} + \tilde{\boldsymbol{p}}_{JB} \boldsymbol{F}_{B,grv} - \tilde{\boldsymbol{p}}_{JD} \boldsymbol{F}_B - \boldsymbol{M}_B
\end{aligned}
\tag{8.7}
$$

Table 8.2 and Eq. 8.8 define the properties of the biped and DMST designs extracted from the CAD model shown in Fig. 8.4 used in these simulations. A 3.5 kg proof mass is added to the terminal link of the tail, as shown in the definition of m_5, to provide the tail with sufficient loading capacity to affect the biped dynamics.

Table 8.2: Simulation parameters for biped with DMST.

Property	Value	Property	Value
$\boldsymbol{p}_{JB,lcl}$	[96.4; 336.9; 0] mm	m_B	9.525 kg
$\boldsymbol{p}_{JD,lcl}$	[52.8; 497.2; 0] mm	m_0	0.350 kg
$\boldsymbol{p}_{JT}$	[190.0; 0; 0] mm	$m_{\{1\text{-}4\}}$	0.267 kg
$L_{J2C,0}$	63.3 mm	m_5	3.5 kg
L_{J2C}	59 mm	$L_{J2J,0}$	105.25 mm
$L_{J2C,n}$	49 mm	L_{J2J}	60 mm
r_i	[9, 16, 22, 28, 34] mm	r_{cbl}	25 m

$$
\boldsymbol{I}_B = \begin{bmatrix} 0.3929 & -0.0142 & 0 \\ -0.0142 & 0.2782 & 0 \\ 0 & 0 & 0.2780 \end{bmatrix} \text{kg}-\text{m}^2
\tag{8.8}
$$

A controller is designed to modify the bending of the tail in response to undesirable pitch angle displacement and velocity. For a given tail, there will be a motor angle $\vartheta_{m,max}$ that corresponds to the tail configuration that generates the maximum pitch gravitational moment with respect to the tail frame B. For the tail under consideration, this will occur when the sum of the joint angles ϑ_1 through ϑ_5 is 90°. Using Eq. 8.7 and the parameters in Table 8.2, $\vartheta_{m,max} = 64.29°$. The controller should modify ϑ_m within the range of $[-\vartheta_{m,max}, \vartheta_{m,max}]$ based on the biped pitch angle and pitch angular velocity. Equation 8.9 defines the control law for ϑ_m, with ϕ fixed at 0°, where

κ defines the direction and intensity of the control action, K_p (unitless) and K_v (units: sec) are non-dimensionalizing gains for the pitch angle and pitch angular velocity with units rad and rad/s, respectively, and 'sat' is the unit saturation function, such that κ falls within [-1, 1]. In this simulation, $K_p = 10$ and $K_v = 1$ sec.

$$\vartheta_m = \vartheta_{m,max}\kappa \quad , \quad \kappa = -\text{sat}\left(K_p\gamma + K_v\dot{\gamma}\right) \tag{8.9}$$

Figure 8.6 shows the behavior of the system with and without compensation from the tail for a disturbance $|\Delta M| = 15$ N-m for $t = 0.5$ sec. Without tail compensation, the destabilizing moment is sufficient to tip the COM over the revolute joint, fully destabilizing the system, starting at $|\Delta M| = 14.7$ N-m. For $|\Delta M| = 15$ N-m, with tail compensation, the tail bends forward in the $-y$ direction, compensating for the destabilizing moment in the $+y$ direction. This motion modifies the tail's loading applied to the biped in M_B such that the disturbance only causes a slight pitch of the system before it falls back to a stable configuration. For the gains K_p and K_v chosen, the maximum magnitude of κ is -0.411; meaning that the controller did not have to drive the tail to its maximum position in order to stabilize for this disturbance.
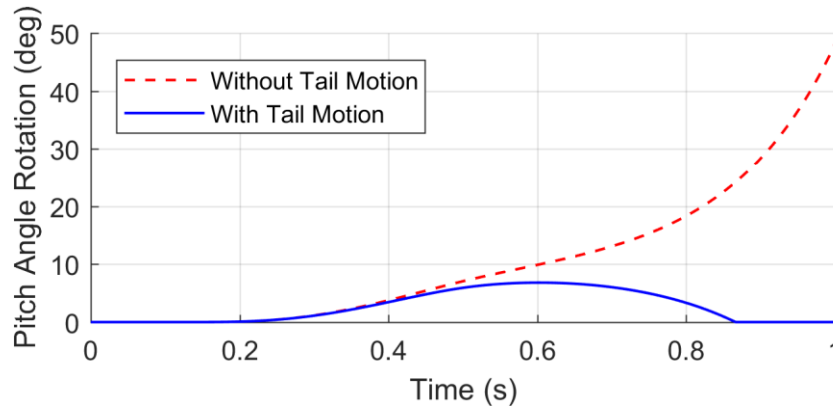
Figure 8.6: Pitch angle stabilization of the biped with DMST.

The maximum disturbance magnitude these control gains can accommodate is 20.4 N-m, representing a 39% increase in maximum allowable disturbance magnitude with respect with the destabilizing moment of 14.7 N-m. If the tail is held fixed at $\vartheta_m = -\vartheta_{m,max}$ throughout the full simulation, the maximum disturbance magnitude it can accommodate is $|\Delta M| = 24.8$ N-m, which

represents the theoretical maximum disturbance this tail can reject based on gravitational loading given the biped and tail geometry and mass distribution.

8.2.2 Maneuvering: Quasi-Static Stable Forward Walking Gait

In this section, dynamics simulations are performed to investigate the proposed mechanism's ability to stabilize the robotic system shown in Fig. 8.4 during a walking gait. The Solidworks CAD model of the robotic system was exported to MSC ADAMS [129], a physics-based multi-body dynamics simulation software. ADAMS is able to calculate the absolute motions of all bodies subject to torques applied on the joints by virtual actuators while taking into account the mass, inertia, body accelerations and contact/frictional forces between the feet and ground.

In this investigation into gait stabilization to enable maneuvering in the form of forward walking, the robotic system's COM is used as a stability criteria to calculate the tail trajectory required to stabilize the biped robot during a walking gait. This criteria states that the horizontal projection of the COM should fall within the biped robot's support polygon defined as the convex hull generated by the contact points of the feet to ensure a stable quasi-static walking gait [130]. To evaluate this criteria, Eqs. 8.11 are used to compute the combined robotic systems COM, p_{COM}, with reference to variables defined in section 5.1

$$
\begin{aligned}
p_{T,COM,lcl} &= \frac{\sum_{i=0}^{n} m_i p_{i,COM}}{m}, \\
m_T &= m_0 + \sum_{i=1}^{n} m_i, \quad p_{T,COM} = p_{JD} + R_B \, p_{T,COM,lcl}, \\
p_{COM} &= \frac{m_B p_{JB} + m_T p_{T,COM}}{m_B + m_T}
\end{aligned}
\tag{8.11}
$$

Where $p_{T,COM}$ is the DMST tail COM defined in the J frame (Fig. 8.5), m_T is the total mass of the DMST. The largest displacements of tail COM away from its base occurs at $\vartheta_{m,max} = \pm\, 64.29°$. Using simulation parameters presented in Table 8.2, rotating the tail by $\pm\, \vartheta_{m,max}$ approximately centers p_{COM} within the single support polygon of the left and right foot. The roll DOF was used to keep p_{COM} within the single support polygon as the robot performs a walking gait with a 150 mm step length. Figure 8.7 depicts the dynamic simulation of the biped robot performing a stable

quasi-static forward walking gait enabled by the DMST. Using this method, the biped robot can also balance its self on one support polygon using the tail as a counter balance to enable differential turning by generating a gait trajectory with the opposing foot. Therefore, using tail-aided motion the combined robotic system can satisfy all walking criteria mentioned in section 6.2
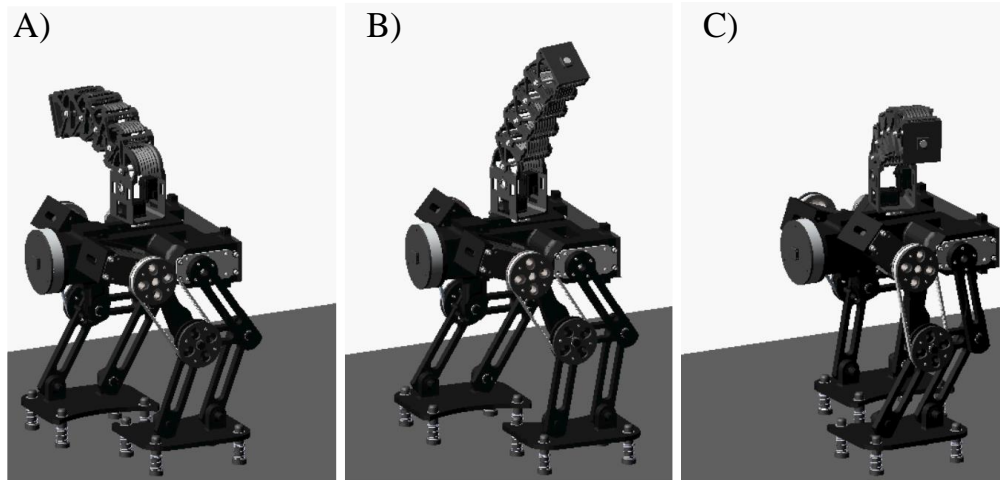
Figure 8.7: Dynamic simulation depicting the DMST stabilizing a planar biped robot performing a quasi-static stable forward walking gait: A) left support phase, B) double support phase, and C) right single support phase.

8.3 Conclusion

This chapter demonstrated that the combined robotic systems consisting of robotic tails, R3-RT and DMST, attached to a reduced-DOF quadruped and biped legged robotic platform; respectively, can satisfy comparable walking criteria with respect to conventional legged robots [104] that include: (1) maintain quasi-static stability during locomotion, (2) maintain a constant robot body height during a waiting gait, (3) maintain horizontal body orientation during a walking gait, and (4) have the ability to move backward, forward and (5) steer. Furthermore, the tail onboard the legged robots were used to provide compensatory tail motions to reject external disturbances during walking gaits to further enhance stability.

In section 8.2.1, experiments using the R3-RT attached to a virtual quadruped robot were evaluated to demonstrate maneuvering case scenarios using tail aided motion defined by the control approach in section 7.3.4. Results indicated that the R3-RT can maneuver the quadruped up to a yaw angle of 20° within its allowable workspace with an RMS error of 5.14°. For the

remaining case scenarios $\theta_d = 10°$ and 5°, since the tail produced motions with less angular displacements, the legged robot angular roll and pitch variation during the airborne phase is decreased due to less unbalanced gravitational loading effects at the tail's final configuration which results in the quadruped landing in a more symmetric configuration; thus, reducing the undesirable effects of ground impact. It is for this reason the RMS error decreases with a reduction of θ_d. Future work will investigate articulated tail motion in combination with tail roll motion to reduce the effects of undesirable pitch and yaw motions of the legged robot during maneuvering applications for a smoother landing to minimize the yaw angle RMS error of the legged robot. To demonstrated enhanced stabilization using tail motion, a harmonic oscillator was utilized to control the R3-RT prototype to reject disturbances about the roll axis. Experimental results demonstrated that the tail can reject disturbances of up to 30.2 Nm. This enables the quadruped to reject an external disturbance of up to 20% more magnitude in tail controlled mode with respect to gravitational loading of the quadruped that can reject disturbances of up to 25.6 Nm in uncontrolled mode.

In section 8.2.2, simulation based case studies on the DMST attached to a biped configuration demonstrated how the tail can be used for enhanced stabilization for pitch-angle disturbance rejection while standing and maneuvering to enable a quasi-static stable forward walking gait. Without tail compensation, the destabilizing moment sufficient to tip the biped over is equivalent to 14.7 N-m. With tail motion, the maximum disturbance magnitude the system can accommodate is 20.4 N-m, representing a 39% increase in maximum allowable disturbance magnitude with respect with the destabilizing moment of 14.7 N-m. Furthermore, the DMST enabled the inherently unstable biped configuration to walk forward with a stable quasi-static gait where the biped provides forward propulsive motion during the single support phases where the tail was swung over the left or right foot, to adjust the combined system's COM above the support polygon. Using this method, the biped robot can also balance its-self on one support polygon using the tail as a counter balance to enable differential turning by generating a gait trajectory with the opposing foot.

CHAPTER 9: CONCLUSION

This chapter concludes the dissertation with a summary of the technical contributions and results, with a forward looking discussion into prospective research that has been established as an outcome of the achievements presented in this dissertation.

9.1 Summary of Research Contributions

In nature, animals commonly use their tails to assist propulsion, stabilization, and maneuvering. However, in legged robotic systems, the dominant research paradigm has been to focus on the design and control of the legs as a means to simultaneously provide propulsion, maneuvering, and stabilization. Fundamentally, this research is motivated by the question of how to improve the stability and maneuverability of legged robots utilizing an articulated tail mechanism. It is hypothesized that by using an articulated tail mechanism to aid in these functionalities onboard a legged robots, the burden on the robot's legs to simultaneously maneuver and stabilize the robot may be reduced. This could allow for simplification of the leg's design and control algorithms.

This doctoral dissertation addressed this problem statement and hypothesis by proposing two articulated tail mechanisms, R3-RT and DMST, that are uniquely designed to be practically implemented on a reduced DOF quadruped and biped robot, respectively, for tail-aided stabilization and maneuverability. The articulated tails enable enhanced workspace and inertial loading capabilities relative to pendulum-like tails while the proposed leg mechanism enables the construction of legged robots with simplified design and control; however, these legged robots cannot effectively walk as standalone machines which justifies the implementation of articulated tails for augmented performance. Using experiments and simulations, the combined robotic systems consisting of a reduced DOF quadruped and biped robots augmented via articulated tails, demonstrate walking criteria that is comparable to conventional legged robots. The summary of research contributions are stated as follows:

Chapter 2 justified the use of robotic tails onboard mobile robots for inertial adjustment applications relative to existing technologies and reviews state-of-the-art contributions regarding robotic tail implementation. Since the earliest implementation of a robotic tails dating back to 1991, all designs revolved around the concept of single-body rigid pendulums. However, recent research [21] investigating increased articulation in tail structures using mathematical modeling and simulation has shown promise to enhance inertial loading capabilities. This work has instigated the research into articulated tail designs proposed in this paper.

Chapter 3 presented two novel articulate tail designs, the R3-RT and DMST, which represent a centralized and modular approach for tail implementation onboard legged robots. The proposed mechanisms share common design novelties. Circular contoured tail linkages with constant radii are used to rout cables and maintain equal antagonistic cable displacements; therefore, enabling a single articulated tail segment to be actuated using a single driving pulley. Infinite roll rotation enables the proposed designs to function as both symmetric and asymmetrical rotational based inertial adjustment mechanisms. All existing pendulum-like tails can only function as asymmetrical inertial adjustment mechanisms. The S-shaped cable routing scheme of the R3-RT enables the formation of two distinct tail curvatures using two mechanically decoupled actuated segments.

Chapter 4 presented the modeling, analysis, and experimental results of the R3-RT tail design. Work space analysis of the R3-RT demonstrated a three-dimensional end effector and COM workspace that represents a significant performance advantage relative to existing tail designs. For pendulum-like tails, the locus of points along which the end effector and COM can move is constrained to spheres with a fixed radius. The dynamic loading model was derived and simulated to analyze and better understand the impact of tail motion and tail configuration on generated inertial loading.

Experiments were performed to compare the inertial loading of an articulated tail structure relative to a single-body rigid pendulum. The R3-RT was reconfigured into: 1) articulated single DOF tail segment, and 2) a single-body rigid pendulum structure. The two configurations were actuated in a single plane with constant input force and an equivalent pulley displacement with generated inertial loading measured using a six-axis load cell. On average the articulated tail, relative to the pendulum-like structure, provides: a 53% increase in generated moment about the base, and a 46% net reduction in forces. Increased inertial moments result in enhanced inertial

loading capabilities onboard a legged robot that produce greater angular re-orientation which is beneficial for maneuvering and stabilization applications. Decreased inertial forces is also beneficial because forces cause system translation and may either aid or hinder inertial adjustment applications based on the legged robot state.

Experimentally measured peak loading profile values equal to 6 N and 3.1 N-m fall slightly below computed values using the dynamic loading model because the experimental tail motion duration was slightly longer than the 0.5 s time span used in simulation based studies.

The R3-RT can produce tail configurations with an accuracy and repeatability of 1.4±5.1° for segment 1 and 10.5±6.7° for segment 2. This performance is attributed to the challenges of practical implementation of cable routing that are not nested perfectly along the link's cylindrical surfaces that cause slight variations of equal and opposite cable extension and retraction coupled with error accumulation over the joints.

Chapter 5 presented the modeling, analysis, and experimental results of the DMST tail design. Results of kinematic workspace analysis have demonstrated that the DMST produced a lesser dimensionality end effector and COM workspace in comparison to the R3-RT, presented in Chapter 4, due to less articulation and its ability to form one tail curvature. However, higher dimensional workspaces are achievable for multiple DMST modules connected in series, a concept presented in section 3.4 but not practically implemented as part of this research. These results further emphasized the importance of increased articulation and multi-curvature tail configuration shapes that can produce a higher dimensionality end effector workspace and a greater ability to adjust its COM location which is important for both dynamic inertial adjustment and static stabilization applications, as discussed in section 4.2.1.

A dynamic loading model was derived to analyze the loading generated by the tail in response to variations in trajectory and design parameters. Dynamic force loading analysis concluded that force loading profiles can be distributed about three axes by varying roll angle and magnified by: (1) reducing the time span of tail motions, (2) allocating a larger mass distribution at the tip of the tail while considering spool torque requirements to produce tail curvature, and (3) increasing coupling ratios of bottom segments adjacent to the tail base. Experimental results were used to validate the dynamic loading model.

Experimentally measured peak loading profile values, equal to 6 N and 1.8 N-m, fell below computed values using the dynamic loading model because the experimental tail motion duration

was slightly longer than the 0.2 s time span used in computed results. This is expected since as the time spans of tail motions are lengthened, dynamic loadings decrease towards steady state gravitational loading conditions.

Experimental results indicated that the DMST exhibits satisfactory accuracy and repeatability measured to be 3.1±0.8°. These results show better accuracy and repeatability in comparison to the R3-RT that can be attributed to the use of nylon coated steel braided wire with swaged ball bearing ends as described in section 3.4; while the R3-RT utilizes nylon braided cables that are secured at its ends using a screw and nut mechanism.

Chapter 6 presented a novel reduced-DOF modular leg mechanism used to construct legged robots, quadrupeds and bipeds, with simplified design and control to be used as experimental platforms to assess the attached articulated tails ability to augment performance.

The 2-DOF RML mechanism novelties stem from its construction using two serially connected four-bar mechanisms that are mechanically decoupled and can maintain a parallel flat foot orientation without the use of an actuated ankle. A passive suspension system integrated into the ankle is capable of maintaining a four point of contact support polygon on both flat and unstructured terrain. A foot trajectory is generated to minimize impulsive forces during a walking gait. A proof-of-concept prototype is integrated to evaluate the performance in accurately tracking a foot trajectory. Errors are minimized to 1.2° with a standard deviation of ±1.1° through a series of iterations that result in a maximum deviation of 5.2 mm from the desired trajectory. However, since the RML is a planar leg mechanism, the resultant quadruped configuration cannot maneuver (turn) or stabilize itself and the biped configuration cannot satisfy produce a stable walking gait or maneuver; thus, justifying the implementation of articulated tails to augment performance in terms of maneuvering and stabilization.

Chapter 7 presented dynamic modeling of a generic robotic system design consisting of an articulated tail and legged robotic system. This generic model is applied to the quadruped and R3-RT to derive the dynamic models to analyze an optimal tail mass and length ratio to enhance inertial adjustment applications. Results of analytical optimization are corroborated with measured data from biological animals. Using the proposed dynamic formulation, a maneuvering controller was proposed that consists of a Path Planner controller to plan tail trajectories for goal oriented maneuvering behavior and a Tail Motion controller to track the planned tail trajectory.

142

Chapter 8 presented experiments and simulations of the combined robotic system. Virtual models of the quadruped and biped robots were built using MSC ADAMS, a multi-body-dynamic physics simulator. Experiments were used to evaluate maneuverability and stabilization of a virtual quadruped robot using tail motions for the R3-RT prototype. Multi-body dynamic simulations of the DMST onboard a biped robot demonstrate the tails ability to enable a quasi-static gait and enable left and right turning. The quadruped robot augmented with the R3-RT and the biped robot augmented with the DMST demonstrate walking conditions [104] comparable to conventional legged robots that include: 1) maintaining quasi-static stability during motion, 2) maintaining a constant robot body height during a waiting gait, 3) maintaining horizontal body orientation during a walking gait, and 4) having the ability to move backward, forward and 5) steer.

9.2 Future Research Directions

This doctoral work established one of the first investigations into articulated tail mechanisms and their implementation onboard legged robots to enable design and control simplifications and augmented performance capabilities. This dissertation laid the foundations for developing a robust legged robotic system augmented via a tail, and for the future work that ensues as a result of the contributions derived from this research. For a better understanding of future research directions, the objectives that remain to be addressed in terms of articulated tail design, modeling and control of the combined robotic system (legged robots with attached tails) are discussed in this section.

9.2.1 Articulated Tail Design Objectives

The performance of robotic tails is highly dependent on its mechanical design. To date, with reference to Table 2.1, tail designs have evolved from planar to spatial pendulums and most recent progress, as a result of the contributions of this dissertation, has shifted to articulated, spatial mechanisms. These advancements have been coupled to enhanced workspace, functionalities, and inertial loading capabilities for more desirable effects of inertial adjustment applications. However, there still remains potential for design advancements to realize the full set of functionalities of biological tail usage as observed in nature that involve tasks of inertial adjustment and manipulation. For instance, the proposed tail mechanisms generate a 2-dimensional planar tail curvature and distribute inertial loading via a roll revolute joint; whereas, biological tails are capable of forming 3-dimenaional spatial curvatures in the absence of a physical joint for roll

143

mobility. Although this dissertation investigated the performance of two unique articulated tail mechanisms, an optimal and general purpose tail design has yet to be proposed. The fundamental challenges that govern this problem include:

- Design optimization and considerations on the minimal number of active DOF's and structural configuration required to produce a spatial workspace with distributed motion about its tail length for enhanced inertial loading capabilities. The added mass of the actuators contributes a change to system dynamics and is directly related to the cost inertial adjustment capabilities.

- Limits on strength, and precision of the tail mechanism that can perform both dynamic motions for inertial adjustment applications and provide the accuracy required for quasit-static applications that involve precise COM positioning for static stabilization and manipulation.

- Limits on motor power, and energy efficiency to maintain a cantilevered configuration with minimal energy consumption.

9.2.2 Modeling and Control Objectives

Although modeling and control approaches have been developed and implemented over a wide range of applications, inertially adjusting a legged robot using a robotic tail is a challenging task due to modeling of a highly coupled, nonlinear dynamic, under actuated system. Since the tail attachment point to a mobile robot is usually located at its rear end, offset from the robot COM, during inertial adjustment applications, tail motions generate both a reactive moment and lateral forces, caused by eccentric mass distribution of the tail that are transferred to the mobile robot. These forces also induce a moment due to this positional offset that introduces challenges in modeling and control. Depending on the state at each instant, this may either augment or diminish the resultant moment produced by the tail, complicating analysis considerably. This problem requires optimization to find good control policies. To address these challenges, common methods employed by researchers include simplifying assumptions that have neglected the effects of inertial forces [6, 31, 33, 40, 44, 46-49] on the mobile robot and have constrained the robotic system dynamics to a single plane [35-37], or have neglected the effects of leg/wheels motion in the

dynamic model [31, 34, 44, 47-49]. The challenges that remain to be addressed both in low-level control and high-level planning to overcome realistic constraints include:

- Developing a dynamic model of a legged robotic system with a tail attached that accounts for variations of inertial properties due to leg and tail motions with ground contact.
- Developing algorithms for maneuvering that also account for the stability of the system that may be compromised during tail motions.
- Developing algorithms for computing an optimal tail trajectory with a constrained workspace that considers the effects of both inertial forces and moments to maximize desirable effects of inertial adjustment.

The objectives outlined in this concluding chapter are founded on the scientific infrastructure established in this dissertation, where the synthesis of the current and prospective work will ultimately culminate into an intelligent legged robotic system that is capable of robust locomotion where stabilization, maneuverability, and manipulation are enabled via an articulated tail mechanism to fully encompass the benefits that biological tails provide animals.

APPENDIX A: NOMENCLATURE

This appendix details the nomenclature of the acronyms (Table A.1), marks and symbols (Table A.2), and variables (Table A.3) used throughout the paper for the analyses of the articulated tails, legged robot, and dynamic formulations.

Table A.1: Nomenclature, Acronym and Definition

Acronym	Definition
COM	Center-of-Mass
DOF	Degree-Of-Freedom
DMST	Discrete Modular Serpentine Tail
MDP	Multi-Diameter Pulley
R3-RT	Roll-Revolute-Revolute Tail
RML	Robotic Modular Leg

Table A.2: Nomenclature, Marks and Symbols

Mark	Meaning	Symbol	Meaning
$|\mathbf{x}|$	Euclidean norm of $\mathbf{x}$	$\times$	Cross product
$\dot{\mathbf{x}}$	First time Derivative of $\mathbf{x}$	sgn	Signum function
$\ddot{\mathbf{x}}$	Second time Derivative of $\mathbf{x}$	sat	Unit saturation function
$\mathbf{x}^{\mathrm{T}}$	Transpose of $\mathbf{x}$		
$\tilde{a}b$	$a \times b$		

<div align="center">**Table A.3:** Nomenclature, Variable and Description</div>

Variable	Description
$a_{k,i}$	i-th order term coefficient for segment k for trajectory generation
$\boldsymbol{a}_{i,jnt}$	Linear acceleration of link joint i
$\boldsymbol{a}_{i,COM}$	Linear acceleration of link joint i
B_i	Body i
$\boldsymbol{C}$	Coriolis and centripetal effects matrix for the equations of motion
C1, C2, C3	Tail configurations
$\mathbf{e}$	Euler parameters for rigid bodies in RML mechanism
F_f	Friction force magnitude between legged robot feet and ground
$\boldsymbol{F}_B = [F_{B,x}, F_{B,y}, F_{B,z}]$	Inertial forces generated about tail base
$\boldsymbol{F}_{F,grv}$	Rigid housing's gravitational loading of R3-RT
$\boldsymbol{F}_{i,grv}$	Gravitational force loading about joint i for R3-RT and DMST
$\boldsymbol{F}_{i,inr}$	Inertial force loading about joint i for R3-RT and DMST
$\mathbf{F}$	Forcing function associated with the external forces for RML
F_t	Tangential force magnitude component exerted on the tail by the quadruped
F_r	Radial force magnitude component exerted on the tail by the quadruped
$\boldsymbol{F}_{jnt}$	Force at ground joint of biped robot toe
$\boldsymbol{F}_{toe}$	Force at biped robot toe with the ground
$\boldsymbol{F}_{B,grv}$	Gravitational force of biped robot
$\boldsymbol{g}$	Gravitational loading vector for the equations of motion
g	Gravitational acceleration magnitude
$\boldsymbol{H}_O$	Total angular momentum of combined legged robot and tail system about point O
$\boldsymbol{I}_i$	Link i moment of inertia with respect to the global frame
$\boldsymbol{I}_{i,lcl}$	Link i local moment of inertia with respect to the link i frame
$\boldsymbol{I}_B$	Biped moment of inertia
$\boldsymbol{J}_i$	Joint i in the RML
$\boldsymbol{J}$	Block diagonal matrix of the link inertia tensors for RML
K_p	Proportional gain
K_i	Integral gain
K_d	Derivative gain
L_{J2J}	Distance between two adjacent joints for R3-RT and DMST
L_{J2C}	Distance between a joint and its COM for R3-RT and DMST
$L_{J2C,n}$	Distance between joint n and the link n COM for R3-RT and DMST
$L_{J2J,0}$	Distance from joint 0 to joint 1 for R3-RT and DMST
$L_{J2C,0}$	Distance from joint 0 to the link 0 COM for R3-RT and DMST
l_H	Hip Length for RML
l_S	Shin Length for RML
l_K	Knee Length for RML
M_a	Tail input torque magnitude
$\boldsymbol{M}$	Mass matrix for equations of motion

$\boldsymbol{M}_M$	Block diagonal mass matrix for RML
$\boldsymbol{M}_{i,jnt}$	Net moment about joint i
$\boldsymbol{M}_{i,grv}$	Gravitational loading about joint i
$\boldsymbol{M}_{i,inr}$	Inertial loading about joint i
$\boldsymbol{M}_{i,gear}$	Gear loading about joint i
$\boldsymbol{M}_{i,act}$	Actuation loading about joint i
$\boldsymbol{M}_B = [M_{B,x}, M_{B,y}, M_{B,z}]$	Inertial moments generated about tail base
$\boldsymbol{M}_{jnt}$	Moment at ground joint of biped robot toe
$\Delta\boldsymbol{M}$	Impulse magnitude of destabilizing moment
ΔM	Impulse magnitude of destabilizing moment magnitude
m	Total system mass of combined legged robot and tail
m_i	Mass of rigid body i
m_F	Mass of the rigid housing of R3-RT
M_f	Friction moment magnitude between legged robot feet and ground
m_B	Biped mass
$\mathbf{n}$	Forcing functions associated with external moment acting on RML
n	Link number in an articulated tail
n_{pair}	Number of leg pairs in a legged robot
$\boldsymbol{p}_{i,jnt}$	Link i joint positions
$\boldsymbol{p}_{i,COM}$	Link i COM positions
$\boldsymbol{p}_{0,COM,lcl}$	Local position vector from joint 1 to the link 0 COM
$\boldsymbol{p}_{0,jnt,lcl}$	Local position from the global coordinate frame to joint 0
$\boldsymbol{p}_{1,jnt,lcl}$	Local position from joint 0 to joint 1
$\boldsymbol{p}_{i,j,J2C}$	Position vector from joint i to the link j COM
$\boldsymbol{p}_{F,COM}$	Position vector of the rigid housing COM relative to the R3-RT base frame
$\boldsymbol{p}_{COM}$	Combined robotic system, tail and legged robot, COM location
$\boldsymbol{p}_{i,j,CJ}$	Position vector from the link i COM to joint j
$\boldsymbol{p}_{HF} = [\,p_{HF,x}, p_{HF,z}\,]$	Position vector from the hip frame to the foot frame for RML
$\mathbf{p}$	Cartesian positions of body links for RML
$\mathbf{P}_i$	Position vector locating the point mass i
$\boldsymbol{p}_{JB}$	Position vectors from the origin of frame J to point B
$\boldsymbol{p}_{JD}$	Position vectors from the origin of frame J to point D
$\boldsymbol{p}_{BT}$	Position vectors from the origin of frame B to point T
$\boldsymbol{p}_{JB,lcl}$	Local position vector from the origin of frame J to point B
$\boldsymbol{p}_{JD,lcl}$	Local position vectors from the origin of frame J to point D
$\boldsymbol{p}_{BJ}$	Position vector from the frame B origin to frame J
$\boldsymbol{p}_{BD}$	Position vector from the frame B origin to frame D
q	State variable vector
r_{cbl}	Radius of the cylindrical contoured link
$\boldsymbol{R}_i$	Orientation matrix of link i for articulated tail mechanism
$\boldsymbol{R}_B$	Orientation matrix of Biped robot

T_k	k-th cable tension
$T_{i,j}$	Cable tension at joint i of the cable terminating at link j
T_s	Time period of a single gait cycle
t	Simulation time
t_0	Simulation start time
t_f	Simulation end time
$\boldsymbol{u}$	Actuation input for the equations of motion
$\boldsymbol{v}_i$	Velocity of mass i
$\boldsymbol{v}_{i,jnt}$	Velocity vector of joint i
$\boldsymbol{v}_{i,COM}$	Velocity vector of link COM i
$\boldsymbol{x}_c$	X-component of legged robot and tail COM location
$\boldsymbol{y}_c$	Y-component of legged robot and tail COM location
$\bar{\theta}_i$	Left (L) or right (R) cable displacement
ς_i	Axis of rotation of joint i in R3-RT
δ_k	k-th cable displacements in R3-RT
$\beta_{seg,k}$	Input pulley rotation driving segment k of the R3-RT
$\beta_{d,seg,k}$	Desired input pulley rotation driving segment k of the R3-RT
$\beta_{seg,k,0}$	Segment pulley angle initial value for R3-RT
$\beta_{seg,k,f}$	Segment pulley angle final value for R3-RT
β	Pendulum tail relative angle with respect to legged robot angle θ
β_0	Initial pendulum tail relative angle
β_f	Final pendulum tail relative angle
β_i	Relative i-th link rotation in an articulated tail
β_1	Relative link rotation in segment 1 of R3-RT
β_2	Relative link rotation in segment 2 of R3-RT
φ	Roll DOF of R3-RT
φ_0	Roll angle initial value for R3-RT
φ_f	Roll angle final value for R3-RT
τ	Roll DOF torque of R3-RT
$\boldsymbol{\tau}_r$	Roll DOF torque of DMST
τ_s	MDP drive torque required for DMST
$\boldsymbol{\zeta}_{grv}$	Unit vector along which gravity acts
ε	Maximum threshold of tail angular velocity
Ω	Maximum threshold of tail angular acceleration
$\boldsymbol{\omega}_i$	Angular velocity of body i
$\bar{\mu}$	Mean
$\bar{\sigma}$	Standard Deviation
σ	Mass ratio between the of the summation of the articulated tail linkage masses with respect to the legged robot and tail actuation unit mass
λ	Length ratio between the total articulated tail length with respect to distance between the legged robot COM and the tail attachment point
r_i	Multi-diameter pulley radius of DMST

θ	Legged robot angle
ϑ_i	Relative link rotation of link i in a segment
θ_d	Desired legged robot angular orientation
$\tilde{\theta}$	Estimated legged robot angular orientation
$\bar{\theta}_i$	Mean measured global orientation of link i
θ_H	Hip Angle of RML
θ_S	Shin Angle of RML
ϑ_m	Input angle to DMST MDP
$\vartheta_{m,max}$	Input angle to DMST MDP that corresponds to the configuration that generates the maximum pitch gravitational moment
η_i	Coupling ratio in an articulated tail
μ	Coefficient of friction
ϕ	Roll- DOF of DMST
ϕ_m	Motor input angle for Roll- DOF of DMST
m	DMST mass distribution ratio
χ_i	Link i contact angle between the cable and routing surfaces
ρ	Quadruped roll angle
ρ_b	Roll angle boundary of the quadruped that does not require tail input compensation
ρ_{lim}	Roll angle limit of the quadruped beyond which results in full tail compensation
ψ	Parameterization variable of roll DOF φ of the R3-RT mechanism
κ	Forcing function for tail compensation
ξ	Dampening ratio
ω_n	Natural frequency
$\boldsymbol{\omega}_B$	Angular velocity of Biped robot along pitch direction
$\boldsymbol{\Phi}_p$	Jacobian of Constraint vector for RML with respect to Cartesian parameters
$\boldsymbol{\Phi}_e$	Jacobian of Constraint vector for RML with respect to Euler parameters
$\boldsymbol{\Phi}$	Constraint vector for RML
γ	Acceleration-independent terms associated with twice differentiating the constraint vector $\boldsymbol{\Phi}$
λ	Lagrange multipliers associated with the two angle driver constraints correspond to the torque required to actuate RML joints

REFERENCES

[1]   G. C. Hickman, "The mammalian tail: a review of functions," *Mammal Review,* vol. 9, pp. 143-157, 1979.

[2]   A. B. Howell, "Speed in animals, their specialization for running and leaping," *American Journal of Physical Anthropology,* vol. 3, pp. 109-110, 1944.

[3]   M. J. Benton, "Studying function and behavior in the fossil record," *PLoS Biology,* vol. 8, p. e1000321, 2010.

[4]   U. Proske, "Energy conservation by elastic storage in kangaroos," *Endeavour,* vol. 4, pp. 148-153, 1980.

[5]   J. L. C. Santiago, I. S. Godage, P. Gonthina, and I. D. Walker, "Soft Robots and Kangaroo Tails: Modulating Compliance in Continuum Structures Through Mechanical Layer Jamming," *Soft Robotics,* vol. 3, pp. 54-63, 2016.

[6]   A. M. Johnson, T. Libby, E. Chang-Siu, M. Tomizuka, R. J. Full, and D. E. Koditschek, "Tail assisted dynamic self righting," *World Scientific,* 2012.

[7]   T. Libby, T. Y. Moore, E. Chang-Siu, D. Li, D. J. Cohen, A. Jusufi*, et al.*, "Tail-assisted pitch control in lizards, robots and dinosaurs," *Nature,* vol. 481, pp. 181-184, 2012.

[8]   H. W. Greene, G. M. Burghardt, B. A. Dugan, and A. S. Rand, "Predation and the defensive behavior of green iguanas (Reptilia, Lacertilia, Iguanidae)," *Journal of Herpetology,* pp. 169-176, 1978.

[9]   T. L. Hedrick and A. Biewener, "Low speed maneuvering flight of the rose-breasted cockatoo (Eolophus roseicapillus). I. Kinematic and neuromuscular control of turning," *Journal of Experimental Biology,* vol. 210, pp. 1897-1911, 2007.

[10]   T. Kane and M. Scher, "A dynamical explanation of the falling cat phenomenon," *International Journal of Solids and Structures,* vol. 5, pp. 663IN1667-666IN2670, 1969.

[11]   M. Pijnappels, I. Kingma, D. Wezenberg, G. Reurink, and J. H. van Dieën, "Armed against falls: the contribution of arm movements to balance recovery after tripping," *Experimental brain research,* vol. 201, pp. 689-699, 2010.

[12]   L. S. Crawford and S. S. Sastry, "Biological Motor Control Approaches for a Planar Diver," in *Conference on Decision and Control*, 1995, pp. 3881-3886.

[13]   W. Saab, W. Rone, and P. Ben-Tzvi, "Robotic Tails: A State of The Art Review," *Robotica (submitted Nov. 2017),* 2018.

[14]   W. Saab, W. Rone, A. Kumar, and P. Ben-Tzvi, "Design and Integration of a Novel Spatial Articulated Robotic Tail," *Transactions on Mechatronics (submitted Oct. 2017),* 2018.

[15]   W. Rone and P. Ben-Tzvi, "Dynamic Modeling and Simulation of a Yaw-Angle Quadruped Maneuvering With a Planar Robotic Tail," *Journal of Dynamic Systems, Measurement, and Control,* vol. 138, p. 084502, 2016.

[16]   W. Saab and P. Ben-Tzvi, "Design and Analysis of a Discrete Modular Serpentine Robotic Tail for Improved Performance of Mobile Robots," in *International Design Engineering Technical Conferences and Computers and Information in Engineering Conference* Charlotte, NC, 2016, pp. V05AT07A061: 1-8.

[17]   W. Saab, W. Rone, and P. Ben-Tzvi, "Discrete Modular Serpentine Robotic Tail: Design, Analysis and Experimentation," *Robotica* pp. 1-25, 2018.

[18]   W. Saab, W. Rone, and P. Ben-Tzvi, "Robotic Modular Leg: Design, Analysis and Experimentation," *Journal of Mechanisms and Robotics,* vol. 9, pp. 024501: 1-6, 2016.

[19]   W. Saab and P. Ben-Tzvi, "Design and Analysis of a Robotic Modular Leg," in *International Design Engineering Technical Conferences and Computers and Information in Engineering Conference* Charlotte, NC, USA, 2016, pp. V05AT07A062: 1-8.

[20]   W. Saab, Y. Jiteng, and P. Ben-Tzvi, "Modeling and Control of an Articulated Tail for Maneuvering a Reduced Degree of Freedom Legged Robot," in *International Conference on Intelligent Robots and Systems (Submitted March 2018)*, 2018.

[21]   W. Saab and P. Ben-Tzvi, "Maneuverability and Heading Control of a Quadruped Robot Utilizing Tail Dynamics," in *Dynamic Systems and Control Conference*, Va, USA 2017, pp. V002T21A010: 1-7.

[22]   H.-o. Lim, Y. Kaneshima, and A. Takanishi, "Online Walking Pattern Generation for Biped Humanoid Robot with Trunk," in *IEEE International Conference on Robotics and Automation*, 2002, pp. 3111-3116.

[23]   K. Harada, S. Kajita, K. Kaneko, and H. Hirukawa, "Zmp Analysis for Arm/Leg Coordination," in *International Conference on Intelligent Robots and Systems*, 2003, pp. 75-81.

[24] E. Papadopoulos and D. A. Rey, "A New Measure of Tipover Stability Margin for Mobile Manipulators," in *IEEE International Conference on Robotics and Automation*, 1996, pp. 3111-3116.

[25] S. K. Gupta, W. Bejgerowski, J. Gerdes, J. Hopkins, L. Lee, M. S. Narayanan*, et al.*, "An Engineering Approach to Utilizing Bio-Inspiration in Robotics Applications," in *Biologically Inspired Design*, ed: Springer, 2014, pp. 245-267.

[26] J. R. Wertz, "Spacecraft attitude determination and control." vol. 73, ed Springer Netherlands: Springer Science & Business Media, 2012.

[27] G. C. Oates, "Aircraft propulsion systems technology and design," ed Portland, OR: Aiaa, 1989.

[28] S.-H. Lee and A. Goswami, "Reaction Mass Pendulum (RMP): An Explicit Model for Centroidal Angular Momentum of Humanoid Robots," in *IEEE International Conference on Robotics and Automation*, 2007, pp. 4667-4672.

[29] M. D. Carpenter and M. A. Peck, "Reducing base reactions with gyroscopic actuation of space-robotic systems," *IEEE Transactions on Robotics,* vol. 25, pp. 1262-1270, 2009.

[30] K. Machairas and E. Papadopoulos, "On Quadruped Attitude Dynamics and Control Using Reaction Wheels and Tails," in *European Control Conference*, 2015, pp. 753-758.

[31] R. Briggs, J. Lee, M. Haberland, and S. Kim, "Tails in Biomimetic Design: Analysis, Simulation, and Experiment," in *International Conference on Intelligent Robots and Systems* Vilamoura-Algarve, Portugal, 2012, pp. 1473-1480.

[32] A. Patel and E. Boje, "On the Conical Motion of a Two-Degree-of-Freedom Tail Inspired by the Cheetah," *IEEE Transactions on Robotics,* vol. 31, pp. 1555-1560, 2015.

[33] A. Patel and M. Braae, "Rapid Turning at High-Speed: Inspirations from the Cheetah's Tail," in *IEEE/RSJ International Conference on Intelligent Robots and Systems*, 2013, pp. 5506-5511.

[34] A. Jusufi, D. Kawano, T. Libby, and R. Full, "Righting and turning in mid-air using appendage inertia: reptile tails, analytical models and bio-inspired robots," *Bioinspiration and Biomimetics,* vol. 5, p. 045001, 2010.

[35] G.-H. Liu, H.-Y. Lin, H.-Y. Lin, S.-T. Chen, and P.-C. Lin, "A bio-inspired hopping kangaroo robot with an active tail," *Journal of Bionic Engineering,* vol. 11, pp. 541-555, 2014.

[36] A. De and D. E. Koditschek, "The Penn Jerboa: A platform for exploring parallel composition of templates," *arXiv preprint arXiv:1502.05347,* 2015.

[37] G. J. Zeglin, "Uniroo--a one legged dynamic hopping robot," Massachusetts Institute of Technology, 1991.

[38] A. D. Marchese, C. D. Onal, and D. Rus, "Autonomous soft robotic fish capable of escape maneuvers using fluidic elastomer actuators," *Soft Robotics,* vol. 1, pp. 75-87, 2014.

[39] J. Liu and H. Hu, "Biological inspiration: from carangiform fish to multi-joint robotic fish," *Journal of bionic engineering,* vol. 7, pp. 35-48, 2010.

[40] E. Chang-Siu, T. Libby, M. Tomizuka, and R. J. Full, "A Lizard-Inspired Active Tail Enables Rapid Maneuvers and Dynamic Stabilization in a Terrestrial Robot," in *International Conference on Intelligent Robots and Systems*, 2011, pp. 1887-1894.

[41] E. Chang-Siu, T. Libby, M. Brown, R. J. Full, and M. Tomizuka, "A Nonlinear Feedback Controller for Aerial Self-Righting by a Tailed Robot," in *International Conference on Robotics and Automation* 2013, pp. 32-39.

[42] K. Takita, T. Katayama, and S. Hirose, "The Efficacy of the Neck and Tail of Miniature Dinosaur-like Robot TITRUS-III," in *International Conference on Intelligent Robots and Systems*, 2002, pp. 2593-2598.

[43] J. Zhao, T. Zhao, N. Xi, F. J. Cintrón, M. W. Mutka, and L. Xiao, "Controlling aerial maneuvering of a miniature jumping robot using its tail," in *International Conference on Intelligent Robots and Systems* Tokyo, Japan, 2013, pp. 3802-3807.

[44] G. C. Haynes, J. Pusey, R. Knopf, A. M. Johnson, and D. E. Koditschek, "Laboratory on Legs: An Architecture for Adjustable Morphology with Legged Robots," in *SPIE Defense, Security, and Sensing*, 2012, pp. 83870W-83870W-14.

[45] J. Zhao, T. Zhao, N. Xi, M. W. Mutka, and L. Xiao, "MSU tailbot: Controlling aerial maneuver of a miniature-tailed jumping robot," *IEEE/ASME Transactions on Mechatronics,* vol. 20, pp. 2903-2914, 2015.

[46] A. Patel and M. Braae, "Rapid Acceleration and Braking: Inspirations from the Cheetah's Tail," in *IEEE International Conference on Robotics and Automation* 2014, pp. 793-799.

[47] K. C. Galloway, G. C. Haynes, B. D. Ilhan, A. M. Johnson, R. Knopf, G. A. Lynch*, et al.*, "X-RHex: A highly mobile hexapedal robot for sensorimotor tasks," 2010.

[48] N. Kohut, D. Haldane, D. Zarrouk, and R. Fearing, "Effect of Inertial Tail on Yaw Rate of 45 Gram Legged Robot," in *International Conference on Climbing and Walking Robots and the Support Technologies for Mobile Machinces*, 2012, pp. 157-164.

[49] N. J. Kohut, A. O. Pullin, D. W. Haldane, D. Zarrouk, and R. S. Fearing, "Precise Dynamic Turning of a 10 cm Legged Robot on a Low Friction Surface using a Tail," in *IEEE International Conference on Robotics and Automation* 2013, pp. 3299-3306.

[50] F. J. Berenguer and F. M. Monasterio-Huelin, "Zappa, a quasi-passive biped walking robot with a tail: Modeling, behavior, and kinematic estimation using accelerometers," *IEEE Transactions on Industrial Electronics,* vol. 55, pp. 3281-3289, 2008.

[51] W. S. Rone and P. Ben-Tzvi, "Continuum Robotic Tail Loading Analysis for Mobile Robot Stabilization and Maneuvering," in *International Design Engineering Technical Conferences and Computers and Information in Engineering Conference*, Buffalo, NY, USA, 2014, pp. V05AT08A009-V05AT08A009.

[52] J. Zhao, J. Xu, B. Gao, N. Xi, F. J. Cintrón, M. W. Mutka*, et al.*, "MSU jumper: A single-motor-actuated miniature steerable jumping robot," *IEEE Transactions on Robotics,* vol. 29, pp. 602-614, 2013.

[53] T. Libby, A. M. Johnson, E. Chang-Siu, R. J. Full, and D. E. Koditschek, "Comparative Design, Scaling, and Control of Appendages for Inertial Reorientation," *IEEE Transactions on Robotics,* vol. 32, pp. 1380-1398, 2016.

[54] A. M. Wilson, J. Lowe, K. Roskilly, P. E. Hudson, K. Golabek, and J. McNutt, "Locomotion dynamics of hunting in wild cheetahs," *Nature,* vol. 498, pp. 185-189, 2013.

[55] R. J. Full and D. E. Koditschek, "Templates and anchors: neuromechanical hypotheses of legged locomotion on land," *Journal of experimental biology,* vol. 202, pp. 3325-3332, 1999.

[56] C. Laschi and M. Cianchetti, "Soft robotics: new perspectives for robot bodyware and control," *Frontiers in bioengineering and biotechnology,* vol. 2, p. 3, 2014.

[57] S. Kim, C. Laschi, and B. Trimmer, "Soft robotics: a bioinspired evolution in robotics," *Trends in biotechnology,* vol. 31, pp. 287-294, 2013.

[58] W. S. Rone and P. Ben-Tzvi, "Mechanics modeling of multisegment rod-driven continuum robots," *ASME Journal of Mechanisms and Robotics,* vol. 6, p. 041006, 2014.

[59]   W. S. Rone and P. Ben-Tzvi, "Continuum robot dynamics utilizing the principle of virtual power," *IEEE Transactions on Robotics,* vol. 30, pp. 275-287, 2014.

[60]   N. G. Cheng, M. B. Lobovsky, S. J. Keating, A. M. Setapen, K. I. Gero, A. E. Hosoi*, et al.*, "Design and analysis of a robust, low-cost, highly articulated manipulator enabled by jamming of granular media," in *International Conference on Robotics and Automation* 2012, pp. 4328-4333.

[61]   K. Schmidt-Nielsen, "Locomotion: energy cost of swimming, flying, and running," *Science,* vol. 177, pp. 222-228, 1972.

[62]   R. Kram and T. J. Dawson, "Energetics and biomechanics of locomotion by red kangaroos (Macropus rufus)," *Comparative Biochemistry and Physiology Part B: Biochemistry and Molecular Biology,* vol. 120, pp. 41-49, 1998.

[63]   L. Hardesty. (2014, October, 6). *Soft robotic fish moves like the real thing*. Available: http://news.mit.edu/2014/soft-robotic-fish-moves-like-the-real-thing-0313

[64]   L. Birglen, T. Laliberté, and C. M. Gosselin, "Underactuated robotic hands." vol. 40, ed Springer-Verlag Berlin Heidelberg: Springer, 2007.

[65]   R. Balasubramanian and A. M. Dollar, "A Framework for Studying Underactuation in the Human Hand," in *Annual Meeting of the Americal Society of Biomechanics*, 2010, pp. 5-6.

[66]   G. Robinson and J. B. C. Davies, "Continuum robots-a state of the art," in *International Conference on Robotics and Automation*, 1999, pp. 2849-2854.

[67]   W. S. Rone and P. Ben-Tzvi, "Mechanics modeling of multisegment rod-driven continuum robots," *Journal of Mechanisms and Robotics,* vol. 6, p. 041006, 2014.

[68]   P. K. Singh and C. M. Krishna, "Continuum arm robotic manipulator: A review," *Universal Journal of Mechanical Engineering,* vol. 2, pp. 193-198, 2014.

[69]   Z. Li and R. Du, "Design and analysis of a bio-inspired wire-driven multi-section flexible robot," *International Journal of Advanced Robotic Systems,* vol. 10, p. 209, 2013.

[70]   Z. Li, R. Du, M. C. Lei, and S. M. Yuan, "Design and Analysis of a Biomimetic Wire-Driven Robot Arm," in *ASME International Mechanical Engineering Congress and Exposition*, 2011, pp. 191-198.

[71]   Z. Li, R. Du, H. Yu, and H. Ren, "Statics Modeling of an Underactuated Wire-Driven Flexible Robotic Arm," in *5th IEEE RAS/EMBS International Conference on Biomedical Robotics and Biomechatronics*, 2014, pp. 326-331.

[72] J.-w. Suh, K.-y. Kim, J.-w. Jeong, and J.-j. Lee, "Design considerations for a hyper-redundant pulleyless rolling joint with elastic fixtures," *IEEE/ASME Transactions on Mechatronics,* vol. 20, pp. 2841-2852, 2015.

[73] Y.-J. Kim, S. Cheng, S. Kim, and K. Iagnemma, "Design of a tubular snake-like manipulator with stiffening capability by layer jamming," in *International Conference on Intelligent Robots and Systems* 2012, pp. 4251-4256.

[74] E. Nazma and S. Mohd, "Tendon driven robotic hands: a review," *International Journal of Mechanical Engineering and Robotics Research,* vol. 1, pp. 1520-1532, 2012.

[75] L.-R. Lin and H.-P. Huang, "NTU hand: A new design of dexterous hands," *Journal of Mechanical Design,* vol. 120, pp. 282-292, 1998.

[76] T. Okada, "Object-handling system for manual industry," *IEEE Transactions on Systems, Man, and Cybernetics,* vol. 9, pp. 79-89, 1979.

[77] P. J. Kyberd, C. Light, P. H. Chappell, J. M. Nightingale, D. Whatley, and M. Evans, "The design of anthropomorphic prosthetic hands: A study of the Southampton Hand," *Robotica,* vol. 19, pp. 593-600, 2001.

[78] S. Hirose and Y. Umetani, "The development of soft gripper for the versatile robot hand," *Mechanism and Machine Theory,* vol. 13, pp. 351-359, 1978.

[79] M. G. Catalano, G. Grioli, E. Farnioli, A. Serio, C. Piazza, and A. Bicchi, "Adaptive synergies for the design and control of the Pisa/IIT SoftHand," *The International Journal of Robotics Research,* vol. 33, pp. 768-782, 2014.

[80] G. Palli, "Model and control of tendon actuated robots," Diss. alma, 2007.

[81] W. Rone, W. Saab, and P. Ben-Tzvi, "Design, Modeling, and Integration of the Universal-Spatial Robotic Tail," *Journal of Mechanisms and Robotics (Accepted),* 2018.

[82] E. Colgate and N. Hogan, "An Analysis of Contact Instability in Terms of Passive Physical Equivalents," in *International Conference on Robotics and Automation*, Scottsdale, Az, 1989, pp. 404-409.

[83] M. F. Silva and J. T. Machado, "A historical perspective of legged robots," *Journal of Vibration and Control,* vol. 13, pp. 1447-1486, 2007.

[84] S.-M. Song and K. J. Waldron, *Machines that walk: the adaptive suspension vehicle*: MIT press, 1989.

[85]   K. Arikawa and S. Hirose, "Mechanical design of walking machines," *Philosophical Transactions of the Royal Society of London A: Mathematical, Physical and Engineering Sciences,* vol. 365, pp. 171-183, 2007.

[86]   J. T. Machado and M. F. Silva, "An overview of legged robots," in *International Symposium on Mathematical Methods in Engineering*, Ankara, Turkey, 2006.

[87]   J. A. Galvez, J. Estremera, and P. G. De Santos, "A new legged-robot configuration for research in force distribution," *Mechatronics,* vol. 13, pp. 907-932, 2003.

[88]   X. Chen, L.-q. Wang, X.-f. Ye, G. Wang, and H.-l. Wang, "Prototype development and gait planning of biologically inspired multi-legged crablike robot," *Mechatronics,* vol. 23, pp. 429-444, 2013.

[89]   Y. Tang, S. Ma, Y. Sun, and D. Ge, "A multi-legged robot with less actuators by applying passive body segment joint," in *Intelligent Robots and Systems*, Vilamoura, Algarve, Portugal, 2012, pp. 1828-2833.

[90]   A. Schwab and M. Wisse, "Basin of attraction of the simplest walking model," in *International Design Engineering Technical Conferences and Computers and Information in Engineering Conference*, 2001, pp. 531-539.

[91]   A. Torige, M. Noguchi, and N. Ishizawa, "Centipede type multi-legged walking robot," in *Intelligent Robots and Systems*, Tokyo, Japan, 1993, pp. 567-571.

[92]   K. L. Hoffman and R. J. Wood, "Passive undulatory gaits enhance walking in a myriapod millirobot," in *International Conference on Intelligent Robots and Systems* San Francisco, CA, 2011, pp. 1479-1486.

[93]   U. Saranli, M. Buehler, and D. E. Koditschek, "RHex: A simple and highly mobile hexapod robot," *The International Journal of Robotics Research,* vol. 20, pp. 616-631, 2001.

[94]   B. Jimenez and A. Ikspeert, "Centipede robot locomotion," Master's thesis, Ecole Polytechnique Federale de Lausanne, 2007.

[95]   K. Yoneda, Y. OTA, F. Ito, and S. Hirose, "Construction of a quadruped with reduced degrees of freedom," in *Industrial Electronics Society*, Nagoya, Japan, 2000, pp. 28-33.

[96]   H. Funabashi, K. Ogawa, Y. Gotoh, and F. Kojima, "Synthesis of Leg-Mechanisms of Biped Walking Machines: Part I, Synthesis of Ankle Path Generator," *Bulletin of JSME,* vol. 28, pp. 537-543, 1985.

[97] M. Kaneko, M. Abe, K. Tanie, S. Tachi, and S. Nishizawa, "Basic Experiments on a hexapod walking machine (melwalk III) with an approximate straight-line link mechanism," in *International Conference on Advanced Robotics*, St. Louis, MO, 1985, pp. 397-410.

[98] C. Liang, M. Ceccarelli, and Y. Takeda, "Operation analysis of a one-DOF pantograph leg mechanisms," in *17th International Workshop on Robotics in Alpe-Adria-Danube Region*, Ancona, Italy, 2008, pp. 15-17.

[99] N. Lokhande and V. Emche, "Mechanical spider by using Klann mechanism," *International Journal of Mechanical Engineering and Computer Applications,* vol. 1, pp. 013-016, 2013.

[100] C. Tavolieri, E. Ottaviano, M. Ceccarelli, and A. Rienzo, "Analysis and design of a 1-DOF leg for walking machines," in *15th International Workshop on Robotics in Alpe-Adria-Danube Region*, Balatonfured, Hungary, 2006, pp. 15-17.

[101] H. Adachi, N. Koyachi, and E. Nakano, "Mechanism and control of a quadruped walking robot," *IEEE Control Systems Magazine,* vol. 8, pp. 14-19, 1988.

[102] E. C. Lovasz, C. Pop, F. Pop, and V. Dolga, "Novel solution for leg motion with 5-link belt mechanism," *International Journal of Applied Mechanics and Engineering,* vol. 19, pp. 699-708, 2014.

[103] S. Collins, A. Ruina, R. Tedrake, and M. Wisse, "Efficient bipedal robots based on passive-dynamic walkers," *Science,* vol. 307, pp. 1082-1085, 2005.

[104] M. Kaneko, M. Abe, S. Tachi, S. Nishizawa, K. Tanie, and K. Komoriya, "Legged locomotion machine based on the consideration of degrees of freedom," in *Theory and Practice of Robots and Manipulators*, ed: Springer, 1985, pp. 403-410.

[105] V. Krovi, G. Ananthasuresh, and V. Kumar, "Kinematic and kinetostatic synthesis of planar coupled serial chain mechanisms," *Journal of Mechanical Design,* vol. 124, pp. 301-312, 2002.

[106] K. Hashimoto, T. Hosobata, Y. Sugahara, Y. Mikuriya, H. Sunazuka, M. Kawase*, et al.*, "Development of foot system of biped walking robot capable of maintaining four-point contact," in *International Conference on Intelligent Robots and Systems*, Alberta, Canada, 2005, pp. 1361-1366.

[107]   M. Vukobratović and B. Borovac, "Zero-moment point—thirty five years of its life," *International Journal of Humanoid Robotics,* vol. 1, pp. 157-173, 2004.

[108]   M. W. Spong, S. Hutchinson, and M. Vidyasagar, *Robot modeling and control* vol. 3: Wiley New York, 2006.

[109]   E. J. Haug, *Computer aided kinematics and dynamics of mechanical systems* vol. 1: Allyn and Bacon Boston, 1989.

[110]   S. Kajita and B. Espiau, "Legged robots," in *Springer handbook of robotics*, ed: Springer, 2008, pp. 361-389.

[111]   C. Fernandes, L. Gurvits, and Z. Li, "Attitude control of space platform/manipulator system using internal motion," in *Space Robotics: Dynamics and Control*, ed: Springer, 1993, pp. 131-163.

[112]   E. Papadopoulos and S. Dubowsky, "On the nature of control algorithms for free-floating space manipulators," *IEEE Transactions on Robotics and Automation,* vol. 7, pp. 750-758, 1991.

[113]   K. Yoshida and Y. Umetani, "Control of space free-flying robot," in *Conference on Decision and Control*, Honolulu, HI, USA, 1990, pp. 97-102.

[114]   A. M. Johnson, T. Libby, E. Chang-Siu, M. Tomizuka, R. J. Full, and D. E. Koditschek, "Tail assisted dynamic self righting," in *International Conference on Climbing and Walking Robots and the Support Technologies for Mobile Machines*, Baltimore, MD, USA, 2012.

[115]   A. Demir, M. M. ANKARALI, J. Dyhr, K. Morgansen, T. Daniel, and N. Cowan, "Inertial redirection of thrust forces for flight stabilization," in *International Conference on Climbing and Walking Robots and Support Technologies for Mobile Machines*, Baltimore, MD, USA, 2012, pp. 239-245.

[116]   A. Patel and M. Braae, "Rapid turning at high-speed: Inspirations from the cheetah's tail," in *International Conference on Intelligent Robots and Systems*, Tokyo, Japan, 2013, pp. 5506-5511.

[117]   N. Kohut, D. Haldane, D. Zarrouk, and R. Fearing, "Effect of inertial tail on yaw rate of 45 gram legged robot," in *International Conference on Climbing and Walking Robots and the Support Technologies for Mobile Machines*, Baltimore, MD, USA, 2012, pp. 157-164.

[118] N. J. Kohut, A. O. Pullin, D. W. Haldane, D. Zarrouk, and R. S. Fearing, "Precise dynamic turning of a 10 cm legged robot on a low friction surface using a tail," in *IEEE International Conference on Robotics and Automation*, Karlsruhe, Germany, 2013, pp. 3299-3306.

[119] C. Casarez, I. Penskiy, and S. Bergbreiter, "Using an inertial tail for rapid turns on a miniature legged robot," in *International Conference on Robotics and Automation* Karlsruhe, Germany, 2013, pp. 5469-5474.

[120] F. Chernous' ko, "Modelling of Snake-Like Locomotions," *Modeling, Simulation and Optimization of Complex Processes,* pp. 105-114, 2005.

[121] F. Chernous' ko, "Controllable motions of a two-link mechanism along a horizontal plane," *Journal of Applied Mathematics and Mechanics,* vol. 65, pp. 565-577, 2001.

[122] T. R. Kane and M. P. Scher, "A dynamical explanation of the falling cat phenomenon," *International Journal of Solids and Structures,* vol. 5, pp. 663-670, 1969.

[123] T. R. Kane and M. P. Scher, "Human self-rotation by means of limb movements," *Journal of biomechanics,* vol. 3, pp. 39-49, 1970.

[124] E. C.-Y. Yang, P. C. P. Chao, and C.-K. Sung, "Optimal control of an under-actuated system for landing with desired postures," *IEEE Transactions on Control Systems Technology,* vol. 19, pp. 248-255, 2011.

[125] G. B. Gillis, L. A. Bonvini, and D. J. Irschick, "Losing stability: tail loss and jumping in the arboreal lizard Anolis carolinensis," *Journal of Experimental Biology,* vol. 212, pp. 604-609, 2009.

[126] A. Patel, E. Boje, C. Fisher, L. Louis, and E. Lane, "Quasi-steady state aerodynamics of the cheetah tail," *Biology Open,* 2016.

[127] R. M. Brown, D. H. Taylor, and D. H. Gist, "Effect of caudal autotomy on locomotor performance of wall lizards (Podarcis muralis)," *Journal of Herpetology,* pp. 98-105, 1995.

[128] W. Rone, W. Saab, A. Kumar, and P. Ben-Tzvi, "Controller Design, Analysis and Experimental Validation of a Robotic Serpentine Tail to Stabilize and Maneuver a Quadrupedal Robot," *Journal of Dynamic Systems Measurement and Control (submitted Nov. 2017).*

[129] M. S. Corporation, "Msc Adams " vol. 2015, ed, 2005.

[130] R. B. McGhee and A. A. Frank, "On the stability properties of quadruped creeping gaits," *Mathematical Biosciences,* vol. 3, pp. 331-351, 1968.